

**Nanoscale Manipulation of Surfaces and Interfaces: Engineering Electrical Properties  
Through Nanofabrication**

by

Copyright 2012  
Gregory J. Smith  
B.S., Texas A&M University – Corpus Christi, 2006

Submitted to the graduate degree program in Chemistry and the Graduate Faculty of the  
University of Kansas in partial fulfillment of  
the requirements for the degree of Doctor of Philosophy.

---

Chairperson Cindy L. Berrie

---

Carey K. Johnson

---

Robert C. Dunn

---

Timothy A. Jackson

---

Susan M. Stagg-Williams

Date Defended: November 7<sup>th</sup>, 2012

The Dissertation Committee for Gregory J. Smith  
certifies that this is the approved version of the following dissertation:

**Nanoscale Manipulation of Surface and Interfaces: Engineering Electrical Properties  
Through Nanofabrication**

---

Chairperson Cindy L. Berrie

---

Carey K. Johnson

---

Robert C. Dunn

---

Timothy A. Jackson

---

Susan M. Stagg-Williams

Date approved: January 10<sup>th</sup>, 2013

## Abstract

Nanotechnology interest and research has increased dramatically over the last decade, but there remain fundamental limitations and barriers to the fabrication of ever smaller devices. To overcome these limitations, new nanofabrication methods and novel nanoscale systems must be explored. To form nanoscale systems, we must have the ability to electrically interconnect various nanoscale parts. To do that, methods must be developed to form nanowires and nanofeatures in a very controlled fashion with arbitrary shapes. It should be noted, however, that materials' properties can change at nanoscale sizes, so these nanowires and nanofeatures themselves must be studied to ensure they function as designed. Materials with unique electronic properties and low dimensionalities, like graphene and carbon nanotubes also need to be studied for potential use in nanoscale devices. Graphene has been found to be electronically tunable by doping, causing it to be able to function as a semiconductor or as a metallic conductor. Understanding this doping interaction will help in the design and implementation of novel nanoscale systems and devices.

The first part of this work puts forth a method for fabricating metallic nanofeatures into self-assembled monolayer resists. An atomic force microscope (AFM) is used with methods called nanoetching and grafting and oxidative lithography to form patterned nanofeatures down to 20 nm in width. Nanoetching and grafting involve using the AFM tip to directly remove molecules and replace them with new ones, creating a nanopattern. Oxidative lithography uses a conductive AFM tip as a tiny electrode to write nanopatterns into surfaces by very localized electrochemical oxidation. These nanopatterns are then exposed to an electroless copper plating solution, which selectively plates copper right onto those nanopatterns, to form copper nanofeatures. These are characterized with the AFM that helped form them. With this AFM

based method, features of any shape can potentially be formed, providing a way to wire up more complex nanodevices and circuitry.

The second part investigates the interaction between graphene-like materials and adsorbates. These interactions are becoming increasingly important as these materials become incorporated into more devices. There has been much study recently focused on graphene and graphene-like materials, such as carbon nanotubes and graphite. Graphene is of particular interest because of its low dimensionality, being a two-dimensional sheet of  $sp^2$  hybridized carbon atoms, and its unique properties. It is tough and flexible, but what is most interesting is that its electronic properties are very tunable. Adsorbates can dope it p-type or n-type, so it behaves more like a semiconductor or a metal, respectively. In this work, azulene derivatives and gold nanoparticles are studied as potential adsorbates on graphene-like materials. Azulene molecules themselves have very tunable HOMO and LUMO levels, and it could be possible to dope graphite-like materials in different fashions with different types of azulenes. Gold nanoparticles can also be tunable with size and shape, and their ability to dope graphene-like materials is of interest. Using an AFM technique called surface potential mapping, the electrostatic potential of azulenes adsorbed onto graphite was studied. It was found that azulene and azulene compounds with electron withdrawing groups at the 1 and 3 positions were more negative in the potential than the graphite, indicating they were pulling electrons out of the material. An azulene compound with electron donating groups at the 1 and 3 positions was positive in potential with respect to the graphite surface, indicating donation of electrons to the graphite. This is good evidence that azulenes can be tunable dopants for modifying the properties of graphene-like materials.

Using AFM based techniques, this work advances methods to form and electrically characterize nanoscale metallic features and decorated graphene-like materials that could have important applications as nanotechnology moves forward into complex nanodevice fabrication. It also gives insight into a novel system, azulenes on a graphene-like material, at a nanoscale level of resolution. Study of nanosystems like these is integral to the advancement of nanotechnology as a whole.

## Acknowledgments

I must first acknowledge my advisor, Dr. Cindy Berrie. Her knowledge, expertise, and motivation has really inspired me over the years, as has her dedication to her students and teaching. I really think Cindy's advisor style is well suited to me, and believe I wouldn't've done any better under anyone else. I thank Cindy for the years of advice, teaching and support she has given me, and hope I can be to my future students what she has been to me.

I also acknowledge the rest of the Berrie group I've worked with over the years. Dave, who really helped me get started in the lab, Jen and Tina, for good times working together, and Rodi for being Rodi. I want to also thank Matt for his friendship and time spent doing homework problems and playing games.

The rest of the Pchem faculty here at KU need mention as well. I think I've been a TA at least once for 5 or 6 of them. I am thankful to them for their great teaching and for helping me make my own teaching what it is today.

Finally, I would like to voice my appreciation for my partner, Melisa. She somehow has the patience to put up with me, and I don't really think I'd be where I am today without her. Words cannot truly express how grateful I am to her for her love, support, and sacrifice.

## Table of Contents

Abstract .....	iii
Acknowledgments.....	vi
List of Figures .....	xi
List of Tables .....	xvii
<b>Chapter 1: Introduction and Background</b>	
1.1 Background.....	1
1.2 Nanofabrication of Metallic Nanofeatures.....	5
1.2.1 Potential Nanodevice Utilizing ATP Synthase .....	6
1.2.2 Nanolithography Methods .....	7
1.3 Adsorbates on Graphene-Like Materials .....	11
1.4 Overview.....	13
<b>Chapter 2: General Methods and Instrumentation</b>	
2.1 Overview.....	20
2.1 Self-Assembled Monolayers.....	20
2.2 Goniometry .....	22
2.3 Ellipsometry .....	23
2.4 Atomic Force Microscopy .....	24
2.4.1 General Description .....	24
2.4.2 Contact Mode.....	25
2.4.3 Tapping Mode.....	26

2.5 Implementation .....	27
--------------------------	----

### **Chapter 3: Nanofabrication of Nanopatterns and Copper Nanofeatures**

3.1 Introduction.....	30
-----------------------	----

3.2 Materials and Methods.....	36
--------------------------------	----

3.2.1 Self-Assembled Monolayer Formation and Characterization.....	36
--	----

3.2.2 Nano-Etching and Grafting.....	38
--------------------------------------	----

3.2.3 Oxidative Lithography .....	40
-----------------------------------	----

3.2.4 Electroless Copper Plating.....	41
---------------------------------------	----

3.3 Results and Discussion .....	42
----------------------------------	----

3.3.1 Electroless Copper Plating Selectivity.....	42
---	----

3.3.2 Nano-Etching and Grafting Results .....	43
---	----

3.3.3 Oxidative Lithography Results .....	45
---	----

3.3.3.1 Oxidative Lithography on ODT .....	45
--	----

3.3.3.2 Oxidative Lithography on OTS .....	48
--	----

3.3.4 Electroless Copper Plating Results .....	51
--	----

3.3.4.1 Electroless Copper Plating on ODT.....	51
--	----

3.3.4.2 Electroless Copper Plating on OTS .....	54
---	----

3.5 Conclusion .....	60
----------------------	----

### **Chapter 4: Surface Potential Mapping of Azulene Derivative and Gold Nanoparticles**

#### **Adsorbed onto Graphite**

4.1 Introduction.....	66
-----------------------	----



4.1.1 Graphene-Like Materials Properties .....	67
4.1.2 Graphene-Like Materials in Devices .....	68
4.1.3 Tunability of Graphene-Like Materials' Electronic Properties .....	70
4.1.4 Azulene Compounds and Gold Nanoparticles as Adsorbates.....	71
4.2 Methods and Materials.....	75
4.2.1 Azulene Compounds, Naphthalene, and Toluene.....	76
4.2.2 Gold Nanoparticles .....	76
4.2.3 Highly Ordered Pyrolytic Graphite.....	78
4.2.4 Azulenes and Naphthalene Adsorption onto Graphite.....	78
4.2.5 Gold Nanoparticle Adsorption onto Graphite.....	79
4.2.6 Surface Potential Mapping.....	79
4.3 Results and Discussion .....	81
4.3.1 Azulenes on Graphite.....	81
4.3.1.1 Clean Graphite .....	81
4.3.1.2 Solvent Controls.....	82
4.3.1.3 Napthalene .....	85
4.3.1.4 Azulene .....	86
4.3.1.5 1,3-di(2,2,2-trifluoro-1-oxoethyl)azulene.....	88
4.3.1.6 1-(2,2,2-trifluoro-1-oxoethyl)azulene.....	88
4.3.1.7 1,3-diiodoazulene.....	90
4.3.1.8 Azulenes on Graphite Summary .....	92

4.3.2 Gold Nanoparticles on Graphite .....	93
4.3.2.1 Gold Nanospheres.....	93
4.3.2.2 Gold Octahedral Nanoparticles.....	94
4.3.2.3 Gold Nanostars.....	95
4.3.2.4 Gold Nanoparticles Summary.....	95
4.4 Conclusion .....	96
 <b>Chapter 5: Conclusions and Future Directions</b>	
5.1 Overview.....	102
5.2 Nanofabrication of Copper Nanofeatures .....	103
5.2.1 Conclusion .....	103
5.2.2 Future Direction.....	104
5.2.2.1 Oxidative Lithography and Electroless Copper Plating Optimization .....	105
5.2.2.2 Copper Nanofeature Electronic Properties Characterization.....	106
5.3 Adsorbates on Graphite Conclusion .....	107
5.3.1 Conclusion .....	107
5.3.2 Future Direction.....	109
5.3.2.1 Azulene Compounds.....	109
5.3.2.2 Adsorbates on Graphene and CNT .....	110
5.4 Final Statement .....	110

## List of Figures

- Figure 1.1 Log scale plot of transistor count vs. date of introduction for commercially available microprocessors. The line indicates the Moore's Law prediction, a doubling of transistors per microprocessor every two years. ....3
- Figure 1.2 Diagram of a potential nanodevice using the  $F_1$  portion of the ATP synthase protein as a molecular rotor. The ability to form the metallic nanofeatures in any size and shape would facilitate fabrication of nanodevices like this one. 7
- Figure 1.3 Pattern of mercaptohexadecanoic acid in a mixed monolayer of hexanethiol and octadecanethiol. A) Topography image and B) lateral force image. This shows the ability to form arbitrarily shaped patterns with the nanoetching and grafting method. Reprinted from Appl. Surf. Sci., 175-176, S. Cruchon-Dupeyrat, et al., Nanofabrication using computer-assisted design and automated vector-scanning probe lithography, 636-642, Copyright (2001), with permission from Elsevier.....10
- Figure 2.1 SAM-substrate systems used. Thiols on gold (top) and silanes on the native oxide of silicon (bottom).....21
- Figure 2.2 Representation of a contact angle ( $\theta$ ) measurement of a droplet of water on a hydrophobic surface (top) and a hydrophilic surface (bottom) .....22
- Figure 2.3 Diagram of an ellipsometer. The elliptically polarized light changes polarization upon reflection at the sample surface. This change contains information about the optical properties of the sample at that surface .....23
- Figure 2.4 Topography (left) and friction trace (middle) and retrace (right) images of an oxidized nanopattern in an OTS SAM. The topography shows the physical features of the surface where the pattern is a slightly raised feature. The friction indicates that the chemistry is different inside and outside the nanopattern.....26
- Figure 2.5 Topography (left) and surface potential (right) images of a flake of graphite on at OTS SAM. The topography shows the graphite flake as a plateau on the OTS surface, while the potential image maps out the electrostatic potential. ....27
- Figure 3.1 Depiction of the nano-etching and grafting method. The resist SAM (top-left) is etched into with the AFM tip. New molecules, indicated with a Y, fill into the open area on the substrate .....39

Figure 3.2 Silane molecules in a SAM. Each molecule can bond with the substrate and up to two neighbors.....	40
Figure 3.3 Depiction of copper electroless plating. Copper selectively gets reduced on the patterned in oxidized chemistry over the methyl terminated resist .....	41
Figure 3.4 Scheme of the overall method of the presented work. Starting with SAMs of ODT on gold and OTS on silicon oxide, they are investigated in both nano-etching and grafting and oxidative lithography to pattern in an oxidized template. This pattern is then exposed to an electroless copper plating solution to selectively form copper nanofeatures on the oxidized template .....	42
Figure 3.5 Topography images of an ODT and a MUA SAM before and after 10 minutes of exposure to the 4 mM Cu <sup>2+</sup> electroless plating solution. A) ODT SAM before exposure. B) ODT SAM after exposure. There is almost no change in the topography, indicating very little copper deposition. C) A section through the surface in B. D) MUA SAM before exposure. E) MUA SAM after exposure. The topography is much rougher, indicating copper deposition across the surface. F) A section across the surface in E.....	43
Figure 3.6 Topography (left) and friction (right) images of ODT on gold taken simultaneously in contact mode AFM after etching ODT molecules out and grafting MUA molecules in. The roughness of the topography image masks the change in height, though the friction contrast is very visible. Three nanopatterns of MUA have been grafted into the ODT later, the narrowest of which is 30 nm at its widest point .....	44
Figure 3.7 Topography image (left) and profile (right) of 3 neat etches into OTS on silicon oxide. The vertical distance between the two markers is 5.5 Å, much shorter than the thickness of the OTS SAM, 27.7 Å .....	44
Figure 3.8 Topography (left) and friction (right) images of ODT on gold taken simultaneously in contact mode AFM after selectively oxidizing nanofeatures into the surface. Features that appear in both images have some substrate oxidation, while those that appear only in friction have little to none. a-f: -6.00 V tip bias, varying tip velocities and number of scans. g-j: -6.50 V tip bias, varying tip velocities and number of scans .....	46
Figure 3.9 Topography (left) and friction (right) images of pattern c, formed with -6.00 V tip bias, 5.31 μm/s tip velocity for about 160 passes. There is very little indication of a feature in the topography image, indicating oxidation of just the monolayer .....	47

Figure 3.10 Topography (left) and friction (right) images of oxidized nanopatterns in an OTS monolayer on silicon oxide. Each of the 20 patterns was formed under different conditions, with varying tip biases, tip velocities, and number of scans. The most pertinent patterns are labeled. a: formed with a -4.50 V tip bias, 5.31  $\mu\text{m/s}$  tip velocity, and about 1600 passes. b: formed with a -6.00 V tip bias, 5.31  $\mu\text{m/s}$  tip velocity, and about 800 passes. c: formed with a -5.50 V tip bias, 5.31  $\mu\text{m/s}$  tip velocity, and about 800 passes. d: formed with a -5.57 V tip bias, 0.20  $\mu\text{m/s}$  tip velocity, and about 20 passes .....49

Figure 3.11 Topography (left) and friction (right) images of oxidized nanofeatures in OTS on silicon oxide, patterns c and d. C) pattern c showing faint contrast in topography and friction. The OTS monolayer is slightly oxidized. D) pattern d is a very thin line ( $< 20 \text{ nm}$ ) of oxidation, showing a slight depression in topography, but a clear feature in friction.....50

Figure 3.12. Topography images of oxidized nanofeatures before (left) and after (right) exposure to a 4 mM  $\text{Cu}^{2+}$  electroless plating solution. Each feature is labeled for reference since they do not all appear in the image before plating.....52

Figure 3.13 Topography (left) and height profiles (right) of copper nanofeatures. Section A profiles a copper nanofeatures formed on oxidized pattern c, while section B profiles a feature formed on oxidized pattern b .....53

Figure 3.14 Topography of a copper nanofeature formed on oxidized pattern c, rendered in 3D to better reveal its overall topography. The grains that make up the feature are roughly on the order of  $100 \text{ nm}^2$  .....54

Figure 3.15 Topography images of oxidized nanopatterns before (left) and after (right) exposure to a 4 mM  $\text{Cu}^{2+}$  electroless copper plating solution for 20 minutes. Although there is some non-specific random growth, most of the patterns show an increase in topography from before plating to after. The labeled patterns correspond to the types of oxidized patterns formed. a: no oxidation occurred. b: overoxidation. c: slight oxidation. d: oxidation partially into the monolayer.....55

Figure 3.16. Topography images of copper deposition on oxidized patterns c (right) and d (left) in OTS on silicon oxide after 20 minutes of exposure to the 4 mM  $\text{Cu}^{2+}$  electroless plating solution. Each feature shows some nanoparticles of copper that have selectively formed on the oxidized regions .....56

Figure 3.17. Topography of oxidized features after a total of 30 minutes exposure time to the 4 mM  $\text{Cu}^{2+}$  electroless plating solution. Many features appear slightly more pronounced than after 20 minutes exposure time .....56

Figure 3.18. Topography (left) and height profiles (right) of copper deposition. Section C profiles copper deposition formed on oxidized pattern c, while section D profiles a deposition formed on oxidized pattern d .....	58
Figure 3.19 Topography and sections of oxidized pattern c in OTS monolayer through increasing amounts of exposure to the 4 mM Cu <sup>2+</sup> electroless plating solution. The sections lie between the markers for each image A) no plating time, the oxidized feature is almost imperceptible. B) 20 minutes plating time. Copper nanoparticles have selectively formed on the nanopattern. C) 30 minutes plating time. More copper has deposited, but it does not fill out the pattern. D) 40 minutes plating time. The feature has not grown, though it has changed slightly.....	59
Figure 4.1 Simple drawing of the molecular structure of graphene .....	67
Figure 4.2 Primitive cell (left), Brillouin zone (middle), and $\pi$ and $\pi^*$ energy levels in momentum space around the K point (right). The $\pi$ orbital (blue) acts as a valence band, and the $\pi^*$ orbital (red) the conductance band. In pristine graphene there is a zero energy gap between these bands. Upon doping, the graphene can behave like a metallic conductor (n-doping) or a semiconductor with an engineered band gap (p-doping). .....	70
Figure 4.3 The azulene molecule with carbon numbering scheme.....	72
Figure 4.4 Solutions of varying sizes of gold nanoparticles .....	74
Figure 4.5 Molecular adsorbates investigated .....	76
Figure 4.6 UV-Vis spectra showing the plasmon absorption bands of the gold nanoparticles synthesized and used as adsorbates. ....	77
Figure 4.7 Diagram of the surface potential mapping AFM experiment. For every scan, a topography scan (left) is performed first in tapping mode. The tip is then pulled off the surface to the desired lift height. The conductive tip then scans over the topography trace just recorded, while an AC bias is supplied to the tip. This bias causes the tip to feel a force from the electrostatic potential of the surface and begin to oscillate. A DC bias is then also applied to the tip to bring this force to a minimum. This DC bias verses position is recorded as the surface potential map.....	80
Figure 4.8 Topography (left) and surface potential (right) images of a freshly cleaved graphite surface. The topography has the characteristic sheets and step edges of graphite. In the surface potential image, the negative potential contrast at the step edges can be seen (A), as well as the local variability in the potential in different sheet (B). .....	81

- Figure 4.9 Topography (left) and surface potential (right) images of a graphite surface with toluene molecules adsorbed. The toluene nanofeatures are lined up with the hexagonal lattice of the underlying graphite. The surface potential shows that each toluene feature exhibits a positive potential contrast against the graphite sheets. The circle indicates one of these features across both images. ....82
- Figure 4.10 Topography (left) and surface potential (right) images of a graphite surface that has been exposed to methylene chloride for over 10 seconds. The graphite sheets show signs of etching; these etches appear to be aligned with the graphite lattice. The surface potential shows that these etches to have a positive potential contrast with the rest of the graphite. The circle indicates one of the etches across both images. ....83
- Figure 4.11 Topography (left) and surface potential (right) images of a graphite surface immediately after exposure to benzene. Even though the benzene was neat, it doesn't cover the entire surface. (A) indicates a region with no benzene adsorption, while (B) indicates a region with benzene adsorption. In the surface potential image, benzene has a positive potential contrast against graphite surface ...84
- Figure 4.12 Topography images of graphite surfaces after exposure to benzene (left) and methylene chloride (right). The left surface was dried under nitrogen for two minutes to remove any residual benzene. The right surface was exposed to methylene chloride for less than ten seconds. Although solvent can affect the surface, with proper treatment these effects can be avoided .....85
- Figure 4.13 Topography (left) and surface potential (right) images of a graphite surface with naphthalene molecules adsorbed. The naphthalene provides almost full coverage of the surface. The surface potential shows the naphthalene with discernible potential against the graphite. The negative potential contrast of the step edges is clearly visible through the adsorbed naphthalene.....86
- Figure 4.14 Topography (left) and surface potential (right) images of a graphite surface with azulene molecules adsorbed. The azulene adsorbs in small, flat, irregular features. The nanofeatures of azulene exhibit a negative potential contrast against the surrounding graphite surface. (B) is a zoomed in image in (A), indicated by the square. ....87
- Figure 4.15 Topography (left) and surface potential (right) images of a graphite surface with DTFA molecules adsorbed. The DTFA adsorbs in small triangles and strips, as seen in the topography image, especially near the center. There are also many areas of open graphite. In the surface potential image, these nanofeatures of DTFA exhibit a negative potential against the bare graphite surface. The circle

indicates crystals of DTFA and their potential (B) is a zoomed in image in (A), indicated by the square.....	89
Figure 4.16 Topography (left) and surface potential (right) images of a graphite surface with TFA molecules adsorbed. Like azulene, the TFA seems to adsorb in mostly small, flat, irregular nanofeatures. There is also accumulation of contaminant at step edges. In the surface potential image, the TFA features show a negative potential contrast against the graphite surface. (B) is a zoomed in image in (A), indicated by the square.....	90
Figure 4.17 Topography (left) and surface potential (right) images of a graphite surface with DIA molecules adsorbed. The DIA adsorbs much less orderly than the previous azulenes and are mostly near step edges with a few clumps on open sheets. The adsorbed DIA molecules stand out as a positive potential against the surrounding graphite surface.....	91
Figure 4.18 Rough approximation of the energy levels of graphite, azulene, DIA and DTFA. Azulene's LUMO lies close in energy to the Fermi level of graphite. Destabilization of the HOMO by electron donating groups like DIA brings it closer to the Fermi level. Stabilization of the HOMO by electron withdrawing groups like DTFA moves it farther away. ....	92
Figure 4.19 Topography (left) and surface potential (right) images of a graphite surface with 40 nm diameter spherical gold nanoparticles adsorbed. The nanoparticles are in groups and singles, and cluster about the step edges. The surface potential image shows that the particles exhibit a positive potential against the graphite surface.....	93
Figure 4.20 Topography and section (left) and surface potential (right) images of a possibly octahedral gold nanoparticle adsorbed onto a graphite surface. The particle is roughly 300 nm in diameter, and in the section through the particle, some edges can be seen. Like the nanospheres, this particle exhibits a positive contrast in the potential against the graphite surface .....	94
Figure 4.21 Topography (left) and surface potential (right) images of a small cluster (2 or 3 based on size) of gold nanostars on a graphite surface. As with the other nanoparticles studied, these exhibit a positive potential against the graphite surface.....	95



## **List of Tables**

Table 2.1 Ellipsometric Characterization of Thiol SAMs on Gold Substrate .....	24
Table 3.1 SAM Characterization .....	38
Table 3.2 Summary of Patterned Nanofeatures Presented.....	48
Table 3.3 Summary of Oxidative Lithography and Copper Plating on OTS.....	60

## Chapter 1: Introduction and Background

### 1.1 Background

Interest in materials' structure and properties at the nanoscale has risen rapidly in the last decade. Factors driving this interest include electronics and robotic miniaturization, the role of nanostructure on interface properties, chemistry at the interfaces of nanostructured materials, and the electrical properties of nanostructured graphene-like materials. For electronics, there is a constant push for smaller and more powerful devices.<sup>1</sup> This has implications not only commercially, but scientifically as well, as more powerful computing enables more complex computational studies to be performed. Nano-robotics is gaining attention in medical research; it is envisioned that biomolecular nanorobots will be able to shuttle drugs to specific areas within a cell.<sup>2</sup> Properties of interfaces depend on the nanostructure of surfaces. Superhydrophobic surfaces are nano-roughened to trap tiny pockets of air at the interface; these have applications in industry as self-cleaning and antioxidant surfaces as well as in microfluidics to decrease drag.<sup>3</sup> In addition, surface nanostructure affects friction and wear, important in industry but also in medical implants.<sup>4</sup> The chemical properties of substances can change as a result of nanostructure as well. Nano-porous gold, for instance, shows a different reactivity than bulk gold.<sup>5</sup> Graphene, a planar and conductive hexagonal network of  $sp^2$  bonded carbon atoms, and its derivatives, carbon nanotubes and graphite, are presently playing an important role in nanotechnology research. Graphene-like materials' special electronic and physical properties, discussed below, make it an interesting subject for this area, particularly in electronic nanodevices.<sup>6</sup> From these examples, we see that properties of materials change when dimensions get down to the nanoscale. One reason for this change is as an object gets smaller and smaller, quantum confinement effects begin to affect electronic properties. Gold nanoparticles, for instance, show

changes in reactivity and catalytic activity at diameters in the single digit nanometer range.<sup>7</sup> Another reason for this change is surface area to volume ratio. When a particle's diameter is reduced to nanometer length scales, surface area to volume ratio is very high, and the bulk properties diminish or are absent. Surface effects now dominate the properties and this is very evident in metallic nanoparticles. Here, surface plasmonic effects control how the particles interact with light, causing scattering and absorption of varying wavelengths depending on the exact size and shape of the nanoparticle.<sup>8</sup>

More specific areas that benefit from advances in nanotechnology include lab-on-a-chip<sup>9</sup> (LOC) devices, sensing, nanoelectronics, and energy. LOC devices are designed as complete analytic tools on small chips and typically utilize microfluidics. A better understanding of how to implement nanostructure into these devices will help improve their sensitivity, longevity, and broaden their application. Related to LOC devices, the role of nanotechnology in sensing has become increasingly important. Due to their large surface area to volume ratios, nanoscale materials can be very sensitive to their immediate environment. Electrochemical sensors with nanostructured electrodes show enhanced signal to noise ratios since many of their properties depend on surface area.<sup>10</sup> Nano-surface plasmon resonance techniques have been described that show nanomolar limits of detection using gold nanorods.<sup>11</sup> These techniques use UV-Vis spectroscopy to track the changes in the surface plasmon resonance of the gold nanorods as they bind analyte in solution.

For electronics, an important prediction and observation made in the 1960's by Intel co-founder Gordon Moore, known as Moore's Law, is that the number of transistors on an integrated circuit doubles roughly every two years.<sup>12</sup> This trend has been followed since then, shown in Figure 1.1, but we are rapidly approaching a fundamental limit.<sup>13</sup> Currently, the

smallest transistors, with component sizes on the order of tens of nanometers, are made with excimer laser and extreme ultraviolet lithography methods.<sup>14</sup> These transistors are made of doped silicon, and even as progress is made reducing size, they are still facing a power problem.<sup>13</sup> As the transistors get smaller, ideally they would require less voltage, maintaining the same power density. This is not the case, however, and the power density must be increased

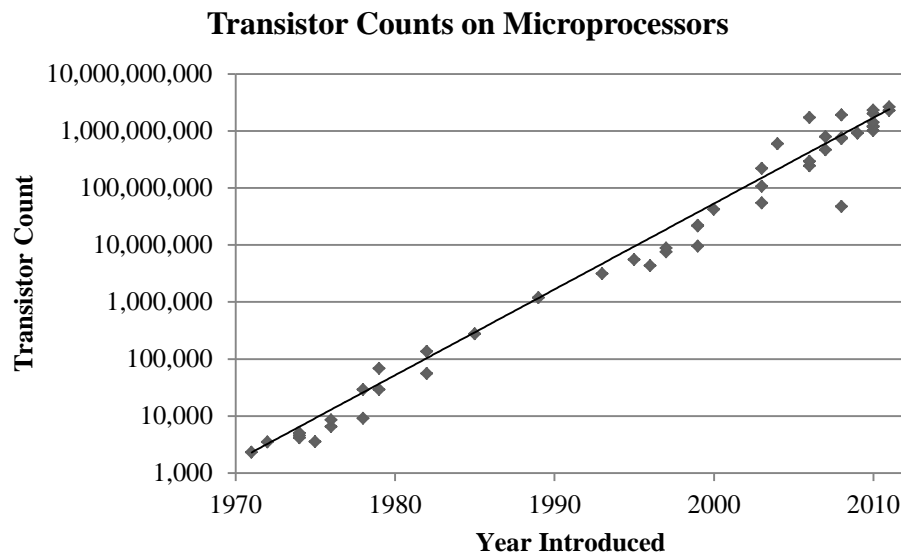


Figure 1.1 Log scale plot of transistor count vs. date of introduction for commercially available microprocessors. The line indicates the Moore's Law prediction, a doubling of transistors per microprocessor every two years. Source: [http://en.wikipedia.org/wiki/Transistor\\_count](http://en.wikipedia.org/wiki/Transistor_count) and references, accessed: 10/30/2012.

to keep the transistors from generating errors. Moving to a transistor material that can still work at the nanoscale and with higher electron mobility may help push these limits even further. Graphene-like materials, such as graphene nanoribbons and carbon nanotubes (CNT), are potential materials that could be used instead of doped silicon.<sup>15</sup>

In the area of energy, more efficient energy harvesting and storing devices are needed to keep up with ever increasing demand. Nanostructure of devices is of importance in solar cells, fuel cells, and batteries. Solar cells involve conversion of light to electronic energy and excited

electrons must travel to the electrode. In dye-sensitized solar cells (DSSC), dyes molecules are adsorbed or chemisorbed onto a nanostructured semiconductor substrate, typically titania, and immersed in an electrolyte solution. The morphology of the nanostructure can have an effect on the path of the electron to the electrode, scattering of light in the cell, and diffusion of the electrolyte. These all, in turn, have an effect on the cell's efficiency. Study of the effects of this morphology is a very active area of research, with studies detailing titania nanorods and nanoflowers,<sup>16</sup> and nanoneedle titania coated carbon nanofibers<sup>17</sup> and many more.<sup>18, 19</sup> For fuel cells, nanostructured catalysts increase the available surface area, increasing rate. For example, researchers have studied palladium and palladium-yttrium nanoparticles decorating carbon nanosheets as catalysts.<sup>20</sup> Lithium-ion batteries are dependent on nanostructure as well, as the ions must travel in and out of the electrodes when charging and discharging. This can cause the electrode material to become pulverized from the volume expansion and reduction during charging and recharging, reducing the performance of the battery. Research is being performed studying new electrode materials, such as tin alloys, formed with nanostructure built in to help stabilize the electrode and increase battery life.<sup>21</sup>

One material in particular that has garnered a lot of attention is graphene and graphene-like materials. As mentioned previously, graphene is a flexible single sheet of  $sp^2$  hybridized carbon atoms arranged in a hexagonal lattice. The bonds between these carbon atoms are fully conjugated, giving graphene very interesting electronic properties. The electronic structure of ideal graphene is such that it acts as a zero-band gap semiconductor.<sup>22</sup> What this means practically is that graphene is very tunable; placing it on a substrate or adsorbing molecules can shift the Fermi level above or below the zero-band gap point, causing the material to conductively behave as a metal or a semiconductor. It can also be cut into nanoribbons, giving it

a range of potential shapes. This gives graphene a wide range of applications within nanoelectronics, from field-effect transistors (FETs)<sup>23</sup> to flexible electrodes.<sup>24</sup> Carbon nanotubes (CNTs), a graphene-like material that can be thought of as a rolled up sheet of graphene, can also behave as conductors or semiconductors based on how they are rolled up.<sup>22</sup> They too have seen much interest as materials in nanoelectronics; researchers at IBM have recently reported fabrication of transistor arrays using CNTs.<sup>25</sup> Graphite is composed of many stacked sheets of graphene, and is an excellent starting point for research into graphene-like materials, due to its relative low cost and ease of use. These materials are described in more detail in Chapter 4.

## **1.2 Nanofabrication of Metallic Nanofeatures**

In the previous section, the importance and relevance of nanoscale and nanostructured materials was discussed. In order to study and exploit these various properties, many nanomaterials have been designed and formed; this is nanofabrication. One of the areas that needs more development is the nanofabrication of metallic nanofeatures for use in electronic nanodevices, especially for prototyping. These features could be used as electrical interconnects to wire together different components in the nanodevice, or serve as components themselves. The requirements on the dimensions of the metallic nanofeatures for use in novel nanodevices would, of course, vary greatly from device to device. A simple method to form these kinds of features in any shape, form, and location on the surface would be the ideal. This would give researchers investigating nanodevices a powerful tool for design and implementation. To give an example of the flexibility and dimensions that might be required by such a prototype nanodevice, in this section a potential complex nanodevice is described. This nanodevice would utilize a molecular rotor, ATP synthase, as a component and metallic features fabricated near it to characterize and perhaps even drive its rotation. Also described in this section are many methods

of nanofabrication that can allow for very directed and controlled growth and positioning of the nanomaterial being formed. These methods include photolithography, e-beam lithography, nano-imprint lithography, dip-pen lithography, nano-etching and grafting, and oxidative lithography. These methods are described briefly here, and in greater detail in Chapter 3.

### 1.2.1 Potential Nanodevice Utilizing ATP Synthase

ATP synthase is a membrane bound protein that is found in many organisms, and its function is to synthesize adenosine triphosphate (ATP), the energy currency of the cell, from adenosine diphosphate (ADP).<sup>26</sup> This protein has two portions called the  $F_0$  and the  $F_1$  portions. The  $F_0$  portion is the membrane bound portion, while the  $F_1$  portion lies outside the membrane. The  $F_1$  portion is composed of 3  $\alpha$  subunits, 3  $\beta$  subunits, arranged in a barrel shape, and a  $\gamma$  subunit that lies in this barrel and protrudes out one end. The  $F_1$  portion contains the active site for ATP synthase. When synthesizing ATP, the  $\gamma$  subunit rotates inside the barrel, causing conformational changes at the active site to drive the reaction. When free from the rest of the protein, the  $F_1$  portion will hydrolyze ATP, causing the  $\gamma$  subunit to rotate in the opposite direction. The dimensions of the  $F_1$  portion, about 10 nm in diameter, make it a good choice for incorporation into a nanodevice.

In a potential nanodevice utilizing the  $F_1$  portion, the protein would sit on the surface with the  $\gamma$  subunit protruding up. Attached to the  $\gamma$  subunit would be an armature, parallel with the surface, with a magnetic nanoparticle attached. This would allow rotation of the armature and particle around the protein as it hydrolyzes ATP. In order to monitor this rotation, metallic nanowires would be fabricated around the protein, so that as the magnetic nanoparticle travels above them, a small but measurable current is induced in the nanowires. A diagram of this

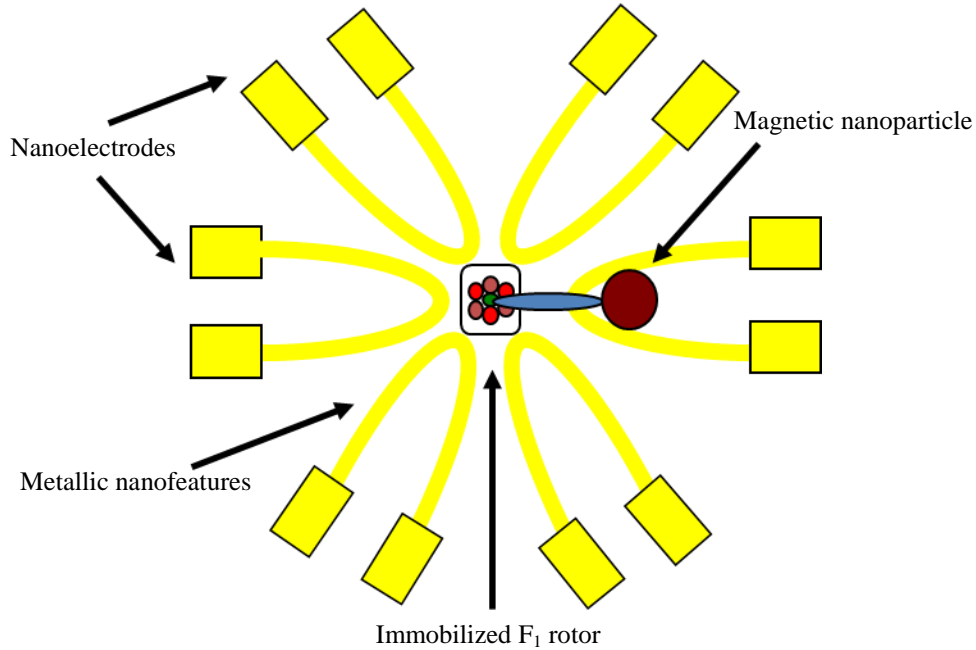


Figure 1.2 Diagram of a potential nanodevice using the  $F_1$  portion of the ATP synthase protein as a molecular rotor. The ability to form the metallic nanofeatures in any size and shape would facilitate fabrication of nanodevices like this one.

nanodevice is shown in Figure 1.2. The dimension of the nanowires themselves would have to be such that they could be close enough to the protein and have a low enough profile for the magnetic nanoparticle to move over them. Given the dimensions of the  $F_1$  portion, the nanowires would need to be 10 nm high and in the low 10s of nm in width. It is this kind of flexibility in forming metallic nanofeatures that we are aiming for in method development. The ability to form metallic nanofeatures of arbitrary size and shape would be a great enabler for various nanodevice systems, such as the one described.

### 1.2.2 Nanolithography Methods

As mentioned previously, there are many methods that exist today for forming these metallic nanofeatures. Here they are briefly summarized and evaluated. Photolithography has long been a method for creating mass produced micro and nano sized circuitry on



semiconductors. Recent advancements with excimer laser and extreme ultraviolet lithography have pushed the sizes of transistor features down to tens of nanometers.<sup>14</sup> Using an interference method, recent work has been reported showing arrays of features with widths of 35 nm.<sup>27</sup> While these methods may offer good size, controllability, and production, to get down to the low 10s of nm they get complex and expensive. For instance, an industrial system using an excimer laser is described utilizing an objective with 30 lenses of purified quartz.<sup>28</sup> Photolithography is thus more suited to high production of arrays of nanofeatures rather than prototype nanodevice fabrication.

Electron beam (e-beam) lithography is a widely used method for creating nanofeatures on surfaces. In a typical e-beam procedure, a resist is spread onto the substrate. The resist is then patterned with the e-beam, leaving bare substrate features. Metal is then deposited on the surface and then the resist etched away. Metal on the resist is also removed, leaving only the metal in contact with the substrate. This technique can fabricate nanostructures down to the tens of nanometers in size. For example, researchers have demonstrated the ability to form gold electrodes of around 30nm in width very close to one another.<sup>29</sup> A small drawback is that e-beam lithography must be performed in vacuum, but a more important issue is that this method requires a resist, which limits flexibility in nanodevice formation. Components in a nanodevice may need to be wired together after they are placed; placing a resist layer over them and then etching it away could damage or alter them.

Nanoimprint lithography is another technique used to form nanostructures. This technique requires a prefabricated template, which is generally pressed into a resist applied to the substrate. The resist is then cured or activated and the template removed, leaving its imprint in the resist. This method can also form nanostructures on the order of tens of nanometers, and can

make many features at once.<sup>30,31</sup> Due to using a template, placement on the substrate is far less controllable, however, and the method also suffers from having to use a resist.

Dip-pen nanolithography (DPN) is a so called additive scanning probe microscopy technique that is performed with an atomic force microscope (AFM). An AFM tip is loaded with molecules to be written onto the substrate. When the tip is brought to the surface, a meniscus of water is formed between them. The molecules on the tip then enter the meniscus and are deposited on the surface as the tip is scanned over it. One method to form metallic nanofeatures with DPN is to apply protective molecules onto a very thin metallic layer, then etch the layer away. The deposited molecules prevent the etching of the metal underneath them. This has been demonstrated to connect gold electrodes to CNT.<sup>32</sup> In this case the CNT were not affected by the metal deposition and removal, but other components could be more sensitive. Another method is to load the tip with metallic nanoparticles. This has been shown with gold nanoparticles on silicon substrates.<sup>33</sup> These nanoparticles were able to be controllably deposited on the surface with feature widths around 100 nm, however, the gold nanoparticles would only deposit on hydrophilic surfaces. This could limit the utility of the method for metallic nanofeature formation. Also, in order to form a functional contact, a feature of nanoparticles would have to be fused by post-treatment steps. While the DPN method was not studied in the presented work, it is acknowledged that DPN has potential to form metallic nanofeatures with the desired flexibility if these limitations can be addressed.

The work presented in the first part of this dissertation utilizes other scanning probe microscopy lithographic methods. Using an AFM, surface chemistry can be altered as the tip scans. The tip can be used to dig out molecules from the surface, leaving a trough behind. This is known as nanoetching or nanoshaving. If this etched area is exposed to molecules that will

react to the underlying surface, it can be filled in with these new molecules.<sup>34</sup> The result is a patterned area of grafted-in chemistry in a field of the preexisting chemistry. Known as nanografting, the size of features made by this procedure are limited by the size of the tip used to create them. For instance, researchers have shown the ability to form nanoshaved patterns in a bovine serum albumen monolayer with widths from hundreds of nm down to 15 nm.<sup>35</sup> They were able to use these patterns to graft in lipids to form a bilayer down to 55 nm in width. While this example shows good feature size, the features themselves are straight lines. To display the ability of AFM based methods to form arbitrarily shaped features, other researchers have used nanoetching and grafting technique in combination with computer-aided design to write a quotation into a monolayer with feature widths of less than 20 nm.<sup>36</sup> Here they have patterned in mercaptohexadecanoic acid into a mixed monolayer of hexanethiol and octadecane thiol. Their pattern is shown in Figure 1.3, displaying the arbitrary shape of features that can be formed by this method.

In addition to mechanically modifying surfaces, AFM can also be used to

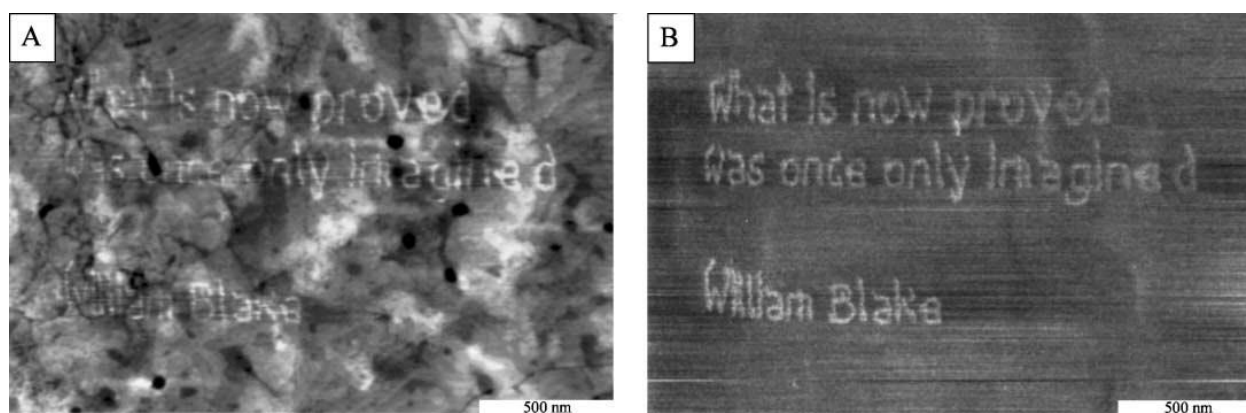


Figure 1.3 Pattern of mercaptohexadecanoic acid in a mixed monolayer of hexanethiol and octadecanethiol. A) Topography image and B) lateral force image. This shows the ability to form arbitrarily shaped patterns with the nanoetching and grafting method. Reprinted from *Appl. Surf. Sci.*, 175-176, S. Cruchon-Dupeyrat, et al., Nanofabrication using computer-assisted design and automated vector-scanning probe lithography, 636-642, Copyright (2001), with permission from Elsevier.

electrochemically modify them. In a process known as oxidative nanolithography or constructive nanolithography,<sup>37</sup> a conductive tip is used to modify the surface by applying a bias between the surface and the tip. The resulting pattern size is limited by a water meniscus that forms between the tip and the surface, and is again on the order of tens of nanometers. Researchers have used this technique to form oxidized patterns in monolayers on silicon oxide, and subsequently deposit silver on those features.<sup>38</sup> Their initial features were around 50 nm in width, but were broken up into nanoparticles. A silver enhancer solution was then used to complete the features, though this increased their widths as well. This method also has the potential to form arbitrarily shaped nanofeatures, and is further developed in the presented work.

From the methods outlined above, nanoetching/grafting and oxidative lithography are the methods used in this work, as they offer the most potential for forming metallic nanofeatures of arbitrary shape and size. DPN, also an AFM based method, shows some potential as well, but is beyond the scope of this work. While these AFM based techniques are slow throughput, they offer a very high amount of control in placement and shape, as the surface can be imaged, then immediately patterned, then imaged again using the same tip.

### **1.3 Adsorbates on Graphene-Like Materials**

In addition to nanofabricating features for use in nanodevices, it is also important to be able to investigate their properties. In the second part of this work, nanofeatures of molecules and nanoparticles are formed on a graphite surface. The graphite surface serves as a model for other graphene-like materials. As mentioned previously, graphene and other graphene-like materials possess very interesting electronic properties. Graphene, being only one atomic layer thick, is very electronically susceptible to the influence of adsorbates and even the substrate it is

placed upon. These act as dopants, either n-type or p-type, and cause the graphene to behave as either more metallic or more semiconducting. Researchers have found that placing graphene on an amine terminated monolayer has a different effect than on a fluorinated terminal group.<sup>39</sup> The effect of these substrates was to n-dope and p-dope, respectively, the graphene sheets. A number of studies have looked at this doping effect through surface potential mapping experiments. In them, a conducting AFM probe is used to measure both the topography and surface potential of the graphene and adsorbate surface in the same scan. In one such experiment, researchers adsorbed two different molecules, 2,3,5,6-tetrafluoro-7,7,8,8-tetracyanoquinodimethane (F4-TCNQ) and vanadyl-phthalocyanine (VOPc), onto graphene sheets.<sup>40</sup> They were able to show that the F4-TCNQ molecules pulled electrons from the graphene, p-doping it, while the VOPc molecules donated electrons, n-doping it. The ability to fine tune this adsorbate-graphene interaction will be of benefit in designing nanodevices incorporating graphene-like materials.

The present research investigates a novel system, azulenic compounds on graphite, and also differently shaped gold nanoparticles on graphite. Azulene is an aromatic compound composed of fused 7 membered and 5 membered rings. This gives azulene the interesting property of having the probability distribution for electrons in its HOMO and LUMO energy levels concentrated on different carbons in the ring structure. These azulenic compounds offer a powerful tool for controlling the type of doping, as their HOMO and LUMO energy levels are very tunable by placing functional groups on different carbons in the structure.<sup>41</sup> In addition, the molecules adhere to the surface without the need for a covalent bond due to strong  $\pi$ - $\pi$  stacking. Covalent bonds interrupt the very nature of the graphenic material; changing too many of the  $sp^2$  carbons to  $sp^3$  carbons has a detrimental effect on the graphene-like materials' unique electronic properties. Metallic nanoparticles on graphene-like materials have been researched before, but

here we look at different shapes of gold nanoparticles. There is evidence that different shapes have different optical properties; researchers have looked at gold tetrahedral, icosahedral, and cubic nanoparticles.<sup>42</sup> They found that each one had slightly different optical properties. Here, we investigate octahedral, spherical, and star-shaped gold nanoparticles to determine if they have a different effect on the graphite surface.

What we have shown here is that these AFM based methods offer a way to achieve nanometer scale control and positioning when nanofabricating patterns, and also offer a way we can probe the electronic properties of nanostructures at that same level. With a better understanding of the interaction of materials at the nanoscale, we can design and fine tune more complex nanodevices.

## **1.4 Overview**

Important aspects of nanofabrication are mainly controllability and size. The motivation behind some of the research presented in this dissertation is to explore and advance a method of constructing metallic nanofeatures in a very controlled fashion, forming them with highly directed placement, shape, and size. This kind of controllability has importance in novel nanodevices and circuitry and is described in Chapter 3.

As mentioned briefly in 1.3, graphene-like materials are currently a much focused on topic in research. The rest of the research in this dissertation is motivated by a need to understand how molecules and nanoparticles adsorbed onto graphene-like materials change the properties of these materials. Many devices have been fabricated using graphene and carbon nanotubes, and understanding how adsorbates affect the electronic properties of these materials

at the nanoscale will help future designers of these devices fine tune the properties to suit their specific needs.

Chapter 2 is an overview of the basic instrumentation and techniques used for all research presented. Self-assembled monolayers (SAMs) and their properties allow for excellent control over the chemistry and properties of surfaces. Ellipsometry is a potent tool that allows angstrom level precision in thickness measurements of thin films. Goniometry allows determination of the hydrophobicity/hydrophilicity of surfaces and so, probes the chemistry at the surface. SAMs, ellipsometry, and goniometry combine to offer a very powerful method to control surface chemistry and physical properties to suit our needs. The AFM is the workhorse instrument for this research. Under the right conditions, the AFM can reach sub-nanometer imaging resolution. This enables us to probe nanostructures and features in high detail. In addition to its strong imaging capabilities, the AFM can be used to modify nanoscale areas on the surface, both chemically and physically. It can also image more than topography, and is also used in this research to create maps of surface potential.

Chapter 3 details the progress made in forming and characterizing copper nanostructures on gold and silicon substrates. The AFM is used as a nanolithographic tool to change the chemistry of SAMs on these substrates very controllably on the tens of nanometers scale. These modified surfaces are then exposed to electroless copper plating solutions. The copper selectively plates out first on the patterned regions on the surfaces. These nanostructures are then characterized by the same AFM that created the patterns.

Chapter 4 describes the investigation of azulene compounds and gold nanoparticles adsorbed onto a graphite surface. This system serves as a starting point for research into other

graphene-like materials, graphene and carbon nanotubes. This research furthers knowledge of how adsorbates affect the electronic properties of graphene-like materials. Various azulene compounds with different substituents are adsorbed onto the surface of this graphite, and their nanostructure and surface potential mapped with the AFM. In addition, some gold nanoparticles and their effect on graphite are also studied to investigate the effect of shape on their interaction with the substrate.

Chapter 5 concludes the research presented and sums up the state of the projects. Future work, both short and long term, is offered. For the copper nanostructures research, we have shown the ability to form nanopatterns of chemistry with widths in the low 10s of nanometers. On these patterns, copper was successfully deposited on monolayers on both gold and silicon oxide substrates. Some of these copper nanofeatures have measured widths of 40 nm, confirming that this method has potential use for forming metallic features for use in nanodevices.

For the adsorbates on graphene-like materials work, we have shown that azulene compounds with different substituents interact differently with the graphite surface. Azulene and derivatives with electron withdrawing character on carbon positions that affect the HOMO level display behavior in the surface potential mapping experiments that suggests they pull electron density from the graphite, p-doping it. In contrast, an azulene derivative with electron donating character on the same carbon positions shows behavior that suggests electron donation from the molecules into the graphite, n-doping it. These data confirm that azulene molecules with different substituents can interact with graphene-like materials differently, lighting the way for their use as adsorbates to fine-tune the properties of graphene-like materials in devices.



Although it has been shown that differently shaped nanoparticles can have different optical properties, this work found no difference in their interaction with a graphite surface.

## References

1. Schmidt, R. H. M., *Ultra-Precision Engineering in Lithographic Exposure Equipment for the Semiconductor Industry*. Philos. T. Roy. Soc. A. **2012**, 370 (1973), 3950-3972.
2. Liu, J. Q.; Nakano, T., *Principles and Methods for Nanomechatronics: Signaling, Structure, and Functions Toward Nanorobots*. IEEE T. Syst. Man. Cy. C. **2012**, 42 (3), 357-366.
3. Hurst, S. M.; Farshchian, B.; Choi, J.; Kim, J.; Park, S., *A universally applicable method for fabricating superhydrophobic polymer surfaces*. Colloid Surf. A-Physicochem. Eng. Asp. **2012**, 407, 85-90.
4. Rubin, A.; Gauthier, C.; Schirrer, R., *The friction coefficient on polycarbonate as a function of the contact pressure and nanoscale roughness*. J. Polym. Sci. Pt. B-Polym. Phys. **2012**, 50 (8), 580-588.
5. Biener, J.; Wittstock, A.; Baumann, T. F.; Weissmuller, J.; Baumer, M.; Hamza, A. V., *Surface Chemistry in Nanoscale Materials*. Materials. **2009**, 2 (4), 2404-2428.
6. Schwierz, F., *Graphene transistors*. Nat. Nanotechnol. **2010**, 5 (7), 487-496.
7. Cuenya, B. R., *Synthesis and catalytic properties of metal nanoparticles: Size, shape, support, composition, and oxidation state effects*. Thin Solid Films. **2010**, 518 (12), 3127-3150.
8. Sandu, T., *Shape effects on localized surface plasmon resonances in metallic nanoparticles*. J. Nanopart. Res. **2012**, 14 (6).
9. Ríos, Á.; Zougagh, M.; Avila, M., *Miniaturization through lab-on-a-chip: Utopia or reality for routine laboratories? A review*. Analytica Chimica Acta. **2012**, 740 (0), 1-11.
10. Wei, D.; Bailey, M. J. A.; Andrew, P.; Ryhanen, T., *Electrochemical biosensors at the nanoscale*. Lab on a Chip. **2009**, 9 (15), 2123-2131.
11. Yu, C.; Irudayaraj, J., *Quantitative Evaluation of Sensitivity and Selectivity of Multiplex NanoSPR Biosensor Assays*. Biophysical Journal. **2007**, 93 (10), 3684-3692.
12. Moore, G. E., *Electronics* April 19, 1965.
13. Bernstein, K.; Cavin, R. K.; Porod, W.; Seabaugh, A.; Welser, J., *Device and Architecture Outlook for Beyond CMOS Switches*. Proc. IEEE. **2010**, 98 (12), 2169-2184.
14. Garner, C. M., *Lithography for enabling advances in integrated circuits and devices*. Philos. Trans. R. Soc. A-Math. Phys. Eng. Sci. **2012**, 370 (1973), 4015-4041.
15. Lu, C.-C.; Lin, Y.-C.; Yeh, C.-H.; Huang, J.-C.; Chiu, P.-W., *High Mobility Flexible Graphene Field-Effect Transistors with Self-Healing Gate Dielectrics*. ACS Nano. **2012**, 6 (5), 4469-4474.
16. Xu, F.; Wu, Y.; Zhang, X. Y.; Gao, Z. Y.; Jiang, K., *Controllable synthesis of rutile TiO<sub>2</sub> nanorod array, nanoflowers and microspheres directly on fluorine-doped tin oxide for dye-sensitized solar cells*. Micro Nano Lett. **2012**, 7 (8), 826-830.
17. Liu, J. W.; Kuo, Y. T.; Klabunde, K. J.; Rochford, C.; Wu, J.; Li, J., *Novel Dye-Sensitized Solar Cell Architecture Using TiO<sub>2</sub>-Coated Vertically Aligned Carbon Nanofiber Arrays*. ACS Appl. Mater. Interfaces. **2009**, 1 (8), 1645-1649.

18. Pan, H.; Qian, J. S.; Cui, Y. M.; Xie, H. X.; Zhou, X. F., *Hollow anatase TiO<sub>2</sub> porous microspheres with V-shaped channels and exposed (101) facets: Anisotropic etching and photovoltaic properties*. *J. Mater. Chem.* **2012**, 22 (13), 6002-6009.
19. Zhang, X.; Thavasi, V.; Mhaisalkar, S. G.; Ramakrishna, S., *Novel hollow mesoporous 1D TiO<sub>2</sub> nanofibers as photovoltaic and photocatalytic materials*. *Nanoscale.* **2012**, 4 (5), 1707-1716.
20. Seo, M. H.; Choi, S. M.; Seo, J. K.; Noh, S. H.; Kim, W. B.; Han, B., *The graphene-supported palladium and palladium–yttrium nanoparticles for the oxygen reduction and ethanol oxidation reactions: Experimental measurement and computational validation*. *Applied Catalysis B: Environmental.* **2013**, 129 (0), 163-171.
21. Li, M.-Y.; Liu, C.-L.; Shi, M.-R.; Dong, W.-S., *Nanostructure Sn–Co–C composite lithium ion battery electrode with unique stability and high electrochemical performance*. *Electrochimica Acta.* **2011**, 56 (8), 3023-3028.
22. S.M.-M. Dubois, Z. Z., X. Declerck, and J.-C. Charlier, *Electronic properties and quantum transport in Graphene-based nanostructures*. *The European Physical Journal B.* **2009**, 72, 1-24.
23. Hahnlein, B.; Handel, B.; Pezoldt, J.; Topfer, H.; Granzner, R.; Schwierz, F., *Side-gate graphene field-effect transistors with high transconductance*. *Appl. Phys. Lett.* **2012**, 101 (9), 093504.
24. Lee, S.; Yeo, J. S.; Ji, Y.; Cho, C.; Kim, D. Y.; Na, S. I.; Lee, B. H.; Lee, T., *Flexible organic solar cells composed of P3HT:PCBM using chemically doped graphene electrodes*. *Nanotechnology.* **2012**, 23 (34).
25. Park, H.; Afzali, A.; Han, S.-J.; Tulevski, G. S.; Franklin, A. D.; Tersoff, J.; Hannon, J. B.; Haensch, W., *High-density integration of carbon nanotubes via chemical self-assembly*. *Nat Nano.* **2012**, advance online publication.
26. Okuno, D.; Iino, R.; Noji, H., *Rotation and structure of FoF1-ATP synthase*. *J. Biochem.* **2011**, 149 (6), 655-664.
27. Wang, L.; Solak, H. H.; Ekinici, Y., *Fabrication of high-resolution large-area patterns using EUV interference lithography in a scan-exposure mode*. *Nanotechnology.* **2012**, 23 (30).
28. Seisyan, R. P., *Nanolithography in microelectronics: A review*. *Tech. Phys.* **2011**, 56 (8), 1061-1073.
29. Carcenac, F.; Malaquin, L.; Vieu, C., *Fabrication of multiple nano-electrodes for molecular addressing using high-resolution electron beam lithography and their replication using soft imprint lithography*. *Microelectron. Eng.* **2002**, 61-2, 657-663.
30. Guo, L. J., *Recent progress in nanoimprint technology and its applications*. *J. Phys. D- Appl. Phys.* **2004**, 37 (11), R123-R141.
31. Zhou, W. M.; Min, G. Q.; Zhang, J.; Liu, Y. B.; Wang, J. H.; Zhang, Y. P.; Sun, F., *Nanoimprint Lithography: A Processing Technique for Nanofabrication Advancement*. *Nano-Micro Lett.* **2011**, 3 (2), 135-140.
32. Wang, W. M.; LeMieux, M. C.; Selvarasah, S.; Dokmeci, M. R.; Bao, Z. A., *Dip-Pen Nanolithography of Electrical Contacts to Single-Walled Carbon Nanotubes*. *ACS Nano.* **2009**, 3 (11), 3543-3551.
33. Wang, W. C. M.; Stoltenberg, R. M.; Liu, S. H.; Bao, Z. N., *Direct Patterning of Gold Nanoparticles Using Dip-Pen Nanolithography*. *ACS Nano.* **2008**, 2 (10), 2135-2142.

34. Xu, S.; Liu, G. Y., *Nanometer-scale fabrication by simultaneous nanoshaving and molecular self-assembly*. *Langmuir*. **1997**, *13* (2), 127-129.
35. Shi, J. J.; Chen, J. X.; Cremer, P. S., *Sub-100 nm Patterning of supported bilayers by nanoshaving lithography*. *J. Am. Chem. Soc.* **2008**, *130* (9), 2718-+.
36. Cruchon-Dupeyrat, S.; Porthun, S.; Liu, G. Y., *Nanofabrication using computer-assisted design and automated vector-scanning probe lithography*. *Applied Surface Science*. **2001**, *175-176* (0), 636-642.
37. Maoz, R.; Frydman, E.; Cohen, S. R.; Sagiv, J., *"Constructive nanolithography": Inert monolayers as patternable templates for in-situ nanofabrication of metal-semiconductor-organic surface structures - A generic approach*. *Adv. Mater.* **2000**, *12* (10), 725-+.
38. Hoeppeener, S.; Maoz, R.; Cohen, S. R.; Chi, L. F.; Fuchs, H.; Sagiv, J., *Metal nanoparticles, nanowires, and contact electrodes self-assembled on patterned monolayer templates - A bottom-up chemical approach*. *Adv. Mater.* **2002**, *14* (15), 1036-+.
39. Wang, R.; Wang, S. N.; Zhang, D. D.; Li, Z. J.; Fang, Y.; Qiu, X. H., *Control of Carrier Type and Density in Exfoliated Graphene by Interface Engineering*. *ACS Nano*. **2011**, *5* (1), 408-412.
40. Wang, X. M.; Xu, J. B.; Xie, W. G.; Du, J., *Quantitative Analysis of Graphene Doping by Organic Molecular Charge Transfer*. *J. Phys. Chem. C*. **2011**, *115* (15), 7596-7602.
41. Shevyakov, S. V.; Li, H.; Muthyala, R.; Asato, A. E.; Croney, J. C.; Jameson, D. M.; Liu, R. S. H., *Orbital Control of the Color and Excited State Properties of Formylated and Fluorinated Derivatives of Azulene†*. *The Journal of Physical Chemistry A*. **2003**, *107* (18), 3295-3299.
42. Dong, J. Z.; Zhang, X. L.; Cao, Y. A.; Yang, W. S.; Tian, J. G., *Shape dependence of nonlinear optical behaviors of gold nanoparticles*. *Mater. Lett.* **2011**, *65* (17-18), 2665-2668.

## **Chapter 2: General Methods and Instrumentation**

### **2.1 Overview**

This chapter describes methods and instrumentation used for the research presented in this dissertation. Self-assembled monolayers (SAMs) are used to very effectively control surface properties and chemistry. They are also used as resists for nanolithography. Goniometry and ellipsometry are used to characterize SAMs and surfaces. Goniometry is the measurement of the contact angle of a droplet and a surface. Here, water contact angles are used to characterize the hydrophobicity/hydrophilicity of SAMs and surfaces. Ellipsometry is a tool for obtaining angstrom level precision in the thicknesses of thin films. This method uses the reflection of elliptically polarized light to measure the optical properties of a surface, which can be used to calculate the thickness of films on that surface. Atomic force microscopy (AFM) is a powerful tool and instrument used to both characterize surfaces and features on the nanoscale, and to manipulate them on the nanoscale. Here it is used to measure topography, friction and surface potential, as well as form nanopatterns on surfaces.

### **2.1 Self-Assembled Monolayers**

Some of the most important tools used in the presented research are self-assembled monolayers (SAMs). SAMs are exactly what their moniker suggests, a single layer of molecules that assemble on a substrate. SAMs allow for controllable modification of surface chemistry.<sup>1</sup> They are a marvel in their ease of use and versatility. To form, the SAM molecules must be brought into contact with their substrate. The molecules must also have at least one end group that has an affinity for or will react with the substrate surface. Typical SAM-substrate systems are thiols on various metals,<sup>2</sup> carboxylic acids on titania,<sup>3</sup> silanes on silicon oxide,<sup>4</sup> and more.

Often, the substrate is simply placed in a solution containing a millimolar concentration of the SAM molecules and a well ordered monolayer forms within 24 hours. As the active group attaches or bonds to reactive sites on the substrate, the molecules start getting packed together. Van der Waals forces bring neighboring chains together, and over time almost all active sites on the substrate are occupied. Stabilized by these Van der Waals forces, good monolayers are formed with straight chain hydrocarbons, more than a few carbons long, with the surface active groups

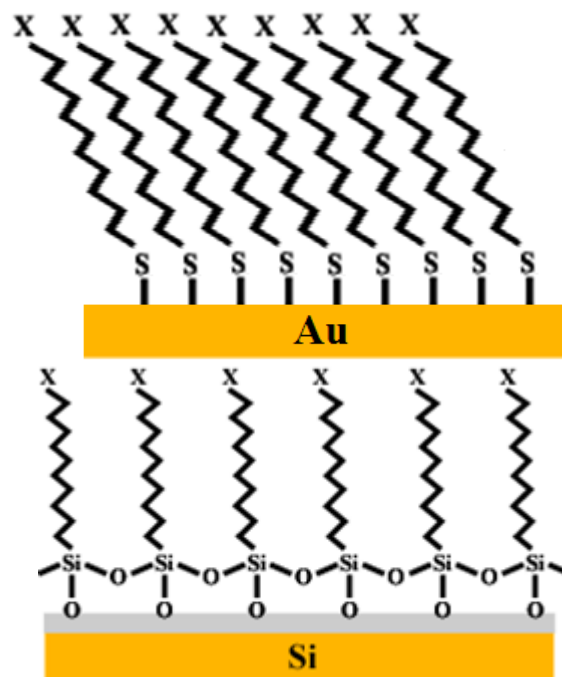


Figure 2.1 SAM-substrate systems used. Thiols on gold (top) and silanes on the native oxide of silicon (bottom).

on one end and a functional group on the other. The variable group can usually be chosen to fit the needs of the situation, although it shouldn't react with the substrate. In this research two substrates are used, gold surfaces and the native oxide surfaces of silicon, depicted in Figure 2.1. For gold substrates, thiol molecules are used to form SAMs, and for silicon oxide surfaces, silanes are used. Both systems have been extensively studied in the literature. The thiols on gold system offers ease of use, a variety of functional groups, and a conductive substrate. Functional groups used in this work include hydrophobic methyl groups and hydrophilic carboxyl groups. The silanes on silicon oxide system does not offer the ease of use that the thiols on gold system has, but monolayers are more robust due to the possible formation of multiple bonds to the substrate and other molecules. This system offers an insulating substrate,

ideal for forming and testing metal nanofeatures. Each system is discussed in more detail in the materials sections in later chapters.

## 2.2 Goniometry

Goniometers measure angles and, in the case of surface science, are usually employed to measure the contact angle of a liquid droplet on a substrate. As used here, water droplets' contact angles are measured on substrates to determine their hydrophobicity. This is done to help characterize SAMs,<sup>5</sup> as their end group

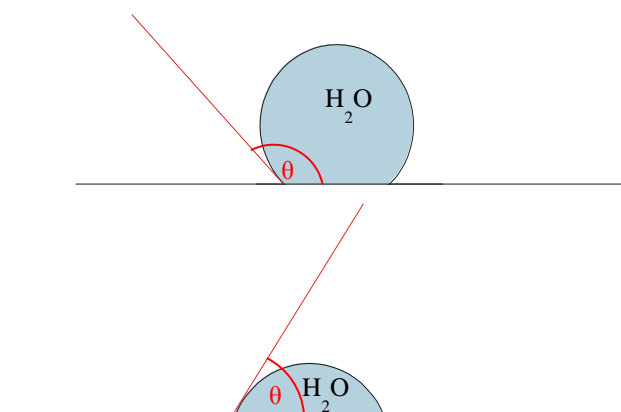


Figure 2.2 Representation of a contact angle ( $\theta$ ) measurement of a droplet of water on a hydrophobic surface (top) and a hydrophilic surface (bottom).

should dictate this property. SAMs of different chemistry can have very different values for water droplet contact angles. A methyl terminated SAM is hydrophobic, and should have a high contact angle,<sup>6</sup> whereas a carboxylic acid terminated SAM is very hydrophilic, and should have a low contact angle.<sup>7</sup> This is shown in Figure 2.2, and is due to the relative energies of the solid-liquid, solid-air, and liquid-air interfaces.<sup>8</sup> For a hydrophobic surface, the solid-air interfacial tension is less than the solid-liquid tension, and so the droplet balls up for a high contact angle. For a hydrophilic surface, the water is attracted to the surface as the solid-air interfacial tension is greater than the solid-liquid tension. Here the water droplet spreads out over the surface for a low contact angle. Goniometry can help in determining a change in chemistry at the surface, for instance, oxidation of a methyl terminated SAM should lower the measured contact angle, as the oxidized regions would be more hydrophilic. The goniometer used was a Ramé-Hart, Inc. NRL C.A. Goniometer.

## 2.3 Ellipsometry

Ellipsometry is used to measure changes in the optical properties of materials at interfaces. In the context of SAMs, it can be used to accurately and precisely measure the thickness of thin films such as SAMs. To do this requires knowledge of the index of refraction of both the substrate and the film. A single wavelength ellipsometer, such as the Rudolf Research AutoEL used in the presented research, consists of a light source, typically a laser, a set

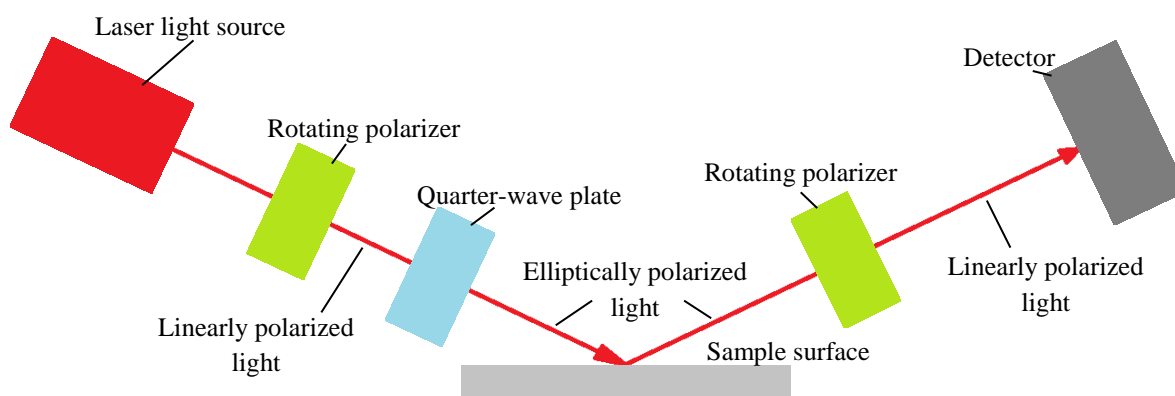


Figure 2.3 Diagram of an ellipsometer. The elliptically polarized light changes polarization upon reflection at the sample surface. This change contains information about the optical properties of the sample at that surface.

of polarizers, a compensator, and a detector. This is depicted in Figure 2.3. Light is directed through one of the polarizers, which is mounted such that it can be rotated. The light then passes through the compensator, a quarter-wave plate, and is now elliptically polarized. It is shined onto the surface at a specific angle of incidence;  $70^\circ$  was used in the presented work. Upon reflection, the polarity of the light changes as it interacts with the interface. Both p-polarized light and s-polarized light can change, but in different amounts. The second polarizer is positioned between the sample and the detector and is also rotatable. The two polarizers situated before and after reflection rotate, attempting to find a minimum in the intensity of the laser on the detector. From the angles of the two polarizers in relation to the quarter-wave plate, which is



fixed, the angles  $\Delta$  and  $\Psi$  can be calculated. The angle  $\Delta$  is the change in phase difference of the p and s polarized light before and after reflection, while the tangent of  $\Psi$  is the ratio of the magnitudes of the total reflection coefficients of the p and s polarized light. These angles, as well as the supplied indexes of refraction, are used to calculate the thickness of the film on the substrate using the fundamental equation of ellipsometry:

$$\tan \Psi e^{i\Delta} = \frac{R^p}{R^s} \quad \text{Eq. 2.1}$$

where  $R^p$  and  $R^s$  are the total reflection coefficients (functions of the film thickness) of the p and s polarized light and  $i$  is the imaginary number.<sup>9</sup>

Table 2.1 Ellipsometric Characterization of Thiol SAMs on Gold Substrates

Sample	n*	k*	Thickness (nm)*
Gold Substrate for DDT	0.177 ± 0.003	3.54 ± 0.02	-
Gold Substrate for ODT	0.19 ± 0.02	3.50 ± 0.04	-
DDT on Gold	-	-	1.1 ± 0.2
ODT on Gold	-	-	1.6 ± 0.4

\*error at one std. dev.

Example data are shown in Table 2.1. Here, the refractive index, n and k, for gold substrates was measured, and then SAMs of dodecanethiol (DDT) and octadecanethiol (ODT) were formed on the substrates. The thickness of each SAM was measured 6 times across the sample surface to get an average.

## 2.4 Atomic Force Microscopy

### 2.4.1 General Description

First described in 1986 by Binnig, Quate, and Gerber,<sup>10</sup> the atomic force microscope has enabled researchers to investigate and manipulate materials on the atomic and nanometer scale. The AFMs used for the presented research are Digital Instruments Nanoscope IIIa Multimode and Nanoscope E with Lateral Force mode atomic force microscopes. At an AFMs core is a piezoelectric material for very fine motion control in the x y and z axes. In the systems used for this work, the sample stage is mounted on top of the piezo. A small cantilever with a very small tip is brought close to the sample surface. The radius of curvature of most tips is on the order of nanometers. A laser is shone onto the back of the cantilever and the reflection is directed into a four quadrant photodetector. This photodetector setup can detect very small movements of the incoming laser beam, caused by very small movements of the cantilever. This motion is interpreted according to the operating mode of the AFM, such as contact mode or tapping mode.

#### 2.4.2 Contact Mode

In a contact mode AFM experiment, the tip is brought down into contact with the sample surface. The tip is then raster scanned over the sample surface, tracing the topography. As the tip encounters features on the surface, peaks and troughs, the force on the cantilever changes and it bends slightly. This causes a deflection of the laser beam going into the photodetector. In this mode, the system is directed to maintain a constant force between the tip and the sample and thus a constant deflection. In response to the change in deflection from the tip encountering topographical features, the sample is moved up or down by the piezo controlling the z axis motion to maintain the desired force, or deflection setpoint. This response versus tip location is mapped as the topography of the surface. Topographical images contain information about the physical features of surfaces and nanostructures and are used to characterize them. Contact mode can also be used to make lateral force or friction measurement, which contains information

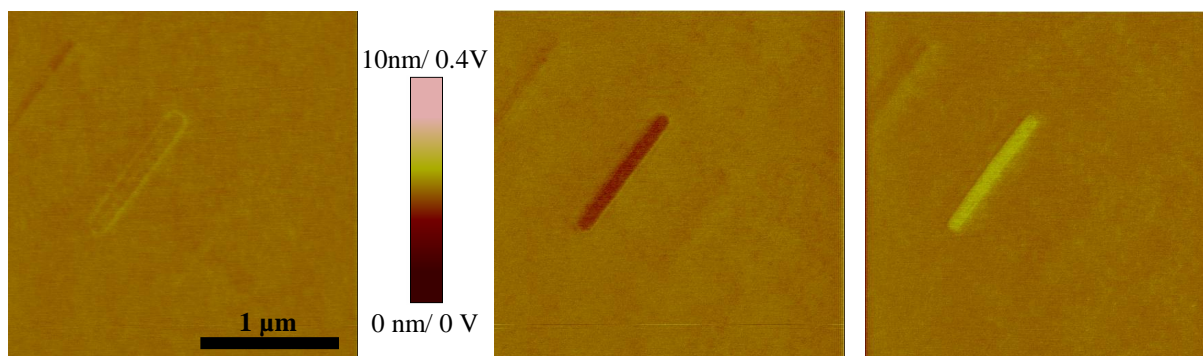


Figure 2.4 Topography (left) and friction trace (middle) and retrace (right) images of an oxidized nanopattern in an OTS SAM. The topography shows the physical features of the surface where the pattern is a slightly raised feature. The friction indicates that the chemistry is different inside and outside the nanopattern.

about changes in the chemistry at the surface. In this mode, the tip is scanned side to side, and as it interacts with the surface, it twists slightly due to friction. The tip has a different interaction across different surface chemistries, which causes the tip to twist to a more or lesser extent. This change in twist is mapped as a friction image. An example of topography and friction images is shown in Figure 2.4. Here, a nanopattern has been oxidized into an OTS monolayer. The topography shows a raised feature, while the friction images indicate that the chemistry has changed inside the pattern. The pattern was formed with oxidative lithography, which is detailed in Chapter 3.

### 2.4.3 Tapping Mode

Tapping mode differs from contact mode in that the tip is not dragged across the surface of the sample. Instead, a piezo inside the tip holder drives an oscillation of the cantilever very near the resonance frequency of that cantilever. The magnitude of the cantilever's oscillation is measured on the photodetector. As the oscillating tip approaches the surface, the oscillation is damped due to tip-sample interactions. The oscillating tip is then scanned over the sample surface. Similar to contact mode, this damped oscillation is set to a specific value; the sample is

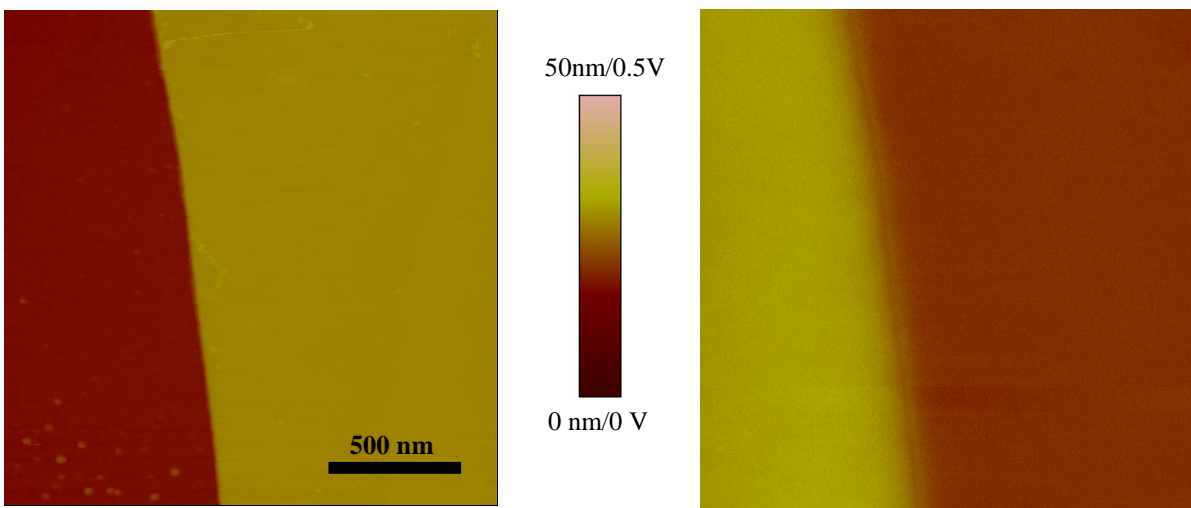


Figure 2.5 Topography (left) and surface potential (right) images of a flake of graphite on at OTS SAM. The topography shows the graphite flake as a plateau on the OTS surface, while the potential image maps out the electrostatic potential.

then moved up and down to keep the amplitude of oscillation constant. This response is mapped as the topography. Tapping mode can also be used in conjunction with a conductive tip to make surface potential maps. Here, the oscillation is driven by an AC bias applied to a conductive tip. This bias on the tip causes it to feel a force from the electrostatic potential of the surface. A DC bias supplied to the tip damps this force, and thus the oscillation. The DC bias required to minimize this oscillation matches the surface potential felt by the tip. This bias is mapped out as the surface potential map. This type of measurement is explained in much more detail in Chapter 4 for probing the electronic properties of azulene derivative molecules on graphite. An example image of topography taken with tapping mode and a surface potential image is shown in Figure 2.5. Here, a graphite flake is imaged on an OTS SAM. In the topography image, the flake is seen as a plateau above the OTS monolayer. The potential image maps out the electrostatic potential of the surface, indicating that the OTS SAM and the graphite surface have different potentials.

## 2.5 Implementation

The techniques and methods described in this chapter are the tools with which the research presented in this dissertation was performed. SAMs allow for chemical modification of surfaces, and can be manipulated by lithographic techniques to form nanopatterns. SAMs are used in Chapter 3 to great effect in this manner. Goniometry and ellipsometry are used to characterize these SAMs, and can also be used to monitor changes in surface chemistry. Finally, AFM is the main instrument used in both Chapters 3 and 4 to characterize and manipulate surfaces and nanofeatures. Contact and lateral force mode are used in Chapter 3 to characterize nanopatterns, while tapping mode is used to characterize copper nanofeatures. AFM is used in Chapter 4 to investigate the nanoscale physical and electrical interaction of adsorbates on graphite with both topographical, in tapping mode, and surface potential mapping.

## References

1. Schreiber, F., *Structure and growth of self-assembling monolayers*. Progress in Surface Science. **2000**, 65 (5–8), 151-257.
2. Kukhta, A. V.; Kukhta, I. N.; Kolesnik, E. E.; Lugovskii, A. P.; Neyra, O. L.; Meza, E., *Optical properties of thiol terminated biphenyloxazole ordered monolayers on gold surface*. Applied Surface Science. **2007**, 254 (1), 116-119.
3. Buckholtz, G. A.; Gawalt, E. S., *Effect of Alkyl Chain Length on Carboxylic Acid SAMs on Ti-6Al-4V*. Materials. **2012**, 5 (7), 1206-1218.
4. Tong, Y.; Tyrode, E.; Osawa, M.; Yoshida, N.; Watanabe, T.; Nakajima, A.; Ye, S., *Preferential Adsorption of Amino-Terminated Silane in a Binary Mixed Self-Assembled Monolayer*. Langmuir. **2011**, 27 (9), 5420-5426.
5. Tencer, M.; Nie, H.-Y.; Berini, P., *A contact angle and ToF-SIMS study of SAM–thiol interactions on polycrystalline gold*. Applied Surface Science. **2011**, 257 (9), 4038-4043.
6. Schmohl, A.; Khan, A.; Hess, P., *Functionalization of oxidized silicon surfaces with methyl groups and their characterization*. Superlattices and Microstructures. **2004**, 36 (1–3), 113-121.
7. Myrskog, A.; Anderson, H.; Aastrup, T.; Ingemarsson, B. r.; Liedberg, B., *Esterification of Self-Assembled Carboxylic-Acid-Terminated Thiol Monolayers in Acid Environment: A Time-Dependent Study*. Langmuir. **2009**, 26 (2), 821-829.
8. Adam, N. K., *USE OF THE TERM YOUNGS EQUATION FOR CONTACT ANGLES*. Nature. **1957**, 180 (4590), 809-810.
9. Tompkins, H. G., *A User's Guide to Ellipsometry*. ACADEMIC PRESS, INC.: San Diego, CA, 1993.
10. Binnig, G.; Quate, C. F.; Gerber, C., *ATOMIC FORCE MICROSCOPE*. Phys. Rev. Lett. **1986**, 56 (9), 930-933.

## Chapter 3: Nanofabrication of Nanopatterns and Copper Nanofeatures

### 3.1 Introduction

A method for forming highly directed and controlled metallic nanofeatures has implications in nanodevice and circuitry fabrication. Here, a method using nanoetching and grafting, oxidative lithography, and electroless plating to form copper nanofeatures has been advanced. Methyl-terminated self-assembled monolayers (SAMs) on both gold and silicon oxide substrates were used as resists to form carboxylic acid-terminated nanopatterns with nanoetching and grafting and oxidative lithography. These nanopatterns were then exposed to an electroless copper plating solution, selectively forming copper nanofeatures on the patterns. The copper nanofeatures formed on gold substrates had widths down to 210 nm, and on silicon oxide substrates down to 40 nm. Although the consistency of the copper nanofeatures formed can be improved, this represents a simpler method, requiring only patterning and solution-based plating steps, to form directed and controlled metallic nanofeatures than has previously been reported.

One of the goals in nanotechnology is to build fully functional, autonomous nanodevices. Although there has been much research devoted to the study of nanodevices,<sup>1, 2, 3</sup> the devices themselves are typically simple one component devices, such as nanotransistors<sup>4</sup> and nanocapacitors.<sup>5</sup> As these nanodevices continue to get smaller and their properties better understood, they will be taken to the next logical step, incorporation into a nanocircuit. The ability to form fully functional complex nanocircuitry will depend on our ability to form the wiring that will electronically connect the functional parts of the nanocircuit. To keep the device small, the wiring would have to be adaptable to fit any arrangement and also be very small itself. While current methods can produce metallic features on the order of tens of nanometers, they

either use a resist system, which can interfere with surface chemistry or features already present,<sup>6</sup> or form arrays of nanoscale features using templates, which are less flexible in regard to prototyping. What will be needed is a method to form conductive nanofeatures or wires within a few nanometers of where they are wanted and in the required dimensions, including height, without altering the rest of the surface. To do this, the method must involve either direct deposition of metal to form the features or introduce a nanopattern of new chemistry that will selectively react with a metal deposition system.

Current methods for forming nanopatterns on surfaces include photolithography,<sup>7</sup> electron beam (e-beam) lithography,<sup>8</sup> nano-imprint lithography, dip-pen lithography,<sup>9</sup> nano-etching and grafting,<sup>10</sup> and oxidative lithography.<sup>11</sup> Most of these methods have been used for some time, however, the nano-etching and grafting and oxidative lithography methods have not seen as much advancement towards forming metallic nanofeatures, but are increasingly becoming more relevant as their capabilities to form very small and directed nanofeatures are realized. These methods are briefly discussed here, focusing on their advantages and disadvantages.

In photolithography, light is used to pattern into a resist layer spread on the substrate. Typically, a mask is used to protect some of the resist from the light. With a positive resist, the light exposed areas are then able to be etched away, leaving the protected resist behind. This leaves the unprotected areas available for chemical modification or deposition, while leaving the still resist coated areas unaffected. With a negative resist, the light exposed areas are strengthened, and the unexposed areas can be etched away. Any technique that uses light in this way, however, will ultimately be diffraction limited. This limit was first described by Ernst Abbe in 1873 as:



$$d = \frac{\lambda}{2n \sin \theta} \quad \text{Eq. 3.1}$$

where  $\lambda$  is the wavelength of light,  $n$  is the refractive index of the medium, and  $\theta$  is half the angle of the maximum cone that can enter the lens;  $n \sin \theta$  is also known as the numerical aperture, NA. Mask projections under the diffraction limit cannot be resolved and thus would not form sharp patterns in the resist. There are ways to decrease the diffraction limit in a system, however, such as using light with a shorter wavelength, using a liquid medium with a higher refractive index, and objective design, while techniques such as multiple exposure get around the problem to an extent. The semiconductor industry is at the forefront of photolithography research and continues to push the boundaries as to what is possible. Current industry techniques use a 193 nm excimer laser, complex objectives, liquid immersion, and multiple exposure to lower the diffraction limit and obtain features on the order of tens of nanometers.<sup>7</sup> This is the method the Intel Corporation uses to manufacture their 22nm half-pitch microprocessors, with arrays of features with sizes down to 18 nm.<sup>12</sup> Although state of the art photolithography may offer good nanofeature size and control, the system expense and use of a resist, which may interfere with surface chemistry, discourage it from being used for prototype nanodevices.

E-beam lithography is a similar process to photolithography. Using a beam of electrons instead of light, patterns are drawn right into the resist without the use of a mask. The very short wavelengths of the electrons mean that the diffraction limit is not an issue at this scale. Here, limits in dimensions are caused not by diffraction, but by electron-electron repulsion and resists. The electron beam can be focused tightly, but the power must be lowered in order to do so because of this repulsion. The resist plays an important role as well. Resists that are tougher can

create more defined patterns, but take more energy to pattern, while softer resists can be patterned with lower power but are less defined and tend to deform.<sup>13</sup> Problems can also arise from surface charging and generation of secondary electrons that can affect feature size and the substrate itself. E-beam lithography can form patterns down to nanometer length scales with good precision,<sup>14</sup> but require the use of resists and high vacuum.

Dip pen nanolithography<sup>15</sup> (DPN) is a technique that uses an AFM probe tip to directly write molecules onto a substrate. The tip is first coated in the “ink” molecules to be written, either by dipping the tip into a neat liquid of the molecules or a solution of them. The tip is then brought into contact with the substrate, where a water meniscus forms between the tip and the substrate due to ambient humidity. The molecules on the tip diffuse off the tip into the meniscus, then onto the substrate as the tip scans. Systems include thiol molecules on a gold substrate or silanes on silicon oxide, and even proteins on nickel.<sup>16</sup> The resulting features can be on the order of tens of nanometers in scale<sup>17</sup> and are limited by the size of the meniscus. These nanofeatures can be used to bind other molecules, like protein or DNA for sensing applications.<sup>18, 19</sup> Because the tip itself is loaded with the ink molecules, it usually cannot be used to image the surface prior to deposition. This can limit the exact placement of the feature being writing with respect to anything already present on the substrate. Techniques can get around this, such as thermal DPN,<sup>20</sup> which uses molecules that will only leave the tip over a certain temperature so it can image cold and write hot. Another disadvantage is that the molecular ink used must travel through the water meniscus formed at the tip-surface interface. If the molecules are not water soluble, they may simply stick to the tip instead of diffusing to the surface.

Nano-etching and grafting<sup>21</sup> is also an AFM based technique. A SAM is formed on a substrate, such as a thiol monolayer on gold. The AFM tip is then used as a tool to disrupt the

interaction of the substrate and the molecules in the SAM. If performed in the presence of other molecules that will interact with the substrate, these other molecules will replace the molecules etched out. Feature size using this technique is only limited by the size of the contact area of the tip and the surface; feature sizes less than ten nanometers have been reported.<sup>10</sup> Direct placement of the pattern is possible with this method, since the surface can be imaged and then patterned with the same tip. Feature shapes are also arbitrary, allowing pattern shape, size, and position to be fully controllable.<sup>22</sup> For these reasons, this method was investigated as a potential technique for forming copper nanostructures in this work. A disadvantage is that nanoetching and grafting is not optimal for all SAM-substrate systems, namely very robust ones such as silanes on silicon oxide. Here, the monolayer molecules can bond with the substrate and each other, forming a layer that is very resistant to mechanical etching.

Finally, oxidative lithography, also known as local anodic oxidation<sup>23</sup> and constructive nanolithography,<sup>11</sup> is an AFM based method which relies on a conductive probe tip to oxidize the surface around the surface-tip contact point. What is thought to happen is when the tip reaches the surface, a meniscus of water forms between the tip and the surface. Although the process is not fully understood, it is thought that when enough of a negative bias is applied to the tip relative to the surface, water molecules split at the tip, forming ions including  $O^-$  and  $OH^-$ .<sup>23, 24</sup> The oxygen species travel through the meniscus to the top of the surface with help from the electric field. These ions react with the surface where, with the high bias and electric field from the tip, they can oxidize it.<sup>25</sup> Feature size with this method is limited by the size of the meniscus formed, much like dip-pen lithography. The meniscus size is very dependent on tip and humidity. Performed on a SAM with relatively inert chemistry, such as octadecyltrichlorosilane (OTS) with methyl terminal groups, it has been previously reported that these groups can be

oxidized into carboxylic acid groups, allowing for the formation of nanopatterns of a more reactive chemistry within an inert one.<sup>11</sup> Researchers exposed an OTS monolayer to a copper mesh and applied a negative bias to the mesh in relation to the sample. IR spectroscopy confirmed the formation of carbonyl stretches indicative of carboxylic acid groups in the monolayer after this oxidation step. As with nano-etching and grafting, this method allows for high control of pattern placement and arbitrary shape, since imaging and patterning can be done with the same tip. This method was also investigated as a potential technique for forming copper nanostructures.

To form metallic nanostructures using nanolithography methods that involve writing in a pattern of new chemistry requires a plating solution that will selectively plate the metal only on the new chemistry in the feature. We chose an electroless copper plating solution that preferentially plates out onto carboxyl groups over methyl groups.<sup>26</sup> Copper was chosen because it is relatively cheap and plentiful and electroless plating solutions of copper are reasonably understood.<sup>27</sup>

This research aims to advance a method utilizing nanoetching and grafting, oxidative lithography, and electroless copper plating to form copper nanostructures with high controllability in placement, shape, and size, while retaining their conductive properties. This method would have implications in the fabrication of novel nanodevices, such as the potential ATP synthase device discussed in Chapter 1, where placement and dimensions are critical to the proper function of the nanostructures in the device. Optimally, for use as nanowires, the features need to be as narrow as possible, yet still function as a wire. As a nanowire's diameter decreases, its resistance increases, due to electron scatter at the wire's surface and grain boundaries. It has been shown that copper nanowires of 30 nm diameter have resistivity of 3.58  $\mu\Omega$  cm, while those

of 15 nm diameter have resistivity of  $5.67 \mu\Omega \text{ cm}$  at 295 K.<sup>28</sup> These resistivities are greater than that of bulk copper,  $1.712 \mu\Omega \text{ cm}$  at 298 K, but still within the limits of decent conductivity. With this in mind, the some nanofeatures formed by the presented method were targeted at very small diameters, in the low 10s of nm range.

## 3.2 Materials and Methods

### 3.2.1 Self-Assembled Monolayer Formation and Characterization

SAM systems studied were octadecanethiol (ODT) and 11-mercaptoundecanoic acid (MUA) on gold substrates (Au.1000.SL1 Platypus) and OTS and 11-undecenyltrichlorosilane (UTS) on silicon(100) (Virginia Semiconductor Inc.) with a native oxide. The gold substrates were prepared by cutting roughly one square centimeter chips from a wafer with a scribe. These chips were rinsed with Millipure water ( $18 \text{ M}\Omega$  resistance) and then sonicated for 30 minutes in a 1:1 mixture of Millipure water and ethanol, then rinsed under chloroform, acetone, and ethanol. The refractive indexes of the gold films were measured with the ellipsometer, as they can differ from bulk gold values due to their thickness and structure. For forming ODT monolayers, the chips are placed in a saturated solution of ODT in ethanol ( $< 3 \text{ mM}$ ) at room temperature and left for at least 24 hours. The MUA molecules tend to dimerize in ethanol due to strong hydrogen bonding and form a bilayer on the gold surface. It has been found that using a 2% solution of trifluoroacetic acid in ethanol along with the MUA helps prevent this.<sup>29</sup> The solution used was 5 mM MUA and 2% trifluoroacetic acid in ethanol. Again, gold substrates were left in the solution for at least 24 hours, and can be stored in solution.

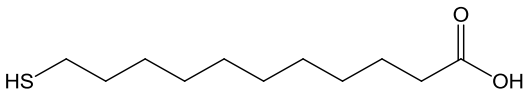
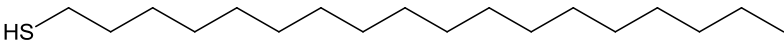
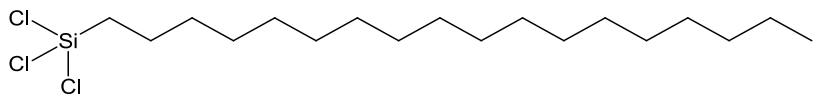
Silicon oxide substrates were prepared by cutting roughly one square cm chips from a wafer. These chips were then cleaned in a piranha solution, a 3:1 v/v solution of sulfuric acid

and 30% hydrogen peroxide in water. Caution must be exercised when handling piranha solution as it is very corrosive and will burn skin on contact. It must not be stored in a sealed container, as it generates gas. Upon mixing, the solution heats up, and the chips were added immediately after, as the heat aids in cleaning. The chips were left in this solution for 30 minutes, then rinsed with water and dried under nitrogen. The thickness of the native oxide was measured with the ellipsometer. The chips were then placed in 3 mM solutions of either OTS or UTS in toluene and left at room temperature for at least 24 hours, but no more than 48 hours. After allowing the monolayer to form, the chips were sonicated in toluene for 30 minutes and then sealed under nitrogen in individual vials for storage.

Prior to use, the SAMs on either substrate were characterized using ellipsometry and goniometry. For ellipsometry measurements, the refractive index of the substrate and the film were entered. The gold substrate indexes were measured previously and bulk silicon values were used for those substrates. For the SAM films, we used 1.45 for the refractive index, as this is the accepted value for typical hydrocarbons.<sup>30</sup> The goniometer was used to make simple static water droplet contact angle measurements to assess hydrophobicity and thus monolayer quality. Characterization values and molecule depictions are shown in Table 3.1 for SAMs used in this work. For static contact angle measurements, a droplet of Millipure water was placed on the surface, and the contact angle measured once on opposite sides. This was done three times for a total of 6 measurements. The thickness measurements were also done 6 times for each sample for an average monolayer thickness. The MUA SAM's contact angle agrees fairly well with a reported value for MUA SAMs formed in ethanol,  $28^\circ \pm 1^\circ$ ,<sup>31</sup> and the measured thickness is smaller than a reported value of  $1.8 \pm 0.1$  nm.<sup>32</sup> Both the contact angle and thickness for the ODT are smaller than previously reported values,  $114^\circ \pm 1^\circ$  and  $2.2 \pm 0.2$  nm.<sup>33</sup> The low

thickness indicates that the SAM may be slightly less well-formed, but the contact angles certainly indicate the expected surface chemistry, and so it was considered a good monolayer. The OTS data compared favorably with reported values of  $115^\circ \pm 1^\circ$  and  $2.4 \pm 0.2$  nm for the contact angle and measured thickness, respectively.<sup>34</sup>

Table 3.1 SAM Characterization

SAM	Static Contact Angle*	Film Thickness (nm)*
<p>MUA</p> 	$21^\circ \pm 3^\circ$	$1.05 \pm 0.03$
<p>ODT</p> 	$108^\circ \pm 1^\circ$	$1.93 \pm 0.04$
<p>OTS</p> 	$110^\circ \pm 2^\circ$	$2.77 \pm 0.05$

\*error at one std. dev.

### 3.2.2 Nano-Etching and Grafting

Nano-etching and grafting was attempted on both ODT SAMs on gold and OTS SAMs on silicon. This method is illustrated in Figure 3.1. For the ODT SAMs on gold, there is evidence indicating that if performed in air, the displaced thiol molecules simply move back into the etched region.<sup>35</sup> For this reason, it is necessary to do the nano-etching and grating under

fluid in the presence of the thiols to be grafted in. A glass fluid cell was used for this purpose which has channels for directing fluid in and out of the sample chamber. The chamber itself is open underneath and has a small metal clip for holding the

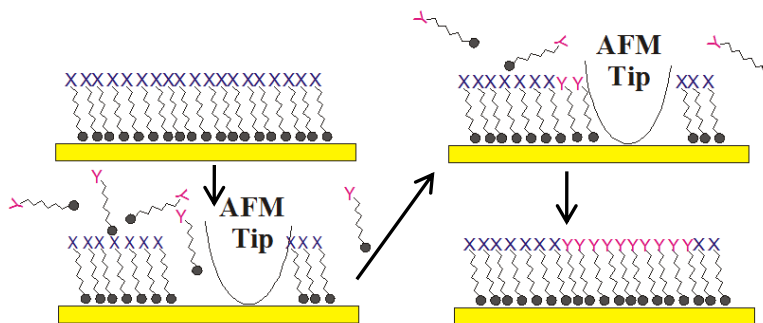


Figure 3.1 Depiction of the nano-etching and grafting method. The resist SAM (top-left) is etched into with the AFM tip. New molecules, indicated with a Y, fill into the open area on the substrate.

cantilever chip. An o-ring is used to form a seal on the surface of the sample and the cell. A 15 mM solution of MUA in ethanol was drawn into the fluid cell over the sample surface. The sample was imaged in contact mode, then the etching and grafting procedure was performed. The tip and cantilever used was silicon nitride with a spring constant of 0.35 N/m. The tip was pressed into the surface while scanning at an increased rate and force to form features 1  $\mu\text{m}$  long and tens of nm wide. Afterward, this area was imaged at 90° to produce a friction map of the nano-grafted area. Even though ODT are a little less than one nanometer longer than the MUA molecules, a topography change that slight is difficult to resolve on a rough surface. A change in friction, however, indicates that the chemistry has changed in those areas.

The OTS SAMs on silicon do not need to be etched under fluid. When the silane binds to the silicon oxide surface, it can form another two Si-O bonds with neighboring silanes. Unlike the thiols on gold system, the nano-etches into OTS can easily be imaged. The OTS monolayers are very robust, however, since they can polymerize with each other after bonding with the substrate, bonding with up to two neighbors or forming multiple bonds to the surface. This is demonstrated in Figure 3.2. This makes OTS SAMs notoriously difficult to etch using force-



based AFM methods. Here, attempts were made to etch into OTS with silicon nitride tips with stiff cantilevers. Scan sizes while etching were 1  $\mu\text{m}$  long and 32 nm wide. These areas were imaged in contact mode. Samples with etches were then exposed to 3 mM UTS in toluene solutions for grafting for 24 hours. These samples were subsequently imaged in contact mode to find evidence of grafting.

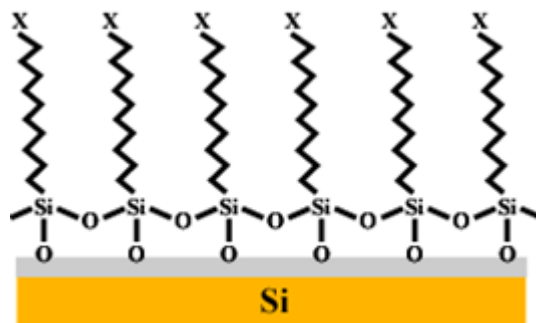


Figure 3.2 Silane molecules in a SAM. Each molecule can bond with the substrate and up to two neighbors.

### 3.2.3 Oxidative Lithography

The oxidative lithography method was used on both SAM systems. Samples were mounted on a steel puck and electrically connected with a silver particle solution or conductive adhesive. When loaded onto the AFM, the puck and sample are grounded. Platinum coated silicon probes (CSC11/Pt MikroMasch) with a reported radius of curvature of 25 nm were used for the oxidative lithography experiments. Whenever possible, the same tip was used to both image and oxidize features for consistency. When oxidizing with the tip, the voltage applied is the most critical factor. The exact bias needed, however, is dependent on the specific tip used and the relative humidity at the sample. Every time oxidative lithography was performed, the proper bias was found by an educated guess and check method. Biases too high would oxidize the monolayer right off the surface and lead to substrate oxidation; too low and there would be no change. Successfully oxidized features are those with contrast in friction with little or no topography change, as this change in height would indicate over-oxidation. Features were formed of various sizes, all in the tens to hundreds of nanometers range in width. To investigate

the role of tip velocity, number of scans, and bias on nanopattern formation and subsequent copper feature formation, these parameters were explored.

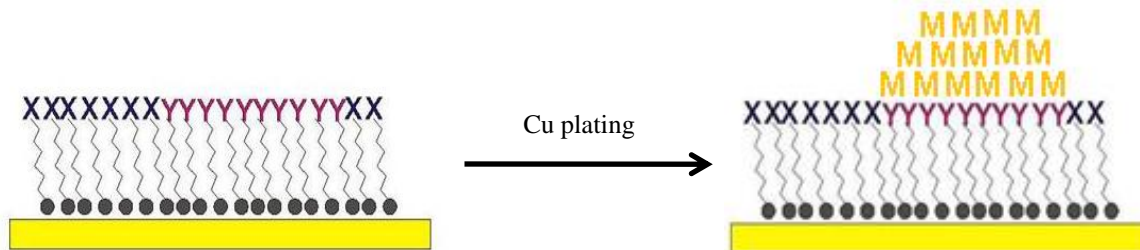


Figure 3.3 Depiction of copper electroless plating. Copper selectively gets reduced on the patterned in oxidized chemistry over the methyl terminated resist.

### 3.2.4 Electroless Copper Plating

After forming nanofeatures of oxidized chemistry in a layer of methyl terminated resist molecules, the samples were exposed to an electroless copper plating solution. A stock solution of 40 mM copper sulfate in water was made with copper sulfate pentahydrate (Sigma). One mL aliquots were taken from this stock solution and diluted with 9 mL Millipure water to make 10 mL of a 4 mM copper sulfate solution. To this, 0.124 grams of sodium tartrate dehydrate (Mallinckrodt) were added and allowed to fully dissolve. Next, 0.2 grams of sodium hydroxide (J. T. Baker) were added to raise the pH of the solution over 13. Finally, 200  $\mu$ L of 37 wt% formaldehyde in water (Sigma) was added to activate the solution. This solution was chosen because it had been used to form similar features<sup>26</sup> and the mechanism of the reaction has been studied. Although still not fully understood, it's thought that the copper(II) ions in solution complex with carboxylate ions at the surface. There, formaldehyde molecules reduce the copper ions one electron at a time to copper(0).<sup>27</sup> More copper(II) ions then get reduced on the copper(0), and the copper nanofeature forms.<sup>36</sup> This copper plating is depicted in Figure 3.3.

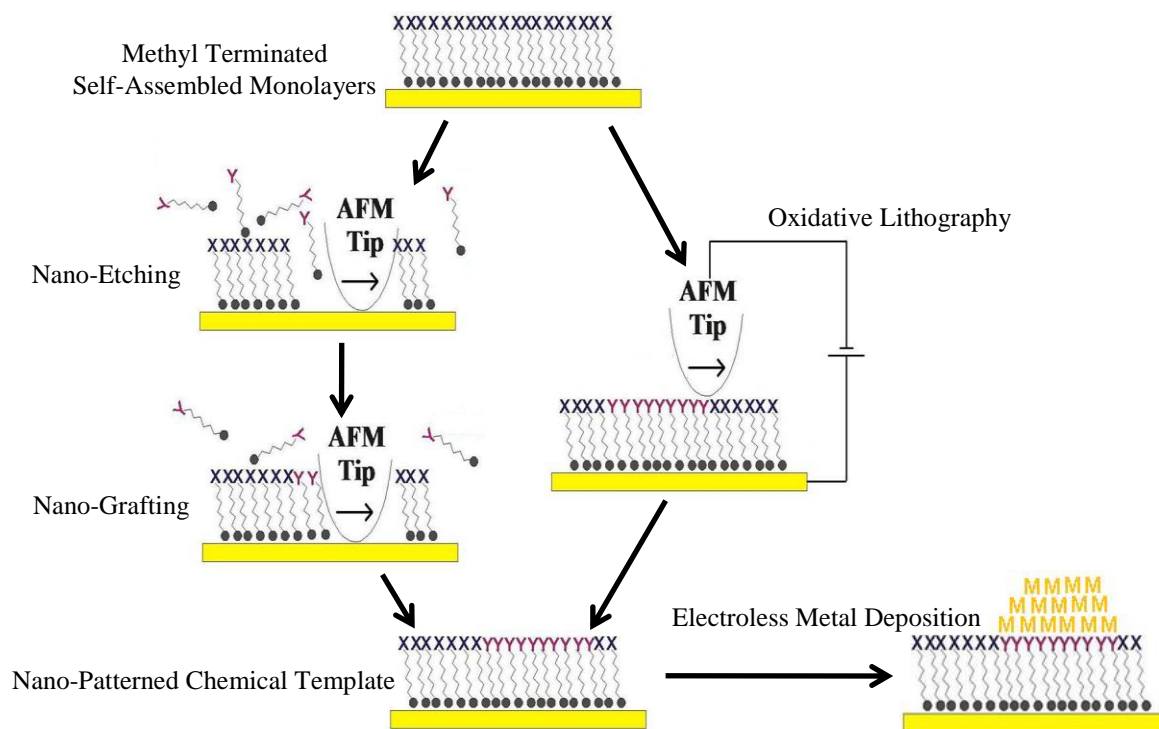


Figure 3.4 Scheme of the overall method of the presented work. Starting with SAMs of ODT on gold and OTS on silicon oxide, they are investigated in both nano-etching and grafting and oxidative lithography to pattern in an oxidized template. This pattern is then exposed to an electroless copper plating solution to selectively form copper nanofeatures on the oxidized template.

A scheme of the presented research is shown in Figure 3.4. Starting with a resist SAM of methyl terminated chemistry, both patterning methods, nano-shaving/grafting and oxidative lithography were investigated to form carboxylic acid nanopatterns. These nanopatterns were then reacted with an electroless copper plating solution, selectively depositing copper on the patterns. These patterns were formed on both ODT on gold and OTS on silicon SAM systems.

### 3.3 Results and Discussion

#### 3.3.1 Electroless Copper Plating Selectivity

To verify that the electroless copper plating solution was selective to carboxyl chemistry over methyl chemistry, an experiment was performed in which an ODT SAM on gold sample

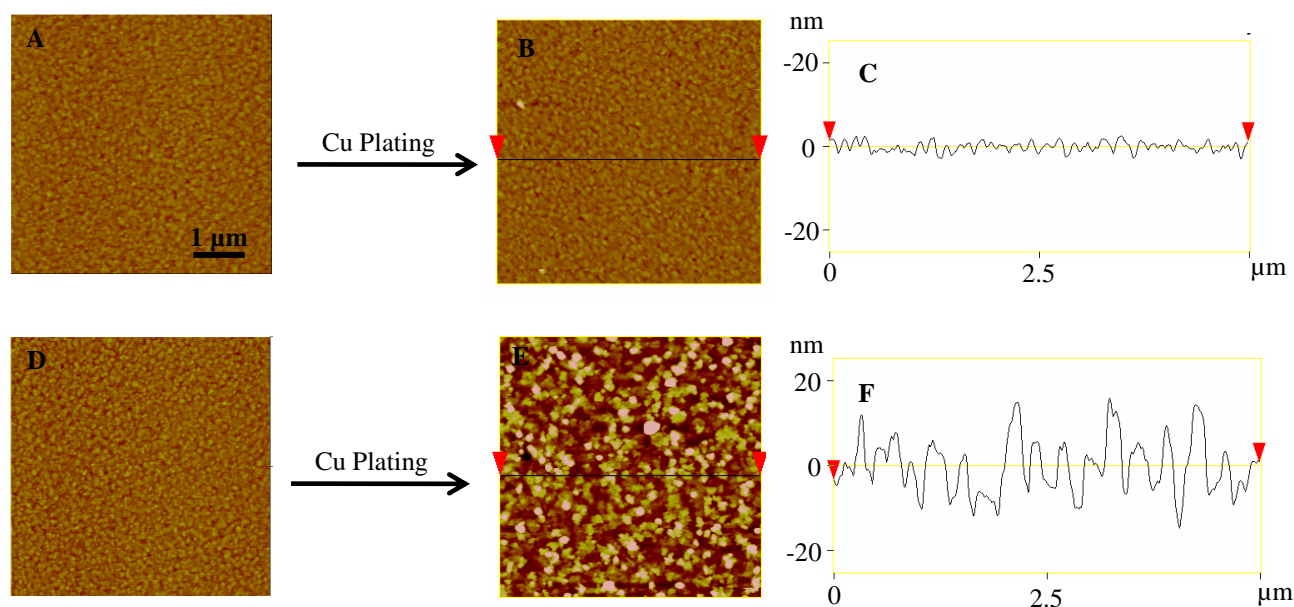


Figure 3.5 Topography images of an ODT and a MUA SAM before and after 10 minutes of exposure to the 4 mM  $\text{Cu}^{2+}$  electroless plating solution. A) ODT SAM before exposure. B) ODT SAM after exposure. There is almost no change in the topography, indicating very little copper deposition. C) A section through the surface in B. D) MUA SAM before exposure. E) MUA SAM after exposure. The topography is much rougher, indicating copper deposition across the surface. F) A section across the surface in E.

and an MUA SAM on gold sample were treated with the same 4 mM  $\text{Cu}^{2+}$  plating solution for ten minutes. AFM topography images were taken of the samples before and after treatment. The samples are indistinguishable before treatment, but afterward, the ODT sample appears almost unchanged while the MUA sample is very different. Topography images of these samples are shown in Figure 3.5. Upon a visual inspection, the ODT sample retained its gold color, while the MUA sample indeed took on a coppery hue. This confirmed that there is enough plating preference on the MUA over the ODT for selective deposition.

### 3.3.2 Nano-Etching and Grafting Results

Nano-etching and grafting were successfully performed on ODT monolayers, grafting in MUA molecules. Even though the difference in film thickness of ODT and MUA is just under 1 nm, these features can be hard to resolve on a rough surface. Instead, friction imaging was used

to locate and characterize the patterns. These can be quite narrow; features as small as 30 nm wide are demonstrated, as shown in Figure 3.6.

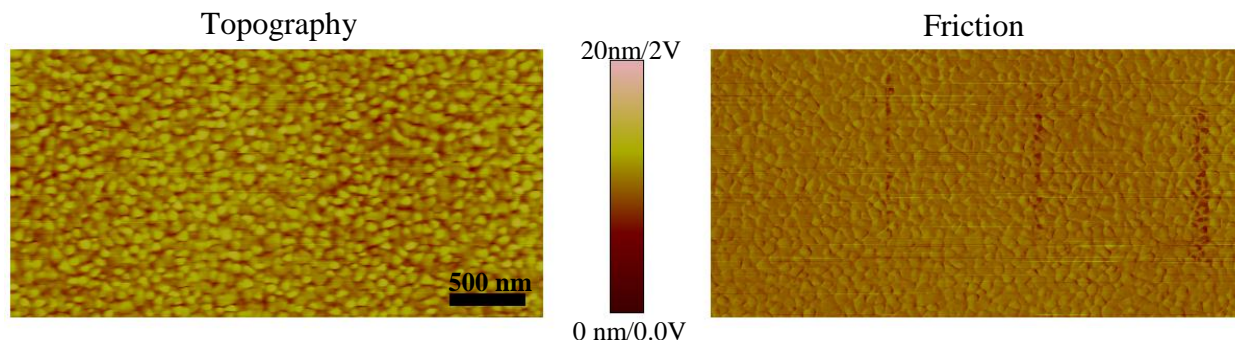


Figure 3.6 Topography (left) and friction (right) images of ODT on gold taken simultaneously in contact mode AFM after etching ODT molecules out and grafting MUA molecules in. The roughness of the topography image masks the change in height, though the friction contrast is very visible. Three nanopatterns of MUA have been grafted into the ODT later, the narrowest of which is 30 nm at its widest point.

Nano-etching and grafting into OTS on silicon, however, proved to be much more challenging. The OTS monolayer is very robust, so robust even, that it takes more force to break through the monolayer than it does to etch into the silicon oxide underneath it. Etching attempts either cut right through the monolayer and into the oxide, even down to the silicon, or barely

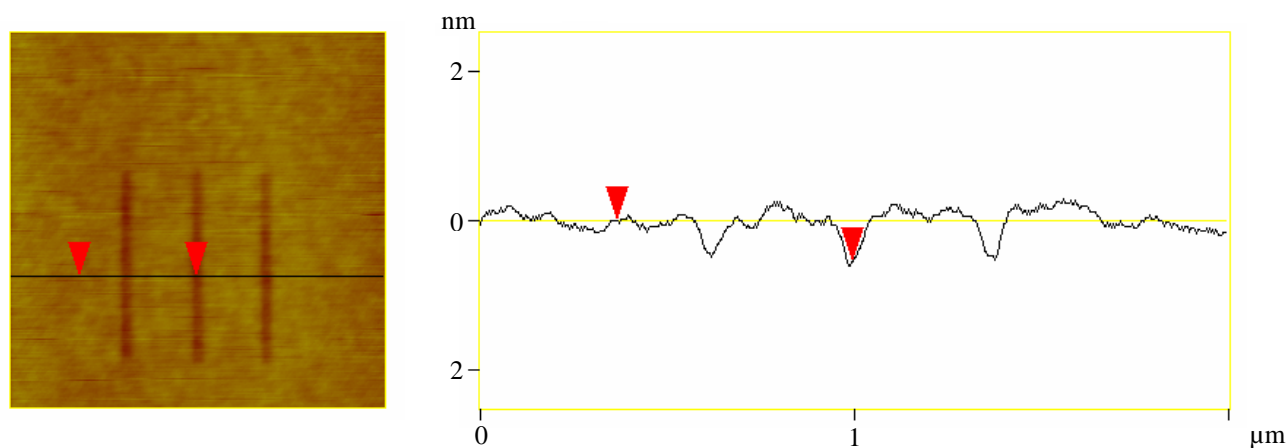


Figure 3.7 Topography image (left) and profile (right) of 3 neat etches into OTS on silicon oxide. The vertical distance between the two markers is 5.5 Å, much shorter than the thickness of the OTS SAM, 27.7 Å.

penetrate the OTS monolayer surface. In the latter case, the molecules in the SAM may simply be parting from the force of the AFM tip. These features were imaged and their depths were found to be around 0.55 nm, as shown in Figure 3.7, much less than the thickness of the OTS SAM. Nonetheless, these samples were exposed to a 5 mM UTS in toluene solution for 24 hours. The UTS molecules have a terminal carbon-carbon double bond, which can be chemically oxidized to carboxyl by permanganate.<sup>37</sup> Upon imaging the area of the features, they were no longer present. The UTS molecules are a little under 1 nm shorter than the OTS molecules, and had they grafted in to these etched patterns they would have been observable as depressions, given the low roughness of the surface. The reorganized molecules of the OTS SAM may have simply relaxed back to their original positions.

### 3.3.3 Oxidative Lithography Results

#### 3.3.3.1 Oxidative Lithography on ODT

Nanofeatures were successfully patterned into both ODT and OTS monolayers. As mentioned previously, the exact bias needed to oxidize the top of the SAM without oxidizing the surface is dependent on tip and humidity. Increasing humidity increases the size of the meniscus formed between the tip and the surface. A greater meniscus-surface contact area decreases the resolution of this method. In an oxidative lithography experiment, ODT on gold was patterned successfully with tip biases of -6.00 V and -6.50 V relative to the surface. Various features were formed with varying tip velocity and number of scans. These features are seen in Figure 3.8.

Pattern a was formed with a -6.00 V tip bias and 5.31  $\mu\text{m/s}$  tip velocity for about 800 passes for 2.5 minutes. This feature can be seen in both topography and friction images and is over-oxidized. The ODT molecules have been oxidized past the end group and down the carbon

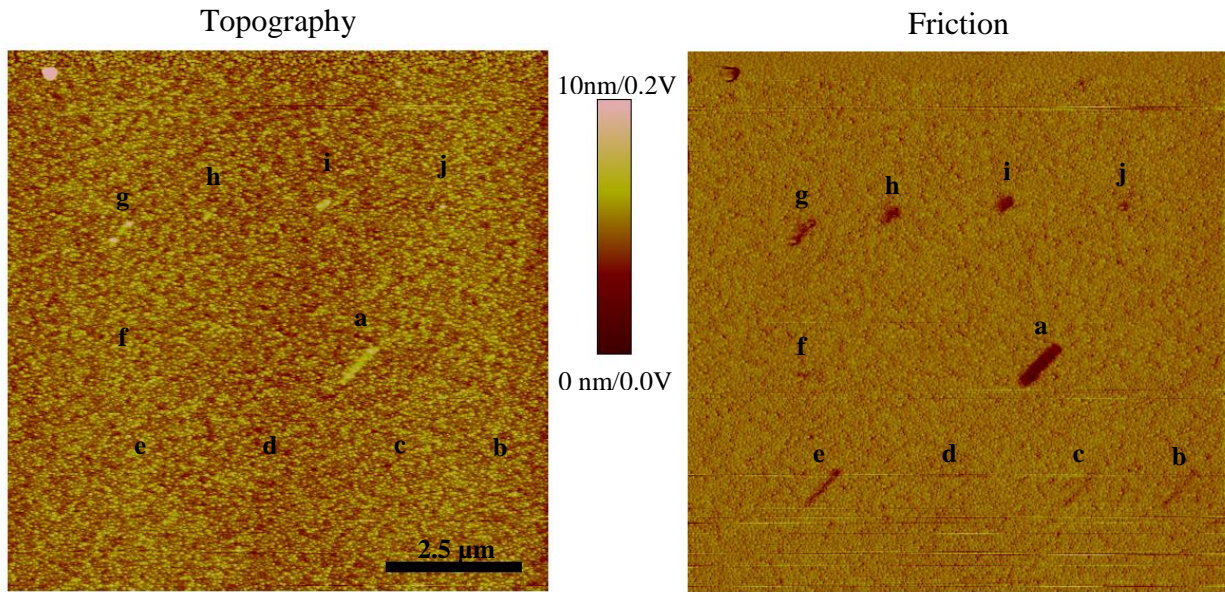


Figure 3.8 Topography (left) and friction (right) images of ODT on gold taken simultaneously in contact mode AFM after selectively oxidizing nanofeatures into the surface. Features that appear in both images have some substrate oxidation, while those that appear only in friction have little to none. a-f: -6.00 V tip bias, varying tip velocities and number of scans. g-j: -6.50 V tip bias, varying tip velocities and number of scans.

chain, and the substrate has been slightly oxidized, increasing in volume and creating a raised feature. Patterns b and c were formed also with a -6.00 V tip bias and 5.31  $\mu\text{m/s}$  tip velocity, but for about 160 passes for 30 seconds. These nanofeatures are clearly seen in the friction image but not in the topography. Pattern c is shown in more detail in Figure 3.9. This indicates a change in chemistry without a corresponding change in topography. Only the top of the monolayer has been modified.

Pattern e was formed with the same conditions as b and c, but with about 320 passes. This made for a stronger feature in the friction image still without forming a topographical feature, indicating little to no change deeper into the SAM. To investigate the role of tip velocity and scan time on pattern formation, pattern d was formed with the same tip bias as patterns b and c, but with a slower tip velocity, 0.2  $\mu\text{m/s}$ , and with only two scans for 10 seconds. As there are no features present in either the topography or friction for pattern d, no detectable oxidation

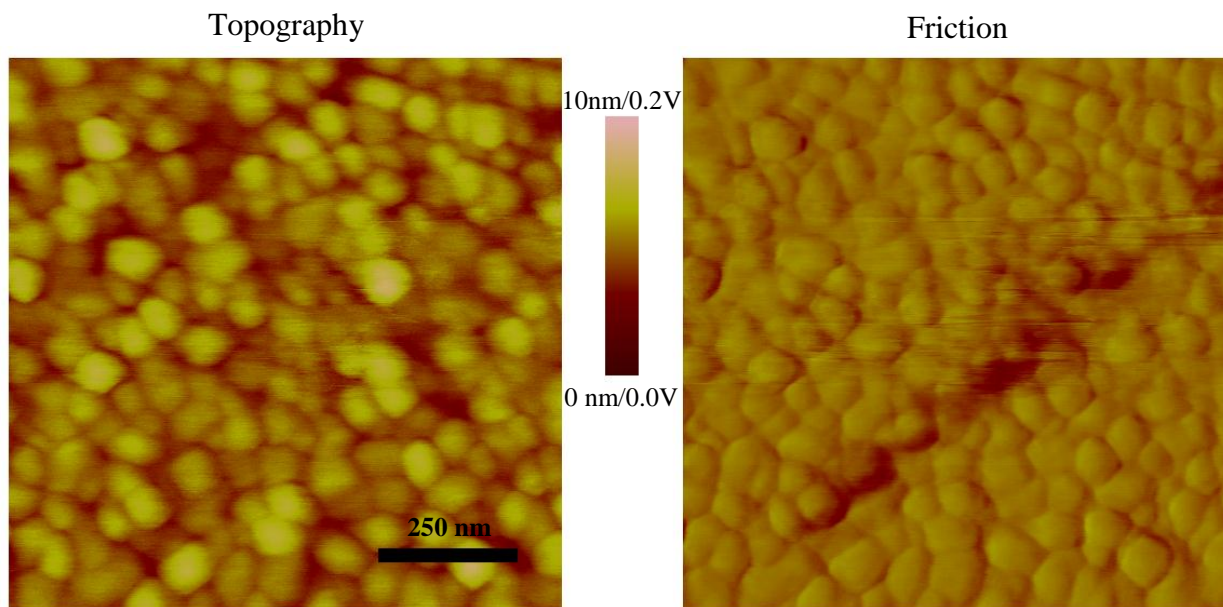


Figure 3.9 Topography (left) and friction (right) images of pattern c, formed with -6.00 V tip bias, 5.31  $\mu\text{m/s}$  tip velocity for about 160 passes. There is very little indication of a feature in the topography image, indicating oxidation of just the monolayer.

seems to have occurred. Pattern f was also formed with -6.00 V tip bias and 2 scans, but with an even slower tip velocity of 0.1  $\mu\text{m/s}$ , also for 10 seconds. The scan length was 500 nm. As indicated by Figure 3.8, pattern f shows a very slight feature in the friction image. The bias was increased to -6.5 V, and pattern g was formed otherwise identically to pattern f. Pattern g shows some topography as well as strong friction, indicating some over oxidation of the molecules.

Patterns h and i were formed at a -6.50 tip bias, but with different tip velocities and number of scans to further investigate tip velocity on oxidation. Pattern h was formed with a tip velocity of 1.33  $\mu\text{m/s}$  for about 55 scans, while pattern i was formed with a tip velocity of 0.05  $\mu\text{m/s}$  for 2 scans. Both patterns were formed in 10 seconds with lengths of 250 nm. Each pattern can be seen in the topography image in Figure 3.8, however pattern i shows a solid topographical feature, indicating strong over-oxidation of the film, compared to the weaker topographical feature for pattern h. Since each pattern was formed in the same amount of time,



10 seconds, this shows evidence that tip velocity may play a role in the rate of oxidation for this method. This could be if the meniscus changed shape at different tip velocities, though the literature is silent on the matter. Pattern j was formed as pattern i, but with only 1 scan. This feature is present very slightly in topography and is visible in friction, again indicating slight over-oxidation.

Table 3.2 Summary of patterned nanostructures presented.

Pattern	Tip Bias (V)	Tip Velocity ( $\mu\text{m/s}$ )	Number of Scans (approx.)	Topography Presence	Friction Presence
a	-6.00	5.31	800	Strong	Strong
b	-6.00	5.31	160	None	Present
c	-6.00	5.31	160	None	Present
d	-6.00	0.20	2	None	None
e	-6.00	5.31	320	None	Strong
f	-6.00	0.10	2	None	Present
g	-6.50	0.10	2	Strong	Strong
h	-6.50	1.33	55	Present	Strong
i	-6.50	0.05	2	Strong	Strong
j	-6.50	0.05	1	None	Present

Table 3.2 summarizes the results of the presented oxidative lithography on an ODT monolayer on gold. These data show that tip bias voltage, tip velocity, and the number of scans applied have a direct effect on the level of oxidation done by the tip. As can be expected, larger biases and increased number of scans increases oxidation. A slower tip velocity also increases oxidation, indicating tip and meniscus dwell time also play a role.

### 3.3.3.2 Oxidative Lithography on OTS

Similar experiments were performed on OTS monolayers. Features were formed again with varying tip biases, tip velocities, and scan numbers in order to sample a range of conditions. Figure 3.10 shows topography and friction images from an experiment in which 20 patterns were

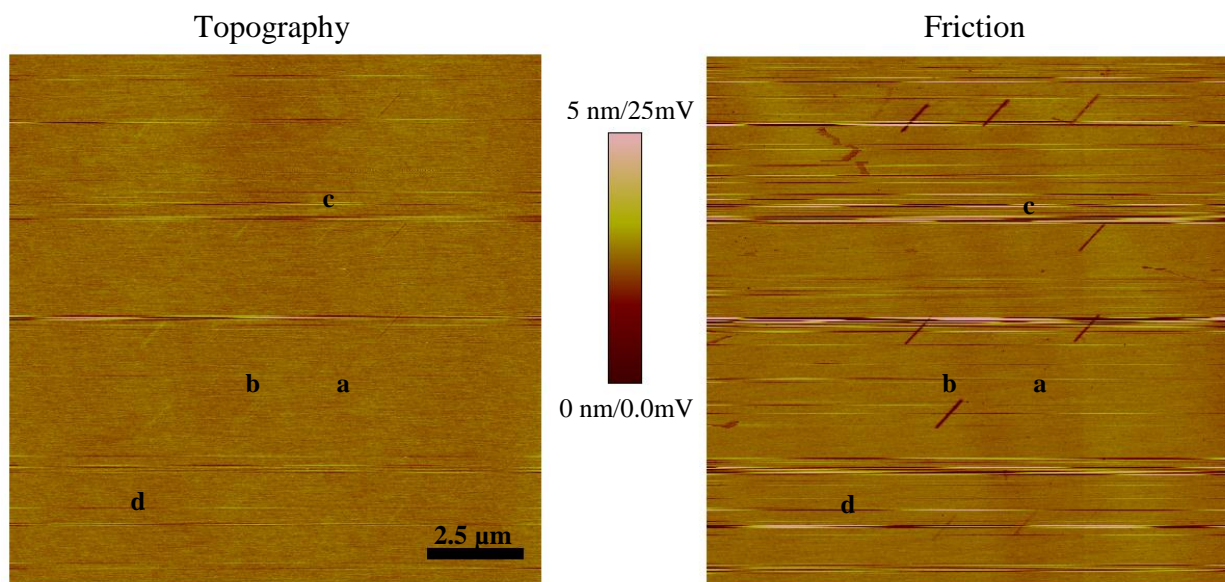


Figure 3.10 Topography (left) and friction (right) images of oxidized nanopatterns in an OTS monolayer on silicon oxide. Each of the 20 patterns was formed under different conditions, with varying tip biases, tip velocities, and number of scans. Representative patterns are labeled. a: formed with a -4.50 V tip bias, 5.31  $\mu\text{m/s}$  tip velocity, and about 1600 passes. b: formed with a -6.00 V tip bias, 5.31  $\mu\text{m/s}$  tip velocity, and about 800 passes. c: formed with a -5.50 V tip bias, 5.31  $\mu\text{m/s}$  tip velocity, and about 800 passes. d: formed with a -5.57 V tip bias, 0.20  $\mu\text{m/s}$  tip velocity, and about 20 passes.

drawn into an OTS monolayer with oxidative lithography. Different tip biases were sampled in order to find the optimal value as to oxidize the OTS without destroying it. Tip velocities and number of passes were then sampled to form a variety of nanofeatures. From the 20 features formed, 4 were selected as representing the types of features formed. These are labeled as patterns a, b, c, and d in Figure 3.10.

Pattern a was attempted with a tip bias of -4.50 V, a tip velocity of 5.31  $\mu\text{m/s}$ , and about 1600 passes for 5 minutes. Upon imaging the area, it was determined that no pattern was formed, as there was no indication in either topography or friction. With the high number of passes, it was concluded that -4.50 V is not a high enough tip bias for any detectable oxidation to occur. Pattern b was formed with a tip bias of -6.00 V, a tip velocity of 5.31  $\mu\text{m/s}$ , and about 800 passes for 2.5 minutes. This caused a noticeable change in topography and a very strong

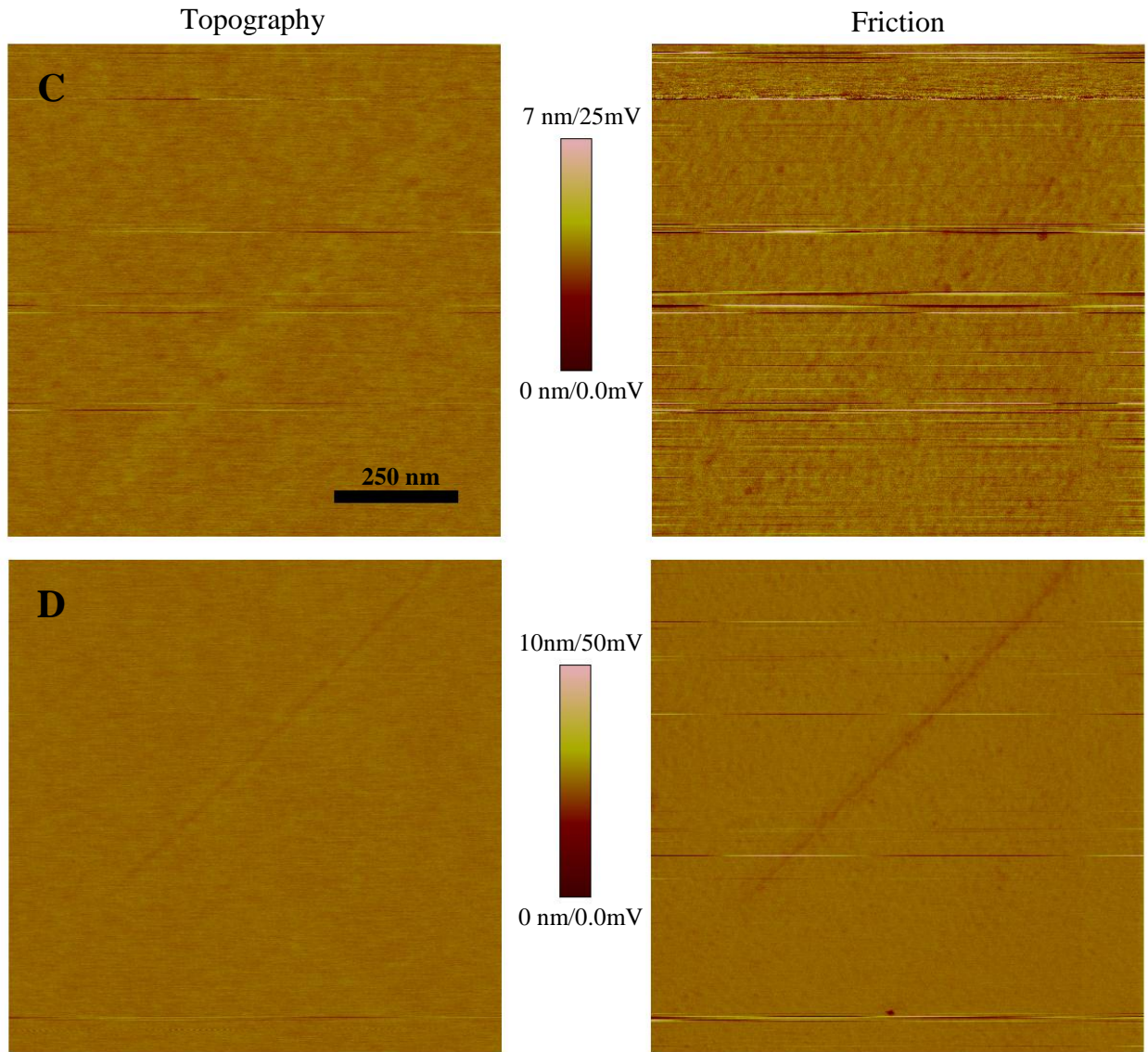


Figure 3.11 Topography (left) and friction (right) images of oxidized nanofeatures in OTS on silicon oxide, patterns c and d. C) pattern c showing very faint contrast in topography and friction. The OTS monolayer is slightly oxidized. D) pattern d is a very thin line (< 20 nm) of oxidation, showing a slight depression in topography, but a clear feature in friction.

pattern in friction. This pattern is an example of over-oxidation; the monolayer may have been damaged instead of oxidizing only at the top. Pattern c was formed with a tip bias of -5.5 V, a tip velocity of 5.31  $\mu\text{m/s}$ , and about 800 passes for 2.5 minutes. This pattern shows up very weakly in the topography and friction images. Only a slight oxidation has occurred here. Pattern d was formed with a -5.57 V tip bias, a tip velocity of 0.20  $\mu\text{m/s}$ , and about 20 passes for 1.7

minutes. This feature shows a very slight depression in topography, and a clear pattern in friction. This may indicate that the OTS molecules have been shortened by complete oxidation of their ends forming CO<sub>2</sub>, but not all the way down to the substrate, leaving the layer itself intact. This feature is also very thin, being just under 20 nm wide. This combination of tip velocity, number of passes, and thus scan time helped to decrease drift in the scanner while still allowing for oxidation. Patterns c and d are shown in detail in Figure 3.11. It is important to note that pattern c is almost imperceptible in both the topography and friction images. It is much less oxidized than pattern b but, as shown later in 3.4.4.2, still develops a discernible copper feature after the electroless plating process.

In comparison to the ODT on gold system, the thicknesses of the features on the OTS on silicon oxide seem to develop much more slowly, requiring many more passes to achieve the same level of oxidation, as indicated by friction images. They can, however, be formed with narrower widths. There is evidence that a current flow must accompany this method of oxidation.<sup>38</sup> Though current was not measured during oxidation, the fact that oxidation occurs much faster on a conductive gold substrate versus an insulating silicon oxide substrate seems to corroborate that idea. Differences notwithstanding, both systems were successfully patterned with oxidative lithography, forming nanoscale features of carboxyl terminated chemistry in a SAM of methyl terminated chemistry. These features were then exposed to the electroless copper plating solution.

### 3.3.4 Electroless Copper Plating Results

#### 3.3.4.1 Electroless Copper Plating on ODT

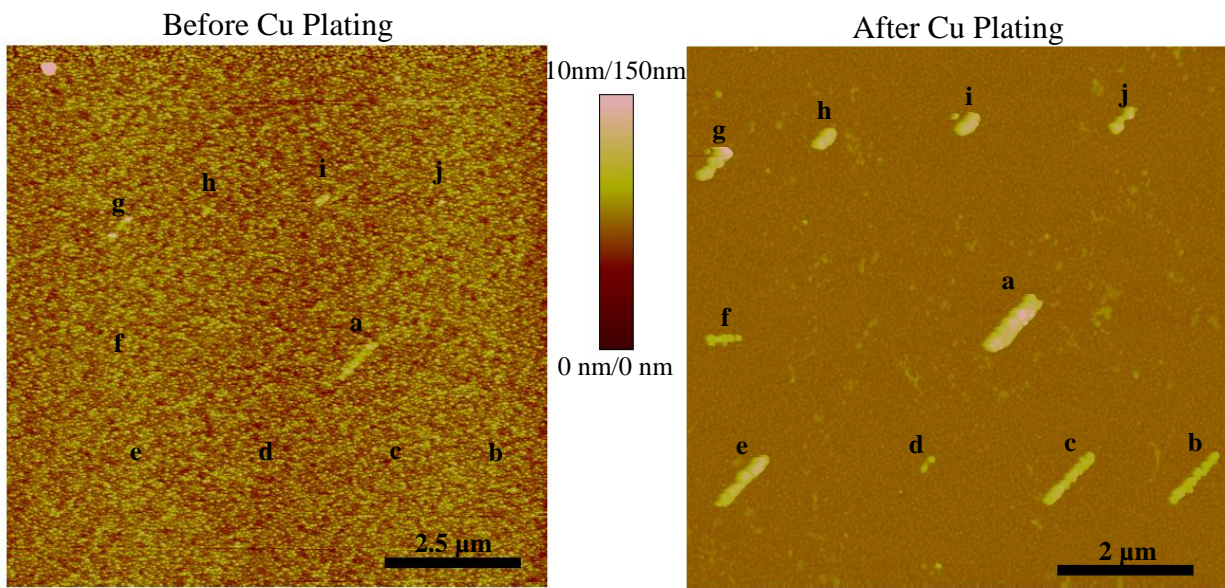


Figure 3.12 Topography images of oxidized nanofeatures before (left) and after (right) exposure to a 4 mM  $\text{Cu}^{2+}$  electroless plating solution. Each feature is labeled for reference since they do not all appear in the image before plating.

The oxidized nanopatterns were exposed to the electroless copper plating solution described earlier to form metallic copper nanofeatures. As demonstrated in 3.4.1, the copper preferentially deposits on areas of carboxyl terminated chemistry vs methyl terminated in SAMs. Here, copper deposition is examined on both systems, ODT on gold and OTS on silicon oxide, using the nanopatterns described in 3.4.3.

The ODT sample was exposed to a 4 mM  $\text{Cu}^{2+}$  electroless plating solution for 10 minutes. The entire chip was fully submerged in the solution. After being exposed to the solution, the sample was rinsed with copious amounts of water, followed by rinsing with ethanol and drying under a stream of nitrogen. The sample was then imaged in tapping mode AFM, using the same tip that was used for the oxidative lithography.

Figure 3.12 shows topography images of the oxidized nanofeatures before and after exposure to the 4 mM  $\text{Cu}^{2+}$  electroless plating solution. Copper nanofeatures have formed on each oxidized pattern, even on pattern d, which displayed little to no friction contrast. There is a

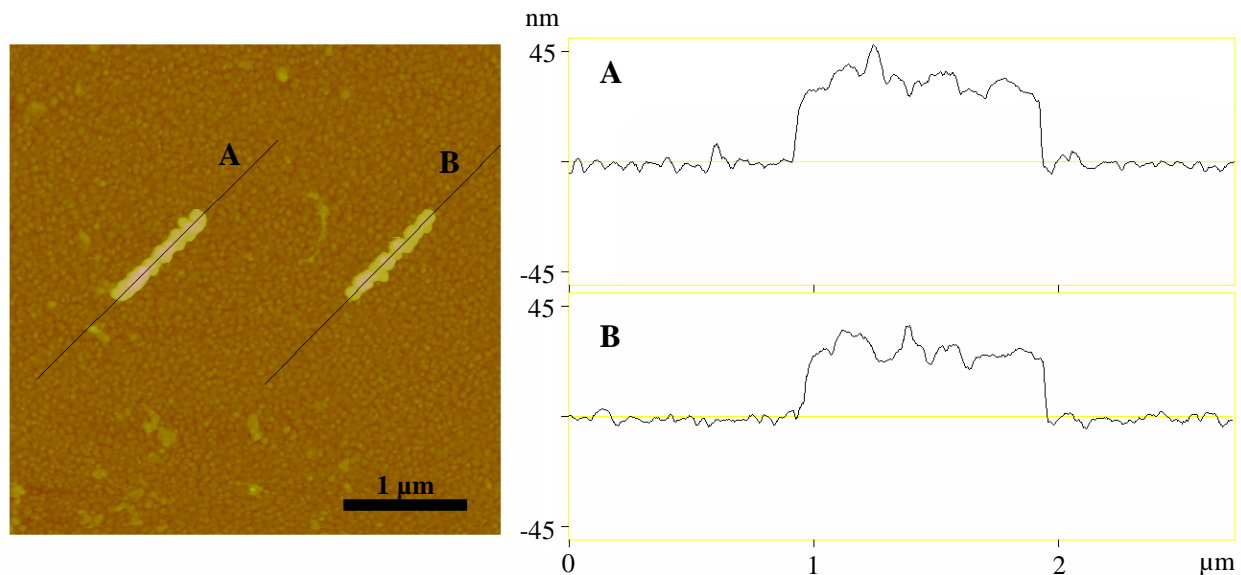


Figure 3.13 Topography (left) and height profiles (right) of copper nanofeatures. Section A profiles a copper nanofeature formed on oxidized pattern c, while section B profiles a feature formed on oxidized pattern b.

direct correlation between feature contrast in friction before plating, and feature size after plating. The stronger the feature appears in the friction image, the larger the copper feature formed after plating, and the basic shape of the feature is maintained.

For use in potential nanodevices, the feature must be continuous and, ideally, be narrow and have a low profile. Patterns b and c were characterized further as they fit this description over the other features. Figure 3.13 shows a topography image with both nanofeatures as well as height profiles for each. They are very similar in shape and size, which is to be expected as the oxidized patterns were formed under the same conditions. They are fairly rough in topography, indicating an uneven amount of copper deposition and growth along the patterns. Figure 3.14 elucidates this roughness by showing the feature grown on pattern c rendered in 3D. The nanofeature appears to be formed by a number of grains that are roughly  $100 \text{ nm}^2$  in size. This grain size is similar to the grain sizes in the gold substrate, indicating that substrate topography may have an effect on the growth of features formed on that substrate. This could be tested by

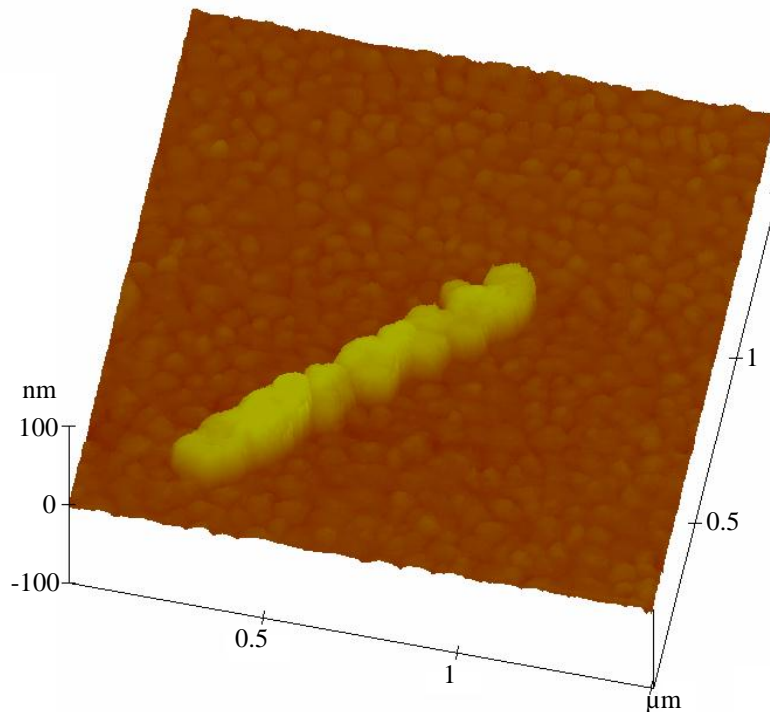


Figure 3.14 Topography of a copper nanofeature formed on oxidized pattern c, rendered in 3D to better reveal its overall topography. The grains that make up the feature are roughly on the order of  $100 \text{ nm}^2$ .

experiments exploring other types of gold surfaces. Pattern b has a measured maximum height of 35.8 nm and a maximum width of 210 nm, while pattern c has a measured maximum height of 47.4 nm and a maximum width of 248 nm. This is large compared with features formed with other methods mentioned previously, particularly in width. While the height of the feature may be controlled by the plating solution conditions, the width is controlled by both the plating solution and the size of the oxidized pattern before plating begins. A thinner oxidized pattern would result in a thinner copper feature formed on top.

#### 3.3.4.2 Electroless Copper Plating on OTS

The OTS on silicon oxide sample with oxidized patterns described in the previous section was exposed to the 4 mM  $\text{Cu}^{2+}$  solution for 20 minutes, totally submerging the sample chip. Immediately after exposure, the sample was rinsed with copious amounts of water, then ethanol

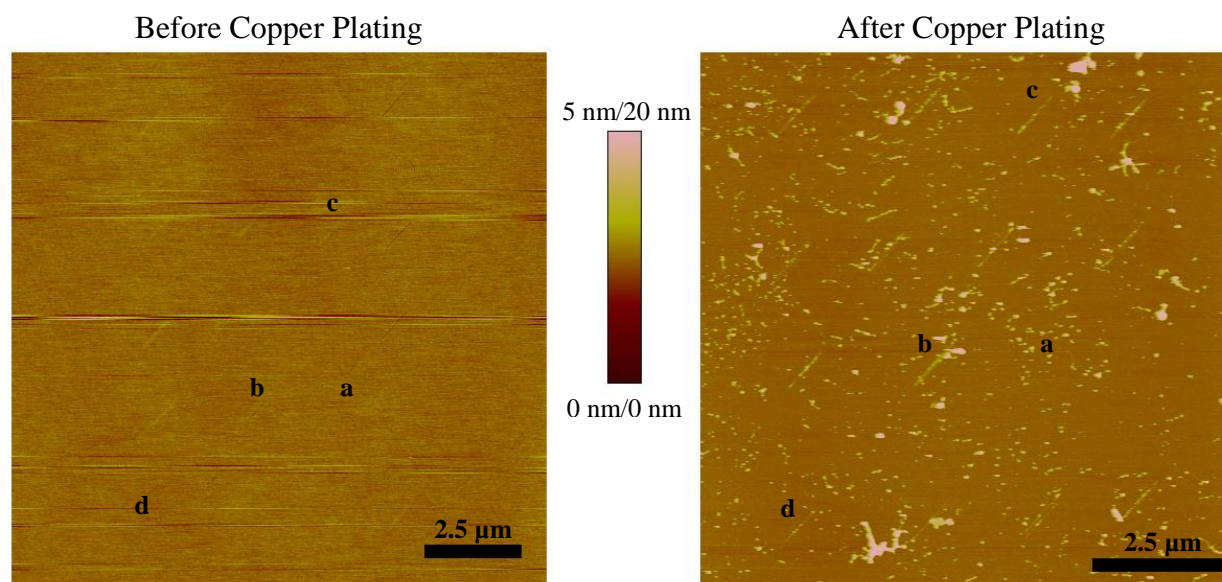


Figure 3.15 Topography images of oxidized nanopatterns before (left) and after (right) exposure to a 4 mM  $\text{Cu}^{2+}$  electroless copper plating solution for 20 minutes. Although there is some non-specific random growth, most of the patterns show an increase in topography from before plating to after. The labeled patterns correspond to the types of oxidized patterns formed. a: no oxidation occurred. b: overoxidation. c: slight oxidation. d: oxidation partially into the monolayer.

and dried under a stream of nitrogen. The sample was then imaged in tapping mode with the same tip that was previously used to form the oxidized patterns. Figure 3.15 shows topography images of the patterns before and after exposure to the plating solution. There is noticeable random deposition on the surface, however most of the oxidized patterns exhibited an increase in topography after copper plating, indicating selective growth on those patterns.

Area a shows little directed growth, which is expected since this oxidation was not detected, as described in the previous section. Pattern b, which is the overoxidized pattern, shows growth, indicating that there are some carboxyl terminated monolayer molecules present. Pattern c also shows growth. This pattern was only slightly oxidized, yet shows growth comparable to the other patterns. Pattern d, which exhibited a slight depression in topography, shows a little growth inside this depression. Patterns c and d are shown in more detail in Figure



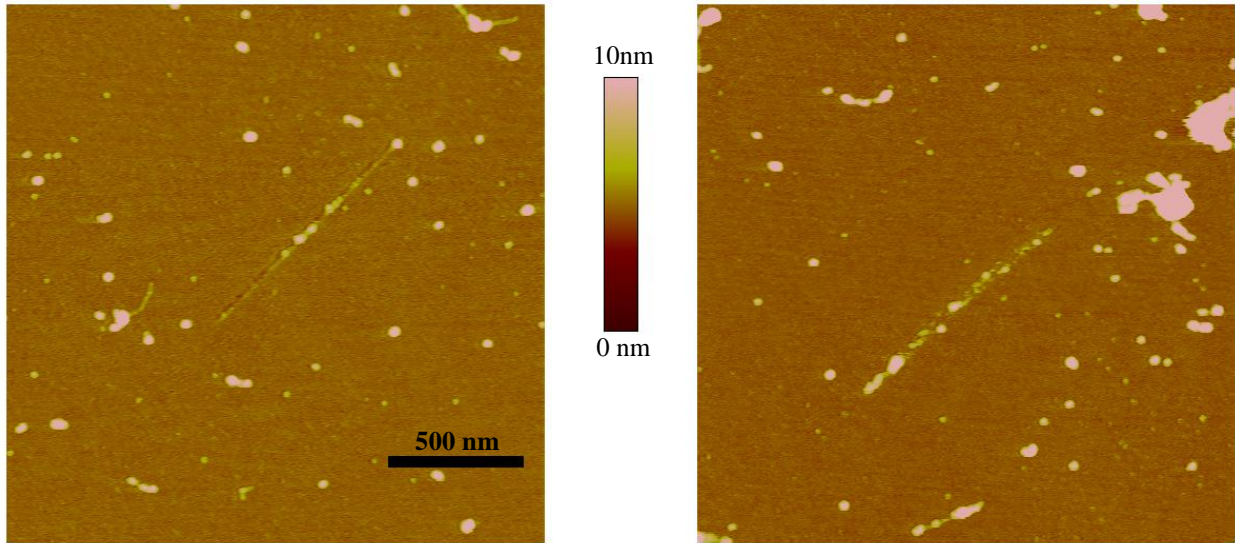


Figure 3.16 Topography images of copper deposition on oxidized patterns c (right) and d (left) in OTS on silicon oxide after 20 minutes of exposure to the 4 mM  $\text{Cu}^{2+}$  electroless plating solution. Each feature shows some nanoparticles of copper that have selectively formed on the oxidized regions.

3.16. Each pattern has some selective growth of copper nanoparticles, indicating that the copper first forms particles that grow together as the feature develops.

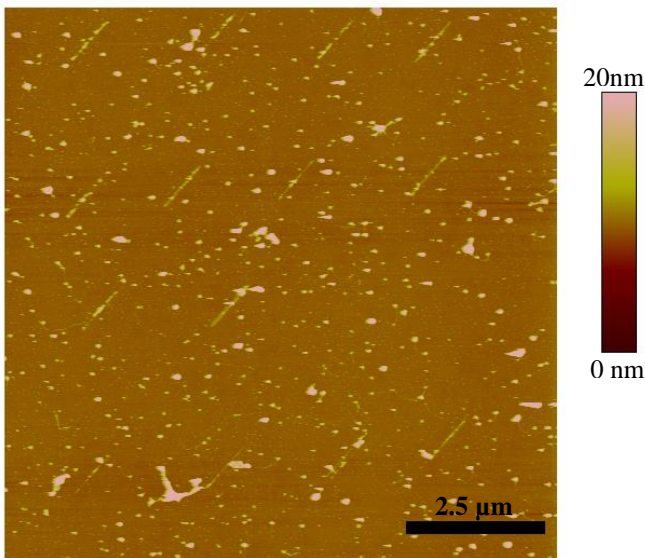


Figure 3.17 Topography of oxidized features after a total of 30 minutes exposure time to the 4 mM  $\text{Cu}^{2+}$  electroless plating solution. Many features appear slightly more pronounced than after 20 minutes exposure time.

This sample was then placed again in the 4 mM  $\text{Cu}^{2+}$  electroless plating solution for another 10 minutes. After rinsing and drying, the patterned areas were imaged again with the AFM in tapping mode. Figure 3.17 shows these features. The patterns display an increase in height after another 10 minutes in the plating solution. Patterns c and d have more copper deposited, even though pattern c still seems to be a collection of

nanoparticles. Patterns c and d were investigated more closely again, looking at the advancement of copper deposition. These images are shown in Figure 3.18. Along with topography, the profile of the deposition in each pattern is traced and shown. It is clear in the profiles how irregular the copper deposition is. Pattern d is very narrow, less than 40 nm at its widest point, but needs to be more continuous to be useful as a working nanowire. To investigate copper deposition further, this sample was again exposed to the 4 mM Cu<sup>2+</sup> electroless plating solution for another 10 minutes for a total of 40 minutes, then rinsed and dried under nitrogen.

The oxidized patterns were again imaged in tapping mode to see the extent of copper deposition. Surprisingly, the features were largely unchanged by another 10 minutes of exposure to the plating solution. To demonstrate this, Figure 3.19 shows the evolution of pattern c through the copper plating exposures. In this figure, A is a topography image of pattern c just after oxidation. It is barely visible as a slight topography increase. B is after the initial 20 minute exposure time. Copper deposition is noticeable, but seems to be in small nanoparticles spread out along the pattern. C shows topography after 30 minutes total plating time, and more copper has been deposited, although it still appears in separate nanoparticles. After 40 total minutes plating time, D shows that the overall height of the feature has not changed much, but the feature itself has changed slightly. This raises questions as to what is exactly happening in the electroless plating solution on this substrate verses the ODT on gold substrate. On that substrate, the copper features continue growing, as evidenced by the larger copper features. Here, growth seems to reach a limit, and understanding this difference will be addressed in future work.

In comparison with copper deposition on the ODT on gold system, deposition here seems to be much slower. The features on the ODT SAM were exposed to the same copper plating

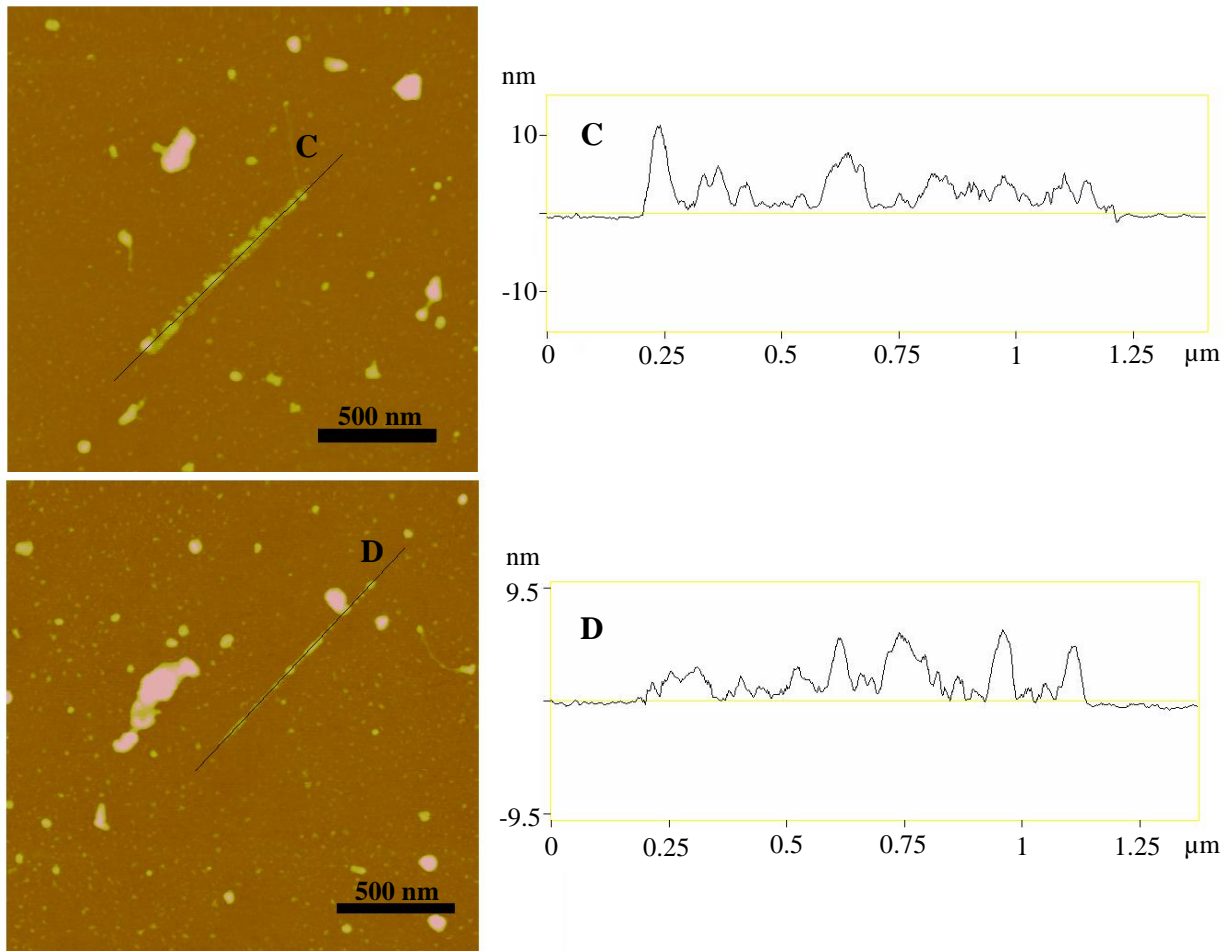


Figure 3.18 Topography (left) and height profiles (right) of copper deposition. Section C profiles copper deposition formed on oxidized pattern c, while section D profiles a deposition formed on oxidized pattern d.

conditions as the features on the OTS SAM, yet copper features 50 nm high formed on the ODT in 10 minutes compared to small nanoparticles forming on the OTS patterns in 20 minutes. The ODT and OTS monolayers both have the same terminal chemistry, methyl groups, and the oxidative lithography oxidized these into carboxyl groups. Something about the plating solution is happening differently on the ODT on gold than the OTS on silicon oxide. The biggest difference between the two systems is substrate conductivity. The plating solution works by reduction of copper ions; perhaps the conductive gold substrate helps facilitate this process. An interesting system to investigate would be a monolayer on n-doped silicon. If conductivity really

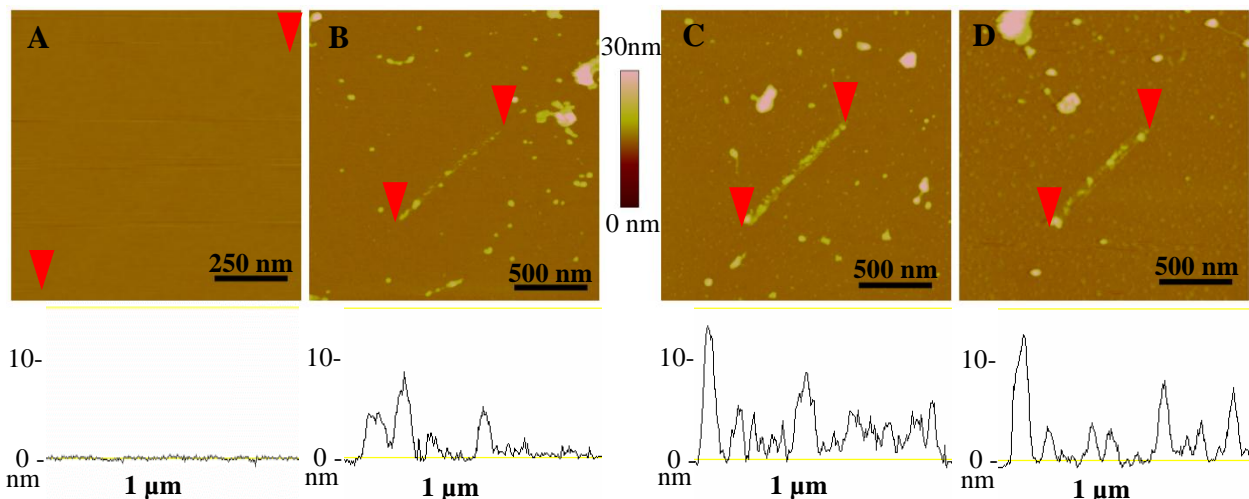


Figure 3.19 Topography and sections of oxidized pattern c in OTS monolayer through increasing amounts of exposure to the 4 mM  $\text{Cu}^{2+}$  electroless plating solution. The sections lie between the markers for each image A) no plating time, the oxidized feature is almost imperceptible. B) 20 minutes plating time. Copper nanoparticles have selectively formed on the nanopattern. C) 30 minutes plating time. More copper has deposited, but it does not fill out the pattern. D) 40 minutes plating time. The feature has not grown, though it has changed slightly.

is an important factor in both oxidation and electroless plating, a SAM directly on a conductive silicon substrate would make a good comparison.

The parameters of oxidative lithography that were studied here were tip velocity, number of scans, and tip bias. Upon exposure to the electroless plating solution, pattern d formed the most narrow nanofeature, at less than 40 nm. This nanopattern was formed with a bias of -5.57 V, a slow tip velocity of 0.2  $\mu\text{m/s}$ , and 20 passes, taking 1.7 minutes to form. In comparison, pattern c was formed for 2.5 minutes at a bias of -5.5 V a tip velocity of 5.31  $\mu\text{m/s}$  and 800 passes. The copper nanofeature formed on this pattern has a width of 90 nm. These data are summarized in Table 3.3. These features are similar in that they are non-continuous. The slower tip velocity and shorter patterning duration seems to form more narrow patterns. To fully elucidate the effects of each parameter, more studies exploring each are needed.

Table 3.3 Summary of Oxidative Lithography and Copper Plating on OTS

Pattern	Tip Bias (V)	Tip Velocity ( $\mu$ /s)	Number of Scans (approx.)	Scan Time (s)	Pattern Presence	Copper Feature Max. Width (nm)
a	-4.50	5.31	1600	300	None	-
b	-6.00	5.31	800	150	Strong	105
c	-5.50	5.31	800	150	Weak	90
d	-5.57	0.2	20	100	Present	40

### 3.5 Conclusion

The copper nanofeatures formed with the oxidative lithography and electroless copper plating described here had measured widths down to 210 nm on gold substrates, and 40 nm on silicon oxide substrates. These results compare favorably with recent publications describing the directed formation of metallic nanofeatures.<sup>25, 39, 40</sup> The Sagiv group, who really pioneered the use of oxidative lithography with SAMs for chemical nanopattern formation, have reported fabrication of silver nanofeatures. In a recent publication, they have reported silver nanofeatures with half-widths down to 33 nm.<sup>25</sup> After forming the nanopattern of carboxylic acid chemistry in an OTS resist, they apply a stamp to the surface, which consists of an OTS monolayer on a silicon oxide substrate which has been coated with a granular silver film. By applying a bias between the stamp (serving as the anode) and the patterned surface, silver nanofeatures form on the carboxyl terminated nanopatterns. The metallic nanofeatures described in this dissertation are smaller, although the nanofeatures formed with this method do seem to be more continuous. This method is also more complex, requiring the application of a silver film stamp for metal deposition instead of a solution.

A method using a conductive AFM tip to directly reduce metal ions has also recently been reported.<sup>39</sup> Here, researchers form a SAM on a negatively charged silicon surface with the SAM molecules adhered to the surface through an electrostatic interaction. They then coat the SAM with 32 nm of copper(II) acetate. Using a conductive AFM tip, they scan the surface of the copper(II) acetate while applying a -20 V bias to the substrate relative to the tip. This causes the copper ions to be locally reduced at the surface-tip interface. After nanofeature formation, the monolayer and remaining copper(II) acetate is removed by sonication in dimethylformamide, leaving the copper nanofeatures behind. The smallest copper nanofeatures reported were 35 nm in width, comparable with our results, and were also rough and non-continuous. While this method produces results similar to those presented here, it requires the use of an easily removable SAM and coating the entire surface with the metal salt. This gives the method less flexibility for use in nanodevice fabrication.

Copper feature formation on gold substrates has been recently reported as well, using a dip-pen lithography technique.<sup>40</sup> The researchers deposited nanopatterns of a carboxylic acid terminated thiol onto a bare gold substrate. They then formed a SAM of methyl terminated chemistry around the patterns. The surface was then exposed to an electroless copper plating solution and copper features formed on the nanopatterns. The widths of the copper lines formed with this method were reported to be 400 nm, and diameters of copper dots formed reported at 180 nm. This method would also be less directed with respect to features already present on the surface, requiring patterns to be formed before a monolayer is formed, and the feature sizes are larger than those shown here.

Compared to other reported methods, the one described here provides a way to form nanofeatures that is more directed, controllable, and simpler. This has implications in

nanodevice prototyping and fabrication of nanocircuitry. One example is the ATP synthase nanodevice described in Chapter 1 and others like it, where nanofeature placement and dimensions are very important. Feature continuity and consistency across substrates are the major hurdles that need to be overcome to make this a truly viable method for forming directed and controlled nanofeatures. Discussed in Chapter 5, future work will begin by first addressing these issues. Humidity control during the oxidative lithography step may help control the ultimate width of the chemical nanopattern. Temperature control during the electroless plating process has been shown to reduce non-specific copper plating,<sup>27</sup> and will be explored. Later work will include electrical characterization and optimization of copper nanofeatures formed with this method. The copper nanofeatures will be formed between microelectrodes, and I/V curves measured to assess resistance. These values can be compared to those in the literature to assess nanowire quality and performance.

## References

1. Pan, C. F.; Luo, J.; Zhu, J., *From proton conductive nanowires to nanofuel cells: A powerful candidate for generating electricity for self-powered nanosystems*. Nano Res. **2011**, 4 (11), 1099-1109.
2. Senga, R.; Hirahara, K.; Yamaguchi, Y.; Nakayama, Y., *Carbon Nanotube Torsional Actuator Based on Transition between Flattened and Tubular States*. Journal of Non-Crystalline Solids. **2012**, 358 (17), 2541-2544.
3. Bernstein, K.; Cavin, R. K.; Porod, W.; Seabaugh, A.; Welser, J., *Device and Architecture Outlook for Beyond CMOS Switches*. Proc. IEEE. **2010**, 98 (12), 2169-2184.
4. Matovic, J.; Adamovic, N.; Radovanovic, F.; Jakšić, Z.; Schmid, U., *Field effect transistor based on ions as charge carriers*. Sensors and Actuators B: Chemical. **2012**, 170 (0), 137-142.
5. Haspert, L. C.; Lee, S. B.; Rubloff, G. W., *Nanoengineering Strategies for Metal–Insulator–Metal Electrostatic Nanocapacitors*. ACS Nano. **2012**, 6 (4), 3528-3536.
6. Kumar, R.; Singh, N.; Chang, C. K.; Dong, L.; Wong, T. K. S., *Deep-ultraviolet resist contamination for copper/low-k dual-damascene patterning*. J. Vac. Sci. Technol. B. **2004**, 22 (3), 1052-1059.
7. Seisyan, R. P., *Nanolithography in microelectronics: A review*. Tech. Phys. **2011**, 56 (8), 1061-1073.
8. Radha, B.; Kulkarni, G. U., *An Electrical Rectifier Based on Au Nanoparticle Array Fabricated Using Direct-Write Electron Beam Lithography*. Adv. Funct. Mater. **2012**, 22 (13), 2837-2845.
9. O'Connell, C. D.; Higgins, M. J.; Nakashima, H.; Moulton, S. E.; Wallace, G. G., *Vapor Phase Polymerization of EDOT from Submicrometer Scale Oxidant Patterned by Dip-Pen Nanolithography*. Langmuir. **2012**, 28 (26), 9953-9960.
10. Liu, M.; Amro, N. A.; Liu, G. Y., *Nanografting for surface physical chemistry*. In *Annual Review of Physical Chemistry*, Annual Reviews: Palo Alto, 2008; Vol. 59, pp 367-386.
11. Maoz, R.; Frydman, E.; Cohen, S. R.; Sagiv, J., *"Constructive nanolithography": Inert monolayers as patternable templates for in-situ nanofabrication of metal-semiconductor-organic surface structures - A generic approach*. Adv. Mater. **2000**, 12 (10), 725-+.
12. Intel 22nm 3-D Tri-Gate Transistor Technology. <http://newsroom.intel.com/docs/DOC-2032> (accessed Oct. 28).
13. Gates, B. D.; Xu, Q.; Stewart, M.; Ryan, D.; Willson, C. G.; Whitesides, G. M., *New Approaches to Nanofabrication: Molding, Printing, and Other Techniques*. Chemical Reviews. **2005**, 105 (4), 1171-1196.
14. Gonsalves, K. E.; Merhari, L.; Wu, H.; Hu, Y., *Organic–Inorganic Nanocomposites: Unique Resists for Nanolithography*. Adv. Mater. **2001**, 13 (10), 703-714.
15. Basnar, B. W., Itamer, *Dip-Pen-Nanolithographic Patterning of Metallic, Semiconductor, and Metal Oxide Nanostructures on Surfaces*. Small. **2009**, 5 (1), 28-44.
16. Nam, J.-M.; Han, S. W.; Lee, K.-B.; Liu, X.; Ratner, M. A.; Mirkin, C. A., *Bioactive Protein Nanoarrays on Nickel Oxide Surfaces Formed by Dip-Pen Nanolithography*. Angewandte Chemie International Edition. **2004**, 43 (10), 1246-1249.
17. Noy, A.; Miller, A. E.; Klare, J. E.; Weeks, B. L.; Woods, B. W.; DeYoreo, J. J., *Fabrication of luminescent nanostructures and polymer nanowires using dip-pen nanolithography*. Nano Lett. **2002**, 2 (2), 109-112.



18. Lee, K. B.; Park, S. J.; Mirkin, C. A.; Smith, J. C.; Mrksich, M., *Protein nanoarrays generated by dip-pen nanolithography*. *Science*. **2002**, 295 (5560), 1702-1705.
19. Breitenstein, M.; Nielsen, P. E.; Holzel, R.; Bier, F. F., *DNA-nanostructure-assembly by sequential spotting*. *J. Nanobiotechnol.* **2011**, 9.
20. Felts, J. R.; Suhas, S.; Randy, H. E.; William, P. K., *Nanometer-scale flow of molten polyethylene from a heated atomic force microscope tip*. *Nanotechnology*. **2012**, 23 (21), 215301.
21. Xu, S.; Liu, G. Y., *Nanometer-scale fabrication by simultaneous nanoshaving and molecular self-assembly*. *Langmuir*. **1997**, 13 (2), 127-129.
22. Cruchon-Dupeyrat, S.; Porthun, S.; Liu, G. Y., *Nanofabrication using computer-assisted design and automated vector-scanning probe lithography*. *Applied Surface Science*. **2001**, 175–176 (0), 636-642.
23. Xie, X. N.; Chung, H. J.; Sow, C. H.; Wee, A. T. S., *Nanoscale materials patterning and engineering by atomic force microscopy nanolithography*. *Materials Science and Engineering: R: Reports*. **2006**, 54 (1–2), 1-48.
24. Dagata, J. A.; Perez-Murano, F.; Abadal, G.; Morimoto, K.; Inoue, T.; Itoh, J.; Yokoyama, H., *Predictive model for scanned probe oxidation kinetics*. *Appl. Phys. Lett.* **2000**, 76 (19), 2710-2712.
25. Berson, J.; Zeira, A.; Maoz, R.; Sagiv, J., *Parallel- and serial-contact electrochemical metallization of monolayer nanopatterns: A versatile synthetic tool en route to bottom-up assembly of electric nanocircuits*. *Beilstein J. Nanotechnol.* **2012**, 3, 134-143.
26. Garno, J. C.; Zangmeister, C. D.; Batteas, J. D., *Directed electroless growth of metal nanostructures on patterned self-assembled monolayers*. *Langmuir*. **2007**, 23 (14), 7874-7879.
27. Lu, P.; Walker, A. V., *Investigation of the mechanism of electroless deposition of copper on functionalized alkanethiolate self-assembled monolayers adsorbed on gold*. *Langmuir*. **2007**, 23 (25), 12577-12582.
28. Bid, A.; Bora, A.; Raychaudhuri, A. K., *Temperature dependence of the resistance of metallic nanowires of diameter  $\geq 15$  nm: Applicability of Bloch-Gruneisen theorem*. *Physical Review B*. **2006**, 74 (3).
29. Wang, H.; Chen, S. F.; Li, L. Y.; Jiang, S. Y., *Improved method for the preparation of carboxylic acid and amine terminated self-assembled monolayers of alkanethiolates*. *Langmuir*. **2005**, 21 (7), 2633-2636.
30. Porter, M. D.; Bright, T. B.; Allara, D. L.; Chidsey, C. E. D., *SPONTANEOUSLY ORGANIZED MOLECULAR ASSEMBLIES .4. STRUCTURAL CHARACTERIZATION OF NORMAL-ALKYL THIOL MONOLAYERS ON GOLD BY OPTICAL ELLIPSOMETRY, INFRARED-SPECTROSCOPY, AND ELECTROCHEMISTRY*. *J. Am. Chem. Soc.* **1987**, 109 (12), 3559-3568.
31. Michael, K. E.; Vernekar, V. N.; Keselowsky, B. G.; Meredith, J. C.; Latour, R. A.; Garcia, A. J., *Adsorption-induced conformational changes in fibronectin due to interactions with well-defined surface chemistries*. *Langmuir*. **2003**, 19 (19), 8033-8040.
32. Atmaja, B.; Cha, J. N.; Frank, C. W., *Adsorbed alpha-Helical Diblock Copolypeptides: Molecular Organization, Structural Properties, and Interactions*. *Langmuir*. **2009**, 25 (2), 865-872.

33. Bethencourt, M. I.; Srisombat, L. O.; Chinwangso, P.; Lee, T. R., *SAMs on Gold Derived from the Direct Adsorption of Alkanethioacetates Are Inferior to Those Derived from the Direct Adsorption of Alkanethiols*. Langmuir. **2009**, *25* (3), 1265-1271.
34. Jiang, P.; Li, S. Y.; Sugimura, H.; Takai, O., *Pattern design in large area using octadecyltrichlorosilane self-assembled monolayers as resist material*. Applied Surface Science. **2006**, *252* (12), 4230-4235.
35. Liu, G. Y.; Xu, S.; Qian, Y. L., *Nanofabrication of self-assembled monolayers using scanning probe lithography*. Accounts Chem. Res. **2000**, *33* (7), 457-466.
36. Malcomson, M. F., Quintus, *Mechanism of Copper Deposition in Electroless Plating*. Langmuir. **1990**, *6*, 1709-1710.
37. Wasserman, S. R.; Tao, Y. T.; Whitesides, G. M., *STRUCTURE AND REACTIVITY OF ALKYL-SILOXANE MONOLAYERS FORMED BY REACTION OF ALKYLTRICHLOROSILANES ON SILICON SUBSTRATES*. Langmuir. **1989**, *5* (4), 1074-1087.
38. Kuramochi, H.; Tokizaki, T.; Onuki, T.; Yokoyama, H., *Precise Control of Nanofabrication by Atomic Force Microscopy*. J. Nanosci. Nanotechnol. **2010**, *10* (7), 4434-4439.
39. Kwon, G.; Chu, H.; Yoo, J.; Kim, H.; Han, C.; Chung, C.; Lee, J.; Lee, H., *Fabrication of uniform and high resolution copper nanowire using intermediate self-assembled monolayers through direct AFM lithography*. Nanotechnology. **2012**, *23* (18).
40. Chang, Y. H.; Wang, C. H., *Electroless deposition of Cu nanostructures on molecular patterns prepared by dip-pen nanolithography*. J. Mater. Chem. **2012**, *22* (8), 3377-3382.

## Chapter 4: Surface Potential Mapping of Azulene Derivative and Gold Nanoparticles Adsorbed onto Graphite

### 4.1 Introduction

Graphene-like materials are attracting much interest for use in nanoscale and nanostructured devices, such as solar cells, fuel cells, field-effect transistors (FETs), and more. This is due to graphene's unique electronic properties. Pristine graphene is a zero-band gap semiconductor, allowing it to be n-doped for conductivity, or p-doped to introduce a band gap.<sup>1</sup> This tunability gives graphene much potential for use in various devices as either a conductor, such as an electrode, or a semiconductor, such as the channel in a FET. Adsorbates have been shown to dope graphene, and good control of this doping behavior will lead to better control and implementation of graphene in these devices. Here we show the initial results investigating a novel system, azulene compounds adsorbed onto graphite, and also gold nanoparticles of varying shapes adsorbed onto graphite. Azulene, a bicyclic aromatic molecule composed of fused 5 and 7 member rings, is itself tunable by changing substituents on the rings. Substitution with different functional groups at different ring positions shifts the energy of the HOMO or the LUMO, causing azulene compounds to display a variety of colors.<sup>2</sup> This, combined with the ability for azulene compounds to  $\pi$ - $\pi$  stack with graphene, make them a strong candidate for use as adsorbates on graphene for tuning its electronic properties. We found that azulene compounds behaved differently on graphite depending on whether their substituents were electron donating or electron withdrawing. The compounds with electron withdrawing groups appeared to p-dope the graphite, while those with electron donating groups appeared to n-dope it. The behavior of the gold nanoparticles, however, did not change depending on shape and was n-doping in

character. This affirms the idea that azulene compounds can be used as effective tuners for graphene-like materials.

#### 4.1.1 Graphene-Like Materials Properties

A chapter of work on graphene-like materials cannot begin without addressing the remarkable properties of these materials. Graphene itself is a two dimensional material composed of  $sp^2$  hybridized carbons bonded in a hexagonal pattern, with each carbon bonding with 3 neighbors, shown in Figure 4.1. This leaves an electron in the remaining p orbital, which forms  $\pi$ -bonds with neighboring p orbitals. A network of  $\pi$ -bonds is formed across the whole of the carbon sheet, delocalizing the

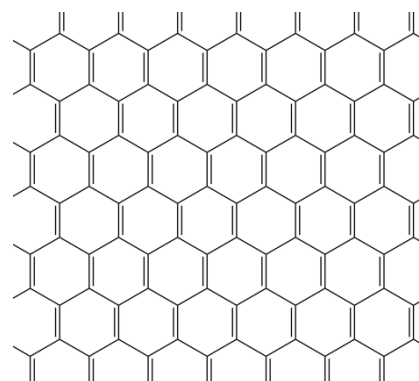


Figure 4.1 Simple drawing of the molecular structure of graphene.

electrons in the  $\pi$  system. These delocalized electrons, in conjunction with graphene's symmetry, are what make graphene's electronic properties unique.<sup>1</sup> Graphene is also exceptionally tough and bendable;<sup>3</sup> combined with its conductivity these properties make it an attractive subject for novel electronic devices research. One such use is as the transparent electrode in a flexible solar cell,<sup>4</sup> since a single sheet of graphene is both conductive and transparent. Other devices include using graphene as the channel in field effect transistors (FETs),<sup>5</sup> decorated graphene as the catalysis material in fuel cells,<sup>6</sup> and more. Graphene can also be thought of as the basis for other graphene-like materials, such as carbon nanotubes (CNT) and graphite.

CNTs, and in particular, single-walled carbon nanotubes (SWCT), are a graphene-like material that can be thought of as “rolled up” or tubular graphene. Consisting of the same

chemistry as graphene,  $sp^2$  hybridized carbons bonded to 3 neighbors, their properties are mostly determined by their chirality and diameter.<sup>7</sup> Chirality for SWCNTs is determined by the angles at which they are “rolled up.” SWCNT can be either metallic conductors or semiconductors based on this chirality. As with graphene, SWCNTs are tough and flexible and are also subjects of much research, sharing many applications with graphene, including the channel in FETs<sup>8</sup>, hole and electron transporters in solar cells,<sup>9</sup> and as sensors for small molecules.<sup>10</sup>

Graphite is composed simply of many stacks of graphene. This is what gives graphite its lubricating properties, since there are no chemical bonds between sheets, as well as its conductance. Graphite is also relatively inexpensive and easy to work with, making it an excellent material for preliminary investigation into graphene-like materials, such as the presented work.

Here we have adsorbed different azulene derivatives and gold nanoparticles onto graphite in order to study the electronic interaction between the adsorbate and the graphite. This interaction is important for understanding how graphite-like materials will behave in devices. The surface potential mapping method with AFM is used to create electrostatic potential maps of the adsorbates on the surface of the graphite. It is found that by changing the substituents on a single position on the azulene ring, the surface potential is altered, indicating a change in the doping of the graphite, which will affect its electronic properties. This change provides a path to tunability of the graphene-like materials’ electronic properties, which should allow these materials to be optimally incorporated into a variety of devices.

#### 4.1.2 Graphene-Like Materials in Devices

As mentioned above, graphene-like materials have garnered quite a bit of attention in research particularly for use in devices where nanostructure is critical to the function and performance of the device. FETs constructed with graphene<sup>11, 12</sup> or CNTs<sup>13</sup> are being studied as alternatives to traditional semiconductor based transistors. As mentioned previously, photolithography methods are currently used to construct nano-scale transistors for circuits, but they will eventually reach a fundamental limit. Ultra-narrow graphene ribbons and CNTs may have the potential to get past this limit and into even smaller devices that use less power. Nanostructured decorated graphene catalysts are also being researched for use in fuel cells.<sup>14</sup> These nanostructured decorated graphene catalysts have a high surface area, and are being developed to replace expensive platinum. Capacitors constructed with graphene sheets show promise for storing electricity and being able to charge and discharge very quickly.<sup>15</sup> Both graphene and CNTs have also been the focus of much research in the area of solar cells, including dye-sensitized solar cells (DSSCs).<sup>16, 17</sup> Graphene has been proposed as a good candidate for the transparent electrode<sup>18</sup> because a single sheet has good transparency, sheet resistance,<sup>19</sup> and flexibility, potentially replacing the relatively expensive and brittle indium based transparent electrodes commonly used.<sup>19</sup> CNTs have been under much investigation as materials to channel the electrons from the dyes to the transparent electrode in DSSCs.<sup>20</sup> They have also been used in gas sensors<sup>21</sup>, FETs<sup>22</sup>, and more. All of these devices are dependent on the electronic properties of the graphene-like material they utilize. Most important for electronic devices, the electronic properties of graphene-like materials can be altered simply by being in contact with another material, be it adsorbates<sup>23</sup> or even the substrate it is placed upon.<sup>24</sup> In a recent study, researchers have reported the doping of graphene due to various substrates using

Raman spectroscopy and surface potential mapping.<sup>25</sup> They found that a silicon oxide substrate p-dopes graphene, while a SAM with an amine terminal group n-dopes it.

#### 4.1.3 Tunability of Graphene-Like Materials' Electronic Properties

Previous studies have indicated that the local environment can have an impact on the electronic properties of graphene<sup>26</sup> and CNT.<sup>27</sup> These effects occur because of the unique electronic structure of graphene itself. This structure comes from the symmetry and hexagonal lattice of the graphene. The primitive unit cell of graphene is a diamond shape that contains two atoms. In order to visualize the unique electronic structure of graphene, a conversion must be

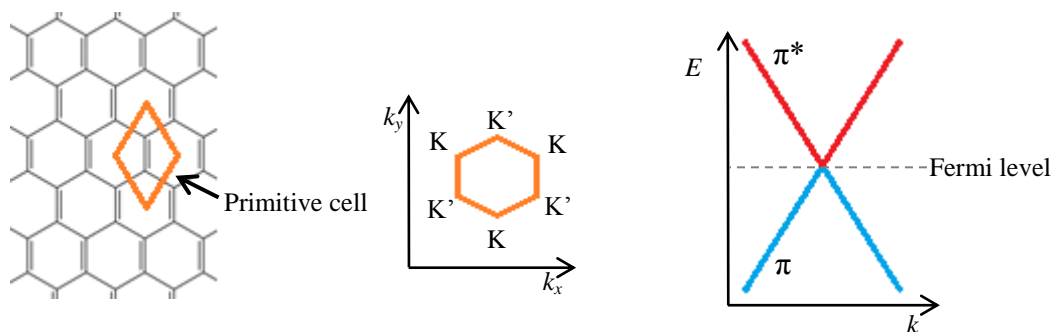


Figure 4.2 Primitive cell (left), Brillouin zone (middle), and  $\pi$  and  $\pi^*$  energy levels in momentum space around the K point (right). The  $\pi$  orbital (blue) acts as a valence band, and the  $\pi^*$  orbital (red) the conductance band. In pristine graphene there is a zero energy gap between these bands. Upon doping, the graphene can behave like a metallic conductor (n-doping) or a semiconductor with an engineered band gap (p-doping).

made from real space to momentum space. In momentum space, the primitive unit cell is the Brillouin zone. In graphene, this unit cell is hexagonal. The corners of the Brillouin zone are called the K and K' points and if the energy of the delocalized  $\pi$  and  $\pi^*$  orbitals are plotted near these K points, what we see is that for pristine graphene, the two orbitals just meet in an inverse cone fashion,<sup>28</sup> shown in Figure 4.2. This means there is a zero energy gap between the orbitals at these points. The  $\pi$  and  $\pi^*$  orbitals act as the valence and conductance bands, respectively, of

the material, and since this valence band is full in pristine graphene and its conduction band so close in energy, it is very sensitive to its environment, as any local changes will disrupt the electronic structure. Adsorbates and substrate effects can pull electrons out of the valence band or push electrons into the conduction band, introducing a band gap and causing the graphene to behave more like a semiconductor in the first case, and causing metallic behavior in the second.<sup>29</sup> This tunability is one of the properties that many researchers are interested in for graphene use in electronic devices, but it happens whenever the graphene is in contact with another material. In a device, for instance, the graphene is often supported on a substrate, and this substrate will have a strong effect on the graphene's electronic properties. Researchers have shown, for instance, that graphene on silicon oxide becomes n-doped,<sup>25</sup> while graphene on a highly fluorinated SAM becomes p-doped.<sup>25</sup> The environment the graphene is in will always have an effect on it, and that effect must be accounted for in design. CNTs have a similar electronic structure to graphene. As mentioned previously, their metallic or semiconducting nature depends on their chirality and thus symmetry. Adsorbates on CNTs can also play a role in their function and properties.<sup>30</sup> In graphite the valence and conduction bands in the graphene sheets overlap, and so it conducts metallically. The interaction of adsorbates on the surface of graphite can give insight into how those adsorbates would affect other graphene-like materials. This work is partly motivated by the question of how adsorbates interact with and affect graphene-like materials and how can we use these interactions to our advantage in devices.

#### 4.1.4 Azulene Compounds and Gold Nanoparticles as Adsorbates

In order to address the tunable electronic nature of graphene-like materials for use in devices, a suitable set of doping adsorbates must be established. This set should have well defined changes in structure and electronic properties in order to make good comparisons. The



molecules chosen for this work are azulene compounds, as they share a core structure that will adsorb well to graphite and have electronic properties that are tunable through substitution on the ring structure. Gold nanoparticles were also studied, as metal nanoparticles are often used to decorate graphene-like materials in devices to improve performance.<sup>31</sup> The main motivation for this work comes from an interest in the optical and electronic properties of azulene molecules and gold nanoparticles and their interaction with graphene-like material as potential dopants.<sup>32</sup> Azulenes are aromatic organic compounds composed of fused seven and five membered rings. Azulene is depicted in Figure 4.3. This ring structure causes a permanent dipole in the molecules, and the HOMO-LUMO gaps of the various azulenes span the visible spectrum. This gap falls in the visible range because of the electronic structure of their HOMOs and LUMOs.<sup>2</sup> The HOMO of an azulene molecule has a lot of electron density on the odd numbered carbons, and very little on the even. Conversely, the LUMO has the opposite; for electrons promoted to this energy level, density is concentrated on the even numbered carbons. Not only does this lower the energy gap between the levels, it allows the HOMO and LUMO to be separately tuned by adding functional groups on different atoms of the molecule. Adding electron donating groups to even carbons destabilizes the LUMO, increasing its energy and widening the HOMO-LUMO gap. An electron withdrawing group on those even carbons would work to stabilize the ring, causing the LUMO to drop in energy, thus lowering the gap. Groups on odd carbons would work this way on the HOMO, electron withdrawing groups stabilizing it and electron donating groups destabilizing it.<sup>2</sup>

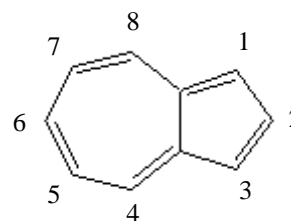


Figure 4.3 The azulene molecule with carbon numbering scheme.

This tunability in the azulene HOMO-LUMO gap makes azulenes attractive molecules to use as dopants, if we can tune their interaction with the graphene-like material. If these orbitals of the azulenes are near in energy to the Fermi level of the graphite-like material, they can interact. If the graphene-like material interacts with the HOMO of an azulene, that HOMO is full of electrons, and will share that electron density with the graphene-like materials, n-doping it.<sup>33</sup> If the LUMO is interacting with it, electron density will be drawn out of the graphene-like material, p-doping it. It could be possible to tune that interaction, simply by using different azulenes with different substituents. Interactions like these have been studied before. Experiments detailed by Wang et al. study how two different molecules, one with very electron withdrawing fluorine groups, and one with a vanadium center, interact with exfoliated graphene.<sup>34</sup> Here they found, with both nanoscale surface potential mapping and more bulk-scale FET experiments, that the molecule with electron withdrawing groups pulled electron density out of the graphene, p-doping it, while the molecule with the vanadium center donated electron density, n-doping it. Other studies have shown how the molecule tetrafluoro-tetracyanoquinodimethane (F4-TCNQ) interacts with epitaxial graphene grown on silicon carbide substrates on a macro-scale.<sup>35, 36</sup> In this system, the substrate donates electron density to the graphene. It was shown that the F4-TCNQ molecules layered on top of the graphene will pull electron density from the graphene. With enough molecules, the graphene was shown to reach a neutral state as the doping from the substrate and the molecules balanced out.

Another thing that makes them attractive is the planar  $\pi$  system in azulene for  $\pi$ - $\pi$  stacking interactions with the graphene-like materials. Chemisorption to graphene and carbon nanotubes interrupts the conjugated  $\pi$  system, and thus interferes with the core electronic properties of the graphene-like material. The  $\pi$  system of the azulenes, however, can  $\pi$ - $\pi$  stack

with the  $\pi$  system of the graphene-like material. This interaction is much more subtle, leading to the doping effect, without completely disrupting the conjugated  $\pi$  system of the graphene. This makes physisorption a feasible way to attach these molecules to the graphite-like material.

In addition to azulenes, gold nanoparticles of different shapes and sizes also hold promise as dopants for graphene-like materials<sup>32</sup> and other materials such as photonics<sup>37</sup> and plasmonics.<sup>38, 39</sup> As gold particles get very small, their properties

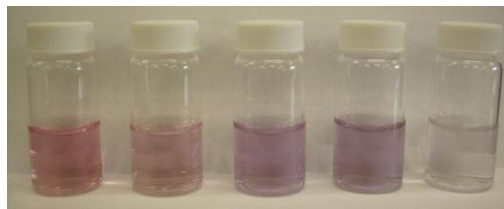


Figure 4.4 Solutions of varying sizes of gold nanoparticles.

change. Surface plasmon effects take over, and the particles start absorbing and scattering visible light, shown in Figure 4.4. The wavelength of light absorbed depends mostly on the size of the nanoparticles. These particles, like azulenes, could be used as sensitizers adsorbed onto semiconducting CNTs or graphene nanoribbons in DSSC, to tune the properties of graphene-like materials by doping, or to scatter the light into the cell, increasing performance.

There have been and are many studies being done on graphene-like materials and their interaction with other molecules.<sup>40</sup> A lot of work has been done in graphene FETs looking at how adsorbates effect their performance.<sup>41, 42</sup> In one study, researchers adsorbed triazine to bilayer and monolayer graphene FETs.<sup>41</sup> They loaded the graphene with different amounts of the molecules, and determined that the electronic properties of the graphene FETs changed with different amounts of triazine adsorbed. In another study, graphene FETs were exposed to air, to adsorb oxygen and water molecules, and aluminum for doping.<sup>42</sup> Here they found that exposure to air p-dopes the graphene, while adsorbed aluminum strongly n-dopes the graphene. This is one way to look at the interaction, but it's very much a bulk measurement. They are measuring what happens to the system on a macroscopic scale. What we want to know is what is going on

at the nanoscale. Devices that use graphene and CNTs are inherently nanoscale, due to their dimensionality; what happens at this scale is important, as feature morphology and surface coverage may have an effect on interactions. One method to probe what is happening, both physically and electrically, is surface potential mapping. Using a conductive AFM probe, both the topography and the electrostatic potential at the surface can be mapped at nanometer length scales. This can provide information relating nanoscale physical features, like adsorbates, with their electrostatic potential relative to the substrate. This tells us about the local distribution of charge on the surface, which in turn, tells us about the electronic interaction happening at that surface. This kind of work has been previously reported describing the doping of graphene sheets with molecules. They found the molecules could either donate electron density to the graphene or pull it into themselves, thus doping the graphene. This was found with a combination of Raman spectroscopy and surface potential mapping experiments.<sup>34</sup>

This chapter details research exploring the novel system of a few azulene derivatives interacting with graphite as well as gold nanoparticles of different shapes and sizes on graphite using nanoscale surface potential mapping performed with an AFM. As mentioned previously, surface potential mapping, also known as Kelvin probe force microscopy, allows us to probe the electrostatic interaction of the adsorbate and the substrate at the nanoscale. This can help us determine if electrons are moving from the adsorbate to the graphite, or vice versa. If there are differences in the interaction between graphite and differently substituted azulenes, this would show up in the surface potential mapping, and would be evidence that these molecules could be used as tunable dopants for graphene-like materials.

## **4.2 Methods and Materials**

#### 4.2.1 Azulene Compounds, Naphthalene, and Toluene

Four differently functionalized azulenes were obtained from the Barybin group. These were azulene, 1,3-diiodoazulene (DIA), 1,3-di(2,2,2-trifluoro-1-oxoethyl)azulene (DTFA), and 1-(2,2,2-trifluoro-1-oxoethyl)azulene (TFA). Each azulene has a different amount of electron donation or withdrawal on the same carbons, 1, 3 or both. Thus

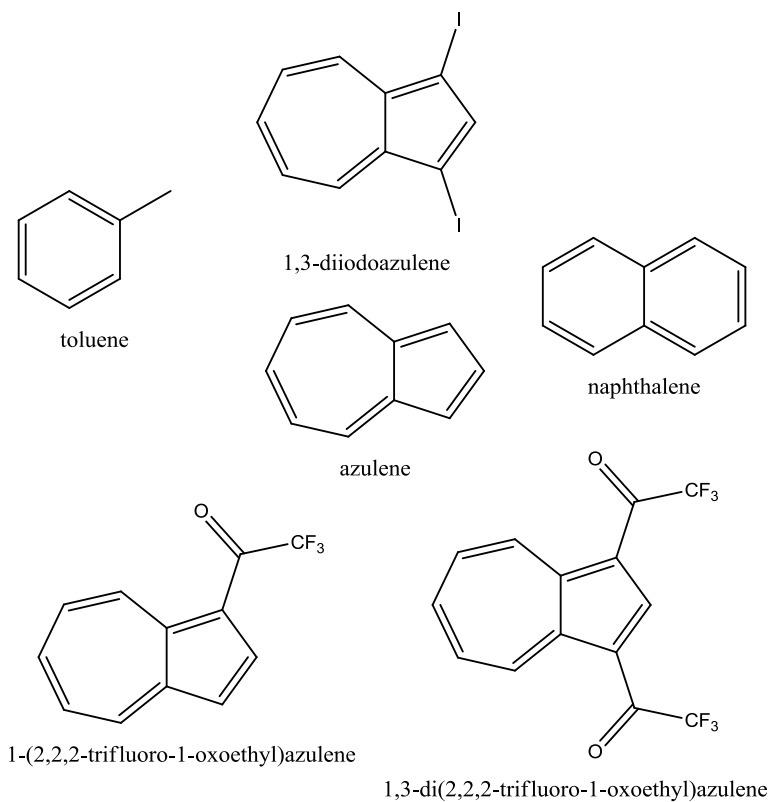


Figure 4.5 Molecular adsorbates investigated.

each azulene will have differently tuned HOMO energy levels and may interact differently with the graphite surface. The iodo groups are electron donating, and so destabilize the ring structure, causing an increase in HOMO energy. The trifluoro-1-oxoethyl groups are electron withdrawing, and work to stabilize the HOMO, bringing its energy down. Naphthalene was also studied as a comparison to azulene. It is the same size as the azulene, but its ring structure is more similar to that of the graphite surface. Toluene was studied as well, as a six membered ring system. Figure 4.5 shows all these molecules.

#### 4.2.2 Gold Nanoparticles

The gold nanoparticle work described here was performed with a talented REU, Zachary Bushman. Four shapes and sizes of gold nanoparticles were studied. These were 40 nm and 15 nm diameter spheres,<sup>43</sup> about 300 nm diameter octahedrons,<sup>44</sup> and about 40 nm diameter stars.<sup>45</sup> Each of the particles was synthesized using established protocols. For the 40 nm and 15 nm diameter spheres, a 0.01 wt% aqueous gold(III) chloride was used with varying amounts of a 1 wt% aqueous sodium citrate solution added. To form the 15 nm diameter particles, 50 mL of the AuCl<sub>3</sub> solution was brought to a boil and then 1.5 mL of the sodium citrate solution was added. Boiling and stirring was continued for ten minutes, then stirring without heat for another 15 minutes. The same procedure was used for the 40 nm spheres, except that 0.625 mL of the sodium citrate solution was added, instead of 1.5 mL.<sup>43</sup>

The gold nanostars were formed by making a solution of 60 mM cetyltrimethylammonium bromide, 0.4 mM gold(III) chloride, and 0.64 mM ascorbic

acid. The solution was left at room temperature for 20 hours, and had developed a purple color. The solution was then centrifuged until the nanoparticles settled out. They were then resuspended in clean water.<sup>45</sup>

The gold octahedrons were formed by adding 0.4 mL of a 20 wt% polydiallyldimethylammonium chloride solution and 16  $\mu$ L of a 1 M HCl solution to 20 mL

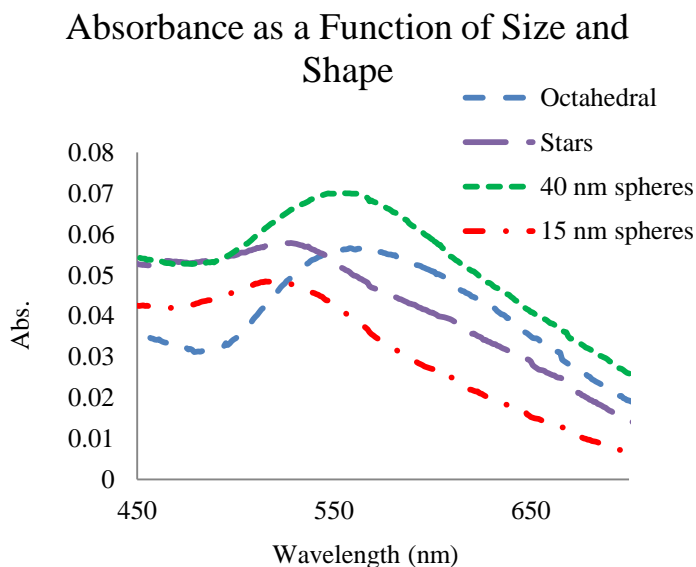


Figure 4.6 UV-Vis spectra showing the plasmon absorption bands of the gold nanoparticles synthesized and used as adsorbates.

ethylene glycol. This solution was then stirred for two minutes. 6.5  $\mu\text{L}$  of gold(III) chloride was added, then the mixture was refluxed while stirring for one hour. The solution's color changed from clear to pink to a rusty color. After cooling, the solution was centrifuged to pull the nanoparticles out. The particles were then resuspended in clean water.<sup>44</sup> Each solution of nanoparticles was analyzed with a Cary 100 UV-Vis spectrometer and the spectra compared with literature values for confirmation. These spectra are shown in Figure 4.6, and are the plasmon absorption bands for each nanoparticle solution. These match the spectra reported for each synthesis method.

#### 4.2.3 Highly Ordered Pyrolytic Graphite

The graphite substrate was typical highly ordered pyrolytic graphite (HOPG). To renew the surface, a piece of Scotch tape was used to exfoliate the surface layers of graphite, exposing fresh layers, and any loose fragments were peeled off with tweezers. The graphite was contacted to ground for a few seconds before being mounted onto the AFM, but was insulated during measurements.

#### 4.2.4 Azulenes and Naphthalene Adsorption onto Graphite

The samples were prepared by first dissolving the molecules in solvent. Solutions of 0.6 mM were made for each azulene and naphthalene in methylene chloride and also in benzene for the azulenes. A 2  $\mu\text{L}$  aliquot of the solution was placed on the graphite surface with a micropipette and then allowed to evaporate. The sample surface was then placed under a stream of nitrogen for two minutes. After this, the sample was mounted onto the AFM. Because of the low concentration and evaporation method, a gradient of surface coverage of molecules on the graphite was usually present. This allowed for choosing a measurement site that had discernible

nanofeatures of adsorbed molecules present, while leaving enough graphite surface exposed for comparison. The graphite was exfoliated with Scotch tape after collecting data for each adsorbant, leaving a clean surface for the next measurement. Solvent effects were also tested by applying the same amount of solvent with no dissolved molecules, then taking the same measurements.

#### 4.2.5 Gold Nanoparticle Adsorption onto Graphite

The gold nanoparticles were all adsorbed onto the graphite in the same fashion. The graphite was submerged in a clean solution containing the nanoparticles in water. This solution was left for at least 20 hours at room temperature. The graphite was then taken out of the solution, rinsed lightly, and allowed to completely dry under a stream of nitrogen.

#### 4.2.6 Surface Potential Mapping

An AFM technique, surface potential mapping allows for nanoscale mapping of the electrostatic potential of surfaces. Surface potential mapping is run in tapping mode, and is taken along with topography. This method is shown in Figure 4.7. Explained in Chapter 2, tapping mode measures the topography of the surface by monitoring the oscillation of the probe tip near the surface. To measure the surface potential, a conductive tip is used, and a topographical scan is first taken. The tip is then brought back to the beginning of the scan and raised a set lift height, usually 5 or 10 nm here. The tapping piezo is then turned off, and instead an AC bias is applied to the tip. The tip is then scanned over the same line, tracing the topography mapped previously while staying at the set height. As the tip encounters static potential from the surface, the applied AC bias interacts with it, causing the tip to oscillate. This is caused by electrostatic force acting on the tip<sup>46</sup>



$$F(z,t) = -\frac{1}{2} \frac{\partial C(z)}{\partial z} [(V_{DC} - V_S) + V_{AC} \sin(\omega t)]^2 \quad \text{Eq. 4.1}$$

where  $\partial C/\partial z$  is the gradient of the capacitance between the tip and the surface,  $V_{DC}$  is a DC bias applied to the tip,  $V_S$  is the potential from the surface,  $V_{AC}$  is the AC bias, and  $z$  is the surface normal. When this DC bias is applied to the tip with the AC bias, the force on it from the potential on the surface changes. When the DC bias applied matches the potential from the surface, the force approaches a minimum. The controller applies a set AC bias to the tip, while

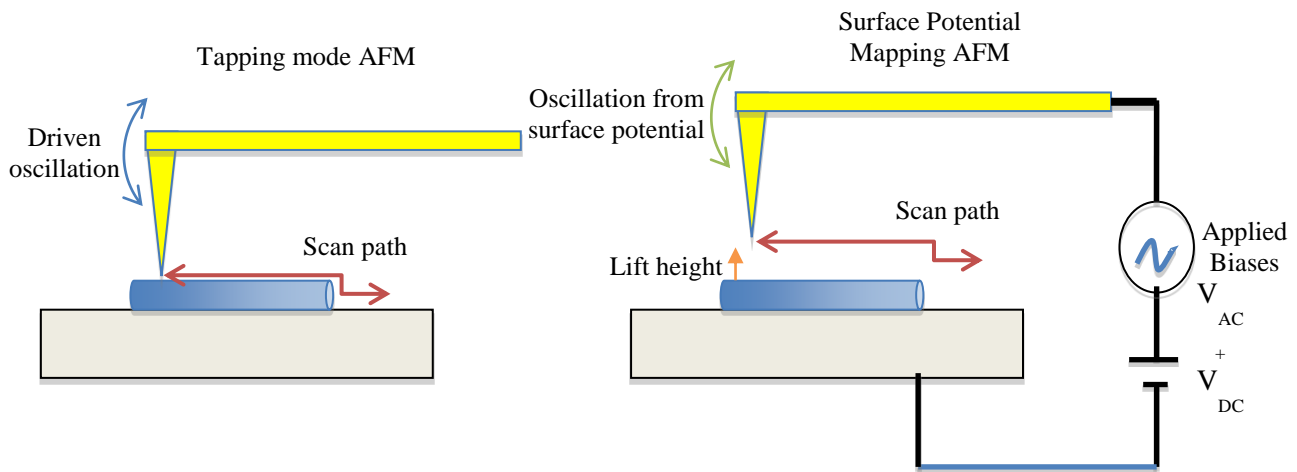


Figure 4.7 Diagram of the surface potential mapping AFM experiment. For every scan, a topography scan (left) is performed first in Tapping mode. The tip is then pulled off the surface to the desired lift height. The conductive tip then scans over the topography trace just recorded, while an AC bias is supplied to the tip. This bias causes the tip to feel a force from the electrostatic potential of the surface and begin to oscillate. A DC bias is then also applied to the tip to bring this force to a minimum. This DC bias versus position is recorded as the surface potential map.

also applying a variable DC bias to keep the oscillation of the tip at this minimum. This DC bias is recorded as a function of position and constructs a potential map of the surface. The potential measured in this fashion is dependent on tip material,<sup>46</sup> however, and can change if the tip changes. Care must be taken to use a clean tip of the same material. Differences in potentials on the same surface are accurate, and the difference between the adsorbate and graphite potentials

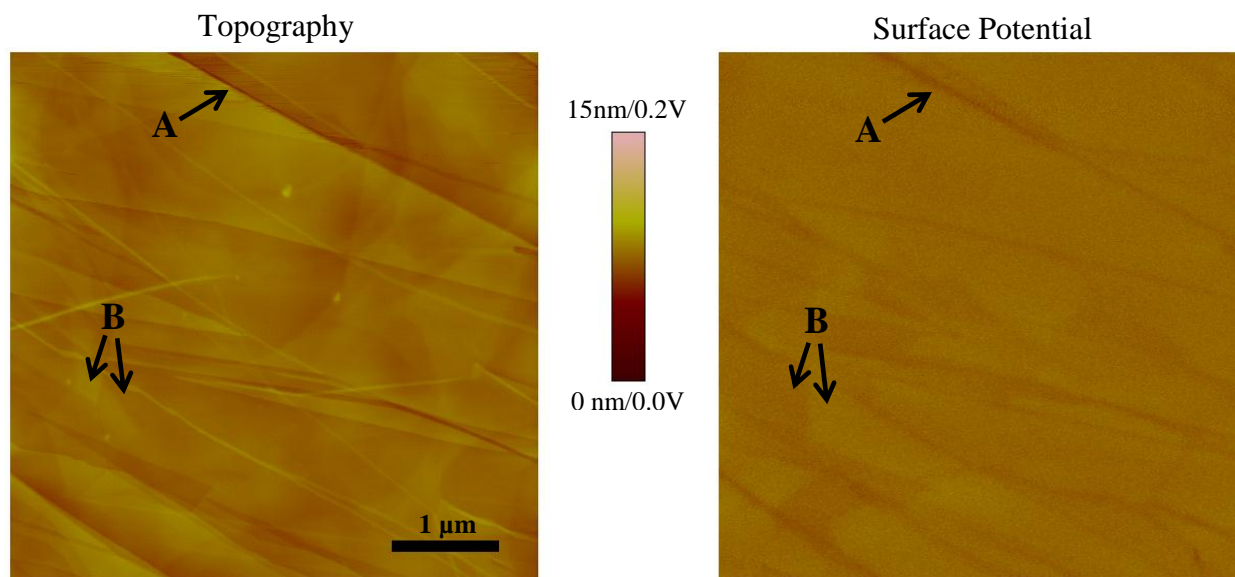


Figure 4.8 Topography (left) and surface potential (right) images of a freshly cleaved graphite surface. The topography has the characteristic sheets and step edges of graphite. In the surface potential image, the negative potential contrast at the step edges can be seen (A), as well as the local variability in the potential in different sheets (B).

can be compared across adsorbates. The graphite surface does have some local variability in potential as well, and can differ between exfoliations. At this stage, the measurements are qualitative. For more quantitative measurements, the substrate and tip would have to be made very consistent across all measurements. This could be done by using the same tip across all measurements and by homogenizing the graphite surface by exposing it to vacuum, as gas may become trapped between the surface sheets during the exfoliation process.

## 4.3 Results and Discussion

### 4.3.1 Azulenes on Graphite

#### 4.3.1.1 Clean Graphite

Freshly cleaved graphite surfaces were imaged as a control. Figure 4.8 shows a typical graphite image. The topography image displays the classic graphite terraces and step edges. At

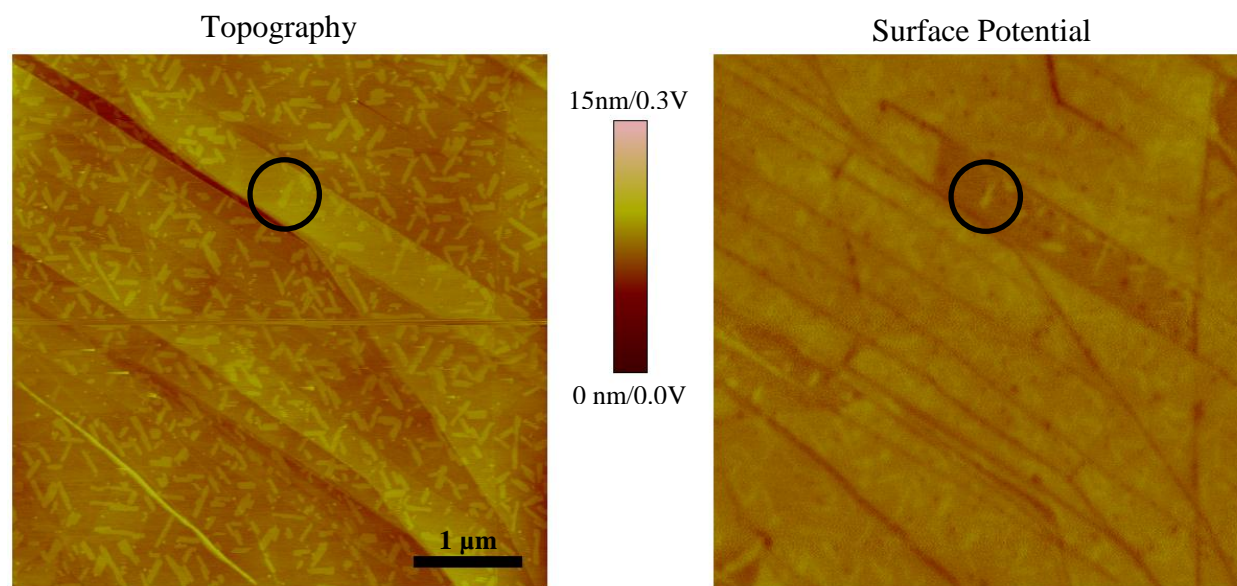


Figure 4.9 Topography (left) and surface potential (right) images of a graphite surface with toluene molecules adsorbed. The toluene nanofeatures are lined up with the hexagonal lattice of the underlying graphite. The surface potential shows that each toluene feature exhibits a positive potential contrast against the graphite sheets. The circle indicates one of these features across both images.

the edges of the sheets, the carbon-carbon bonds have been broken during the cleaving process. These dangling bonds are most likely quickly oxidized in air. Oxygen is more electronegative than carbon, and so in the surface potential image, these step edges almost invariably display a potential that is more negative than the surrounding graphite. This is highlighted by label A. The surface potential image also shows that there can be some local variability in potential of the sheets that make up the graphite surface, highlighted by label B. The sheets are very conductive across their hexagonal lattice, but the conductance between different sheets is lower. This allows for the local variability in sheet potential.

#### 4.3.1.2 Solvent Controls

To rule out any effects introduced by the solvents, each solvent was tested by application to a clean graphite surface with no dissolved molecules. In addition to methylene chloride and benzene, toluene was investigated as a potential solvent. It was quickly ruled out, however, as it

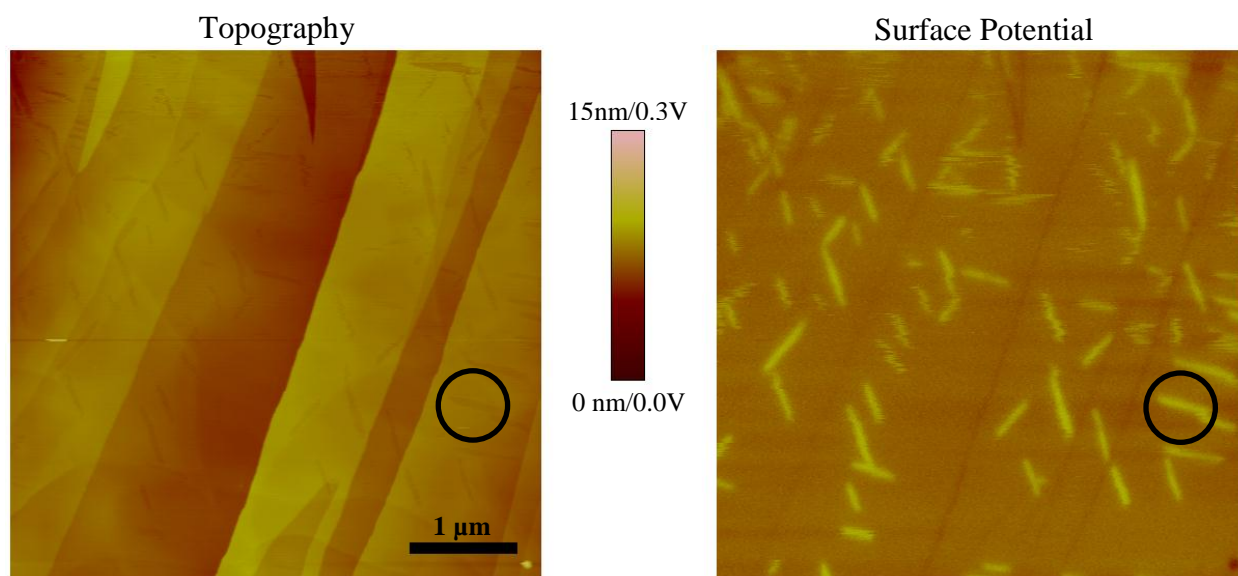


Figure 4.10 Topography (left) and surface potential (right) images of a graphite surface that has been exposed to methylene chloride for over 10 seconds. The graphite sheets show signs of etching; these etches appear to be aligned with the graphite lattice. The surface potential shows that these etches to have a positive potential contrast with the rest of the graphite. The circle indicates one of these etches across both images.

appears to have a strong affinity for the graphite surface and adsorbs readily. As seen in Figure 4.9, the toluene molecules form small, flat oblong features on the graphite surface. These crystals appear in primarily three orientations, with each orientation  $60^\circ$  from the others. This matches the hexagonal lattice of the underlying graphite. The surface potential map of these nanofeatures on graphite shows that the features have a potential slightly more positive than the surrounding graphite. This indicates that electrons have moved from the toluene into the graphite. The HOMO level of toluene may lie close enough to the Fermi level of graphite to interact. In any case, the adsorption of toluene onto the graphite surface ruled toluene out as a potential solvent to carry other molecules to the surface, as it would be difficult to differentiate between toluene and another molecule adsorbed onto the surface in the topography image.

Methylene chloride was then chosen as a solvent because of its non-aromaticity and ability to dissolve most of the azulenes being studied. Upon application to the graphite surface,

methylene chloride can have an etching effect on the surface sheets. This effect only occurs, however, if the surface is exposed to the methylene chloride for a long enough time. At short times, less than 10 seconds, there appears to be no effect. This is shown in Figure 4.10. The etched grooves in the long exposure surface appear to be in line with the hexagonal lattice of the graphite, and show up quite dramatically in the surface potential image. None of these effects are present in the short exposure surface, and so can be avoided by keeping the methylene

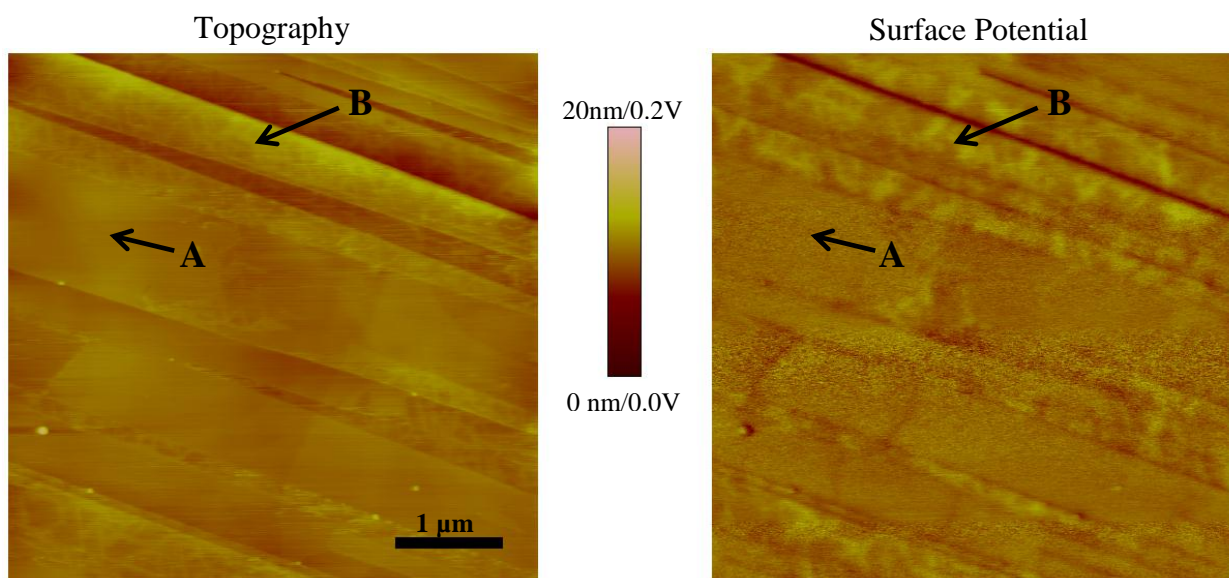


Figure 4.11 Topography (left) and surface potential (right) images of a graphite surface immediately after exposure to benzene. Even though the benzene was neat, it doesn't cover the entire surface. (A) indicates a region with no benzene adsorption, while (B) indicates a region with benzene adsorption. In the surface potential image, benzene has a positive potential contrast against graphite surface.

chloride exposure under 10 seconds.

Benzene was also used as a solvent, mainly for the 1,3 diiodoazulene, as it has a better solubility in benzene than methylene chloride. Since benzene is an aromatic ring, there was concern that it would adsorb too strongly to the graphite surface through  $\pi$ -stacking interactions. Indeed, even a brief exposure of the surface to the benzene will cause some adsorption. Figure 4.11 shows the topography and surface potential images of graphite exposed to benzene. In this

image, the surface is partially covered by the benzene molecules, seen as raised features on some of the terraces, indicated by label B. However, blowing nitrogen over the surface for two minutes was found to remove most, if not all of the adsorbed benzene molecules. Figure 4.12 shows two surfaces, one that has been exposed to benzene and dried under nitrogen, and one that has been briefly exposed to methylene chloride. Both are indistinguishable from a clean graphite image.

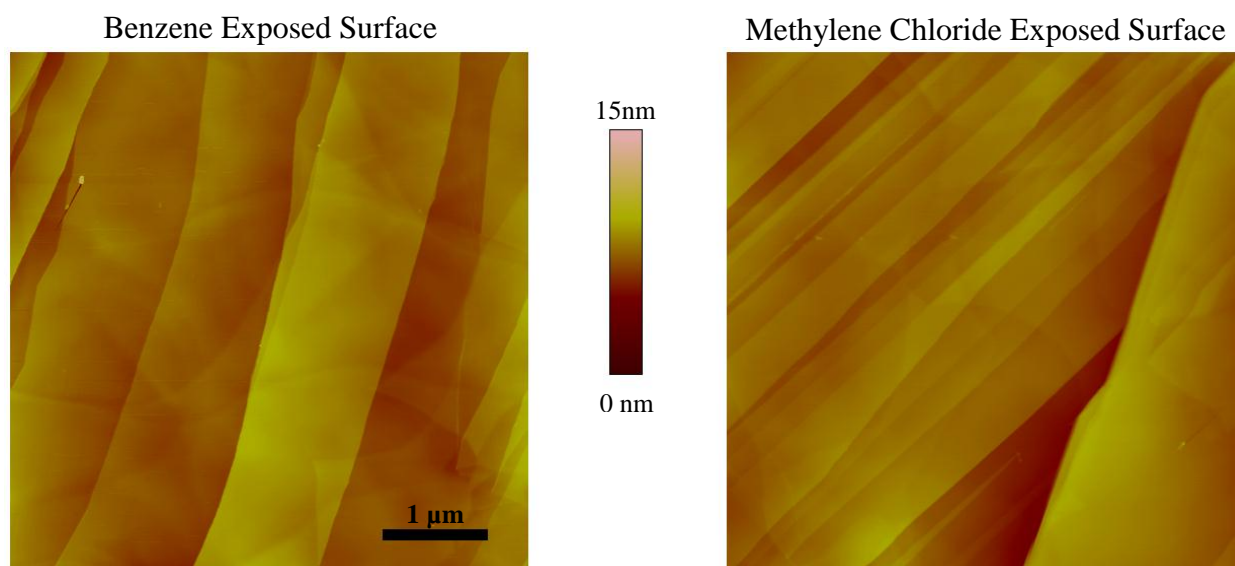


Figure 4.12 Topography images of graphite surfaces after exposure to benzene (left) and methylene chloride (right). The left surface was dried under nitrogen for two minutes to remove any residual benzene. The right surface was exposed to methylene chloride for less than ten seconds. Although solvent can affect the surface, with proper treatment these effects can be avoided.

#### 4.3.1.3 Naphthalene

Naphthalene was adsorbed onto graphite with methylene chloride as the solvent. Naphthalene was studied as a comparison to azulene. The two molecules are isomers, both  $C_{10}H_8$ , but naphthalene's structure is two fused benzene rings, while azulene's structure is fused seven and five membered rings. Naphthalene is similar to the lattice structure of graphite, and

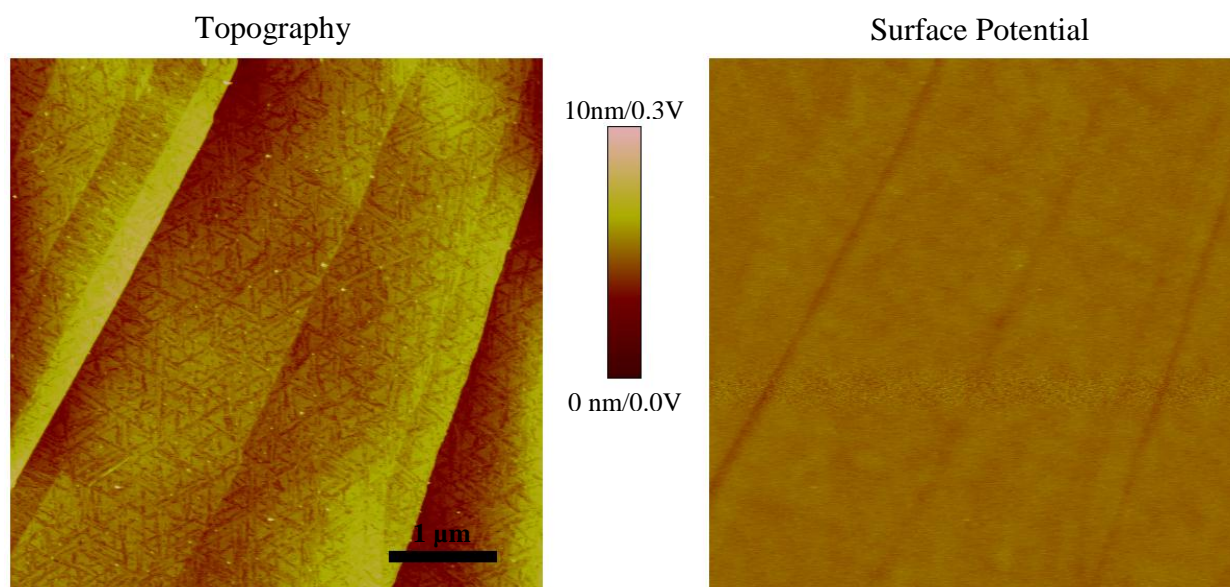


Figure 4.13 Topography (left) and surface potential (right) images of a graphite surface with naphthalene molecules adsorbed. The naphthalene provides almost full coverage of the surface. The surface potential shows the naphthalene with no discernible potential contrast against the graphite. The negative potential contrast of the step edges is clearly visible through the adsorbed naphthalene.

was expected to adsorb well to the surface. Figure 4.13, taken after application of 2 μL of the 0.6 mM solution of naphthalene in methylene chloride to the graphite surface, shows naphthalene covering most of the surface. The topography reveals that flat isosceles triangles dominate the morphology of the deposited naphthalene, with exposed graphite valleys between the nanofeatures. The surface potential map, however, shows that there is little difference in potential between the triangles and the valleys. The step edges of the graphite itself are still easily seen with a more negative potential, even through the deposited naphthalene.

#### 4.3.1.4 Azulene

Azulene was adsorbed onto the graphite surface with methylene chloride as the solvent. Instead of forming ordered features on the surface, as in the case of toluene and naphthalene, the azulene seems to adsorb in mostly flat, irregular features, with some accumulation on step edges. Figure 4.14 shows two sets of topography and surface potential images for azulene on graphite, one set over a larger area that covers many features, and one zoomed in over one feature. The

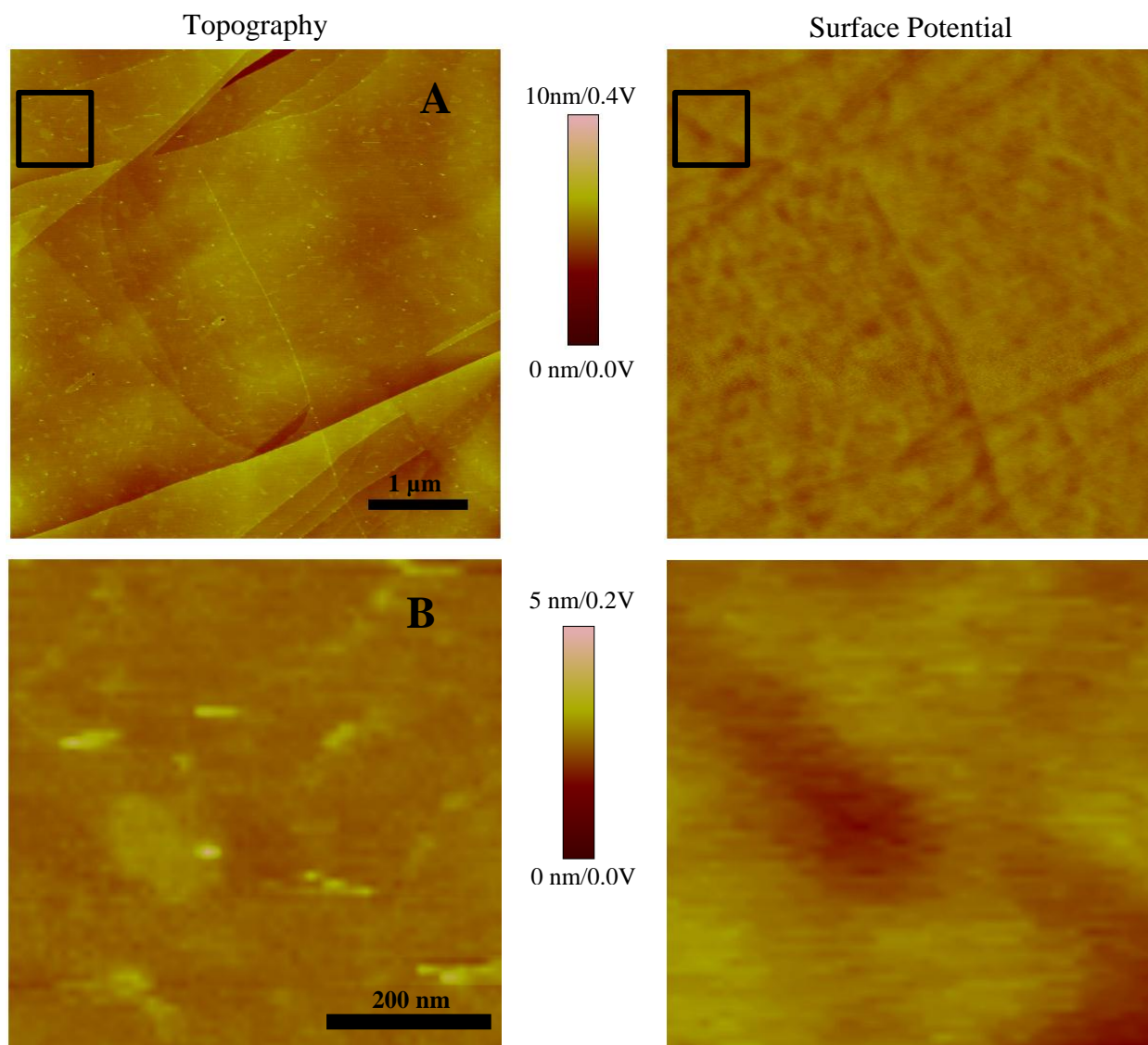


Figure 4.14 Topography (left) and surface potential (right) images of a graphite surface with azulene molecules adsorbed. The azulene adsorbs in small, flat, irregular features. The nanofeatures of azulene exhibit a negative potential contrast against the surrounding graphite surface. (B) is a zoomed in image in (A), indicated by the square.

small bright dots in the zoomed in topography image are believed to be contaminants from the graphite surface. It should also be noted that the feature in the surface potential image appears larger than that in the topography image. This is likely due to a loss in resolution in the surface potential imaging mode. As stated previously, the tip must be lifted off the surface a certain height, and this will have a detrimental effect on resolution. It is readily apparent, however, that the azulene nanofeatures are more negative in the surface potential image than the surrounding



graphite. One explanation for this is that the LUMO level of the azulene is interacting with the Fermi level of the graphite. Since the LUMO of azulene is empty, it would accept electrons, increasing the electron density and thus electrostatic potential, of the azulenes. This would show up as a negative potential contrast.

#### 4.3.1.5 1,3-di(2,2,2-trifluoro-1-oxoethyl)azulene

DTFA was also adsorbed onto graphite with methylene chloride as the solvent. The morphology of DTFA on the surface was more like that of naphthalene than azulene, with some triangular nanofeatures and rectangles forming. There are also larger patches of bare graphite exposed. As seen in Figure 4.15, the DTFA covers a good portion of the surface. The surface potential map clearly shows that the DTFA nanofeatures are very negative in potential compared with the bare graphite areas. A DTFA molecule has 3 fluorine atoms on each substituent, which makes them very electronegative. As these groups are on the odd numbered carbons on azulene, they stabilize the HOMO level. This would cause it to lower in energy. The LUMO remains unaffected. If the LUMO level of azulene with no functional groups interacts with the graphite, then lowering the energy of the HOMO should not have much of an effect, and a strong interaction between the LUMO and the graphite would be observed, as seen with the unsubstituted azulene.

#### 4.3.1.6 1-(2,2,2-trifluoro-1-oxoethyl)azulene

TFA, like DTFA has fluorine atoms, but in this molecule there are only 3. TFA was also adsorbed onto graphite using methylene chloride as a solvent. The TFA morphology adsorbed on the surface looks more like azulene than it does the DTFA, perhaps because it only has one substituent. It is in small, flat, irregular nanofeatures, and there appears to be some balled up

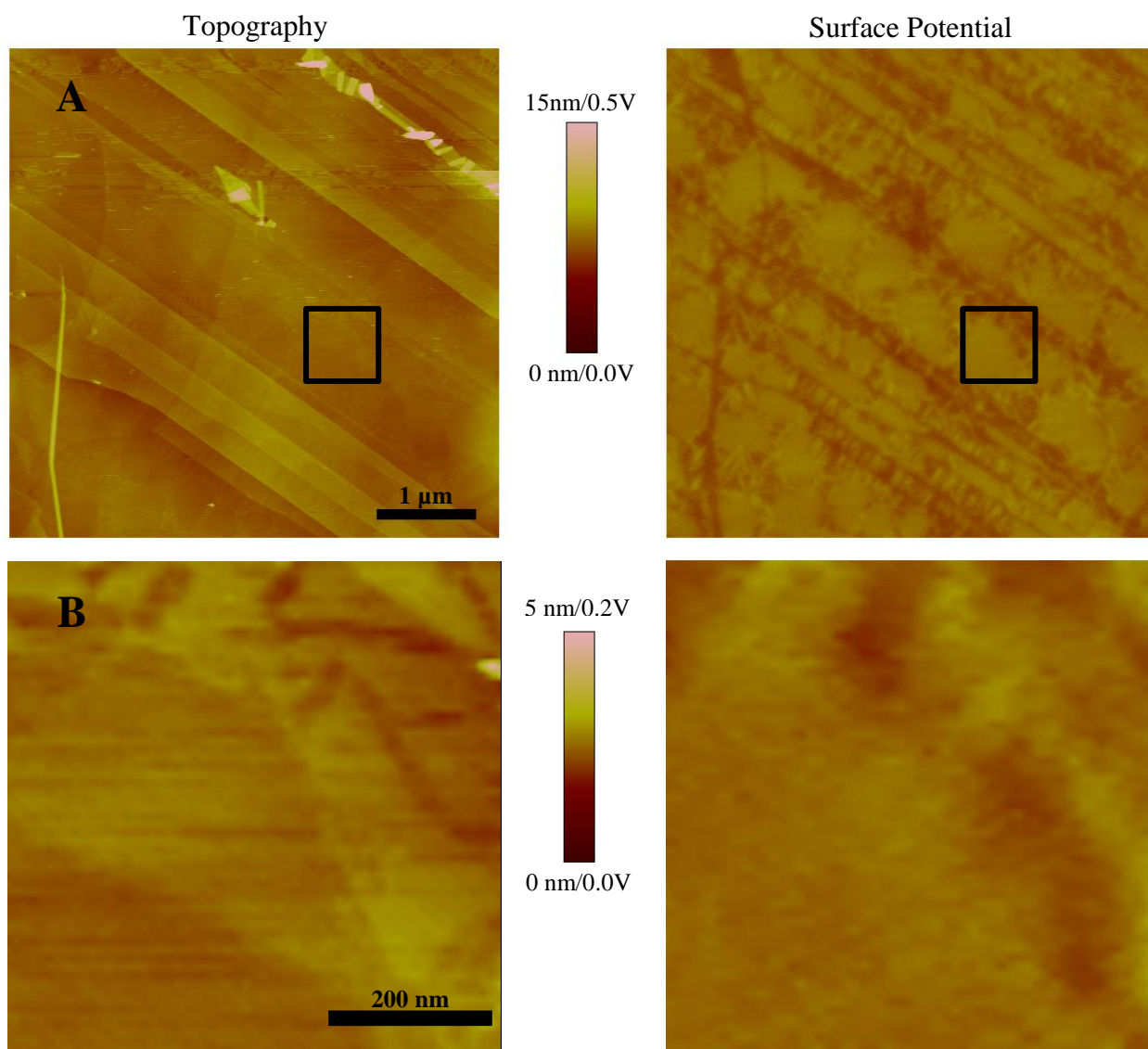


Figure 4.15 Topography (left) and surface potential (right) images of a graphite surface with DTFA molecules adsorbed. The DTFA adsorbs in small triangles and strips, as seen in the topography image, especially near the center. There are also many areas of open graphite. In the surface potential image, these nanofeatures of DTFA exhibit a negative potential against the bare graphite surface. (B) is a zoomed in image in (A), indicated by the square.

material, mostly on step edges. This is seen in Figure 4.16. It is believed that the balled up material is a surface contaminant from the graphite. The small flat nanofeatures in the image in Figure 4.15 are believed to be features of the TFA, as they are consistent with the morphologies of the previous adsorbed molecules. In the surface potential image, these features show up as a negative potential against the graphite background, as the DTFA does. Again, if the LUMO of

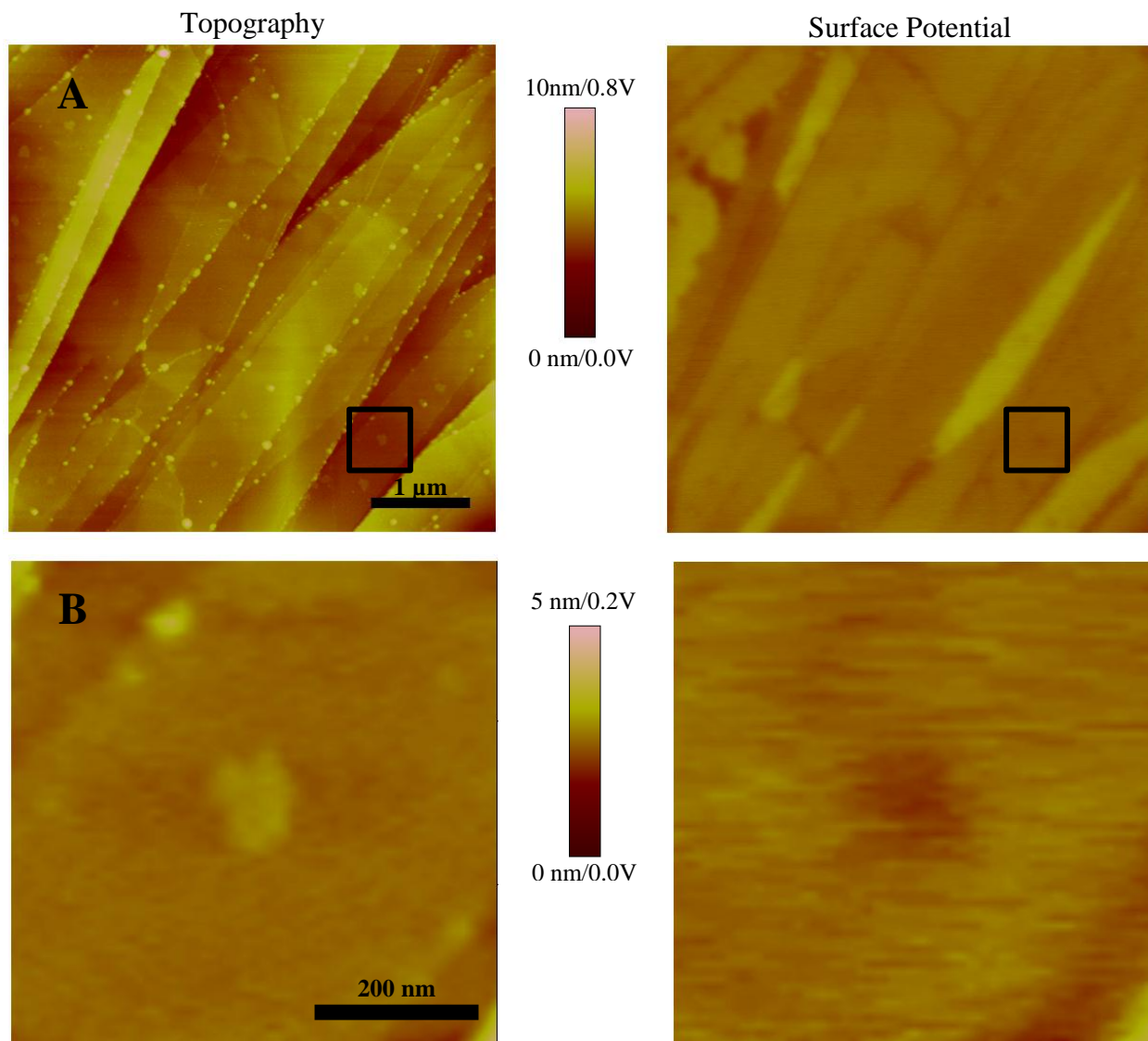


Figure 4.16 Topography (left) and surface potential (right) images of a graphite surface with TFA molecules adsorbed. Like azulene, the TFA seems to adsorb in mostly small, flat, irregular nanofeatures. There is also some accumulation of contaminant at step edges. In the surface potential image, the TFA features show a negative potential contrast against the graphite surface. (B) is a zoomed in image in (A), indicated by the square.

azulene is interacting with the graphite, then lowering the energy of the HOMO should not much affect that interaction. The fact that these molecules also show a negative potential contrast is consistent with this idea.

#### 4.3.1.7 1,3-diiodoazulene

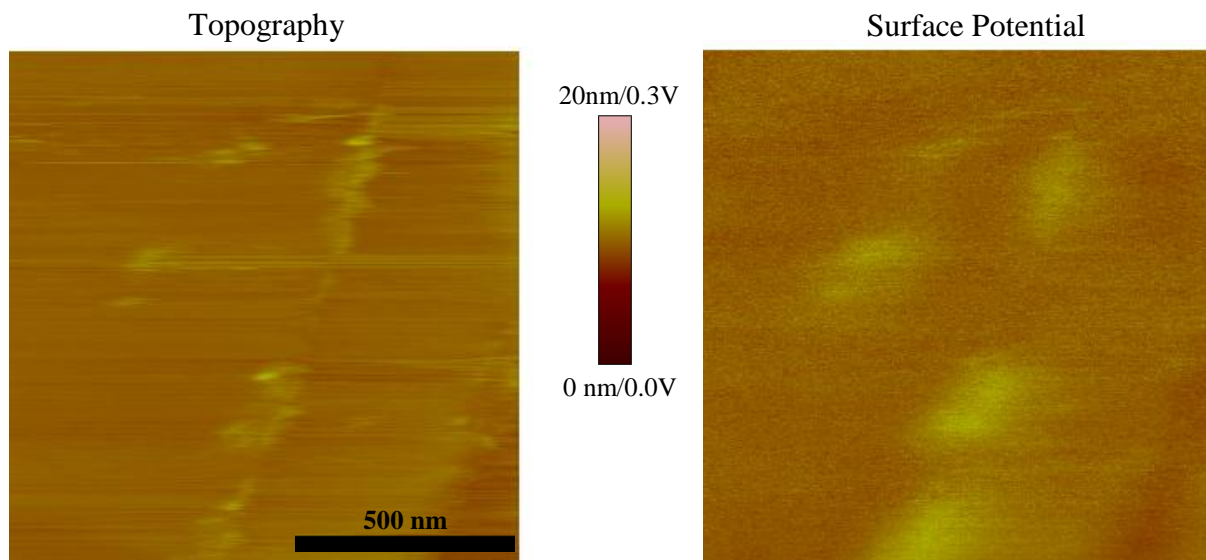


Figure 4.17 Topography (left) and surface potential (right) images of a graphite surface with DIA molecules adsorbed. The DIA adsorbs much less orderly than the previous azulenes and are mostly near step edges with a few clusters on open sheets. The adsorbed DIA molecules stand out as a positive potential against the surrounding graphite surface.

DIA molecules have two iodine atoms at the 1 and 3 position, contrasted to the fluorine containing groups of the DTFA molecules. These iodine groups are electron donating, and instead of stabilizing the HOMO of azulene, it destabilizes it, increasing its energy. DIA was dissolved in benzene and adsorbed onto the graphite surface. This molecule seems to adsorb onto the surface in the most disordered fashion in small groups and on step edges, as seen in Figure 4.17. In the surface potential image, the groups of DIA molecules appear brighter, with a more positive potential, compared with the surrounding graphite. This means that they are somehow giving up electron density to the surrounding graphite. In this molecule, the HOMO level is raised. If this HOMO level interacts with the graphite Fermi level, then electrons from the molecule will enter the graphite, leaving these molecules with a positive potential contrasted with the surrounding graphite. This is what may be happening with the DIA molecules. The HOMO level is raised in this molecule compared to azulene, raised enough that its interaction with the Fermi level of the graphite is dominant over the interaction with the LUMO.

#### 4.3.1.8 Azulenes on Graphite Summary

It is apparent from the data presented that the behavior of different azulenes does depend on the functional groups attached. Azulene was found to have a negative potential contrast with the surrounding graphite. This can be explained by the LUMO of the azulene interacting with the energy levels of the graphite. Since the LUMO is empty, electrons would

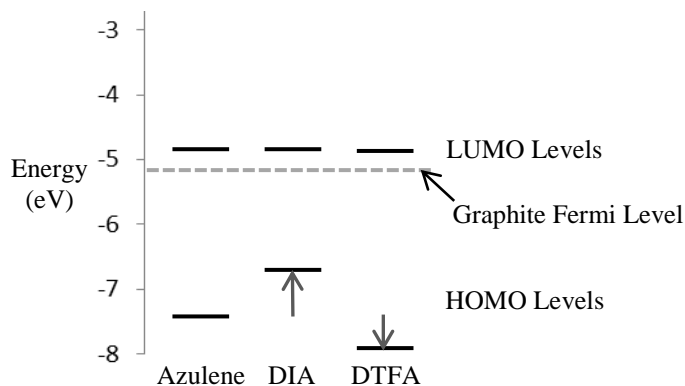


Figure 4.18 Rough approximation of the energy levels of graphite, azulene, DIA, and DTFA. Azulene's LUMO lies close in energy to the Fermi level of graphite. Destabilization of the HOMO by electron donating groups like DIA brings it closer to the Fermi level. Stabilization of the HOMO by electron withdrawing groups like DTFA move it farther away.

enter from the graphite. The DTFA and TFA molecules both have electron withdrawing groups on the 1 and the 3 carbons of the azulene base. This causes stabilization of the HOMO level while leaving the LUMO level unchanged. The LUMO is then still free to interact with the graphite in both of these molecules, thus the negative potential contrast against the graphite surface seen in them both. The DIA molecules, on the other hand destabilize the HOMO by donating electrons. This destabilization increases the energy of the HOMO, raising it up to a level where it can now interact with the Fermi level of the graphite. Thus, electrons from the DIA molecules' HOMO level enter the graphite, causing the positive potential contrast seen in the DIA molecule potential maps. This idea is corroborated by reported data on the work function of graphite and the ionization potential of azulene. A comprehensive review found the work function of graphite to be reported between 4.4 eV and 5.2 eV.<sup>47</sup> The ionization potential of azulene is reported to be 7.42 eV,<sup>48</sup> while the HOMO-LUMO gap is 1.77 eV to 2.63 eV, based

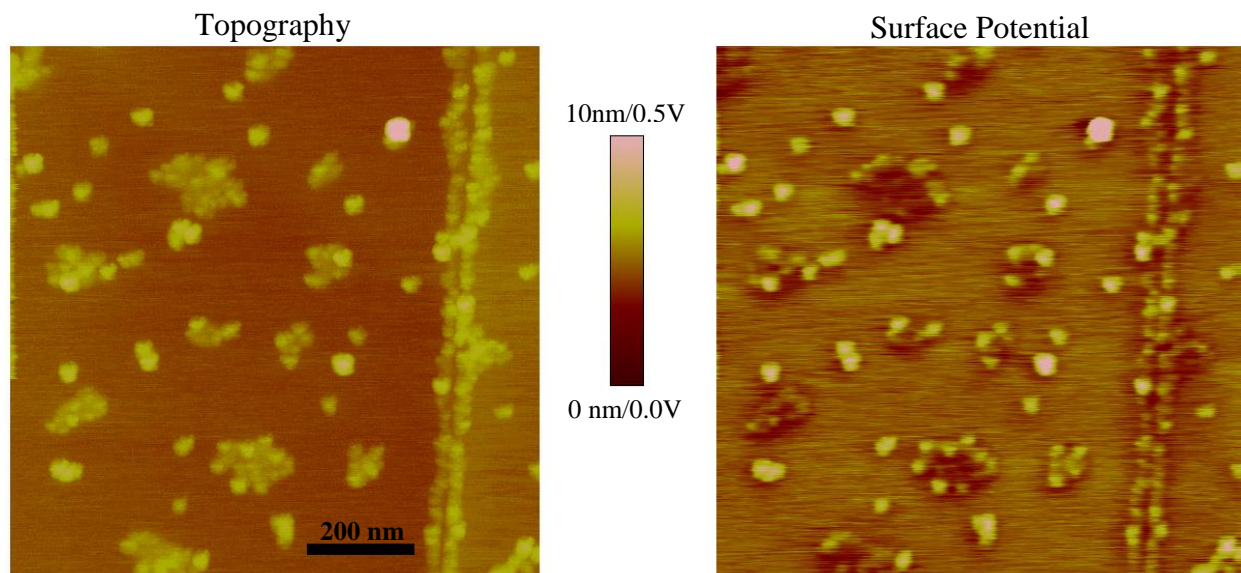


Figure 4.19 Topography (left) and surface potential (right) images of a graphite surface with 40 nm diameter spherical gold nanoparticles adsorbed. The nanoparticles are in groups and singles, and cluster about the step edges. The surface potential image shows that the particles exhibit a positive potential against the graphite surface.

on its visible absorption spectrum.<sup>49</sup> If we take the ionization potential to be the energy of the HOMO, this puts the LUMO within range of the Fermi level of graphite, and agrees with our analysis. Figure 4.18 shows an energy level diagram based on this information, which is a rough approximation. It shows a possible comparison of the energy levels of graphite, azulene, DIA and DTFA. As explained above, destabilization of the HOMO moves this energy level closer to the Fermi level of graphite, while stabilization of the HOMO moves it farther away. This helps provide evidence for the idea that the azulene molecules can function as a tunable adsorbate for graphene-like materials.

## 4.3.2 Gold Nanoparticles on Graphite

### 4.3.2.1 Gold Nanospheres

The nanospheres adsorbed onto the graphite surface well, mostly in clusters and on step edges, but some singly. Figure 4.19 shows the topography and surface potential for some 40 nm

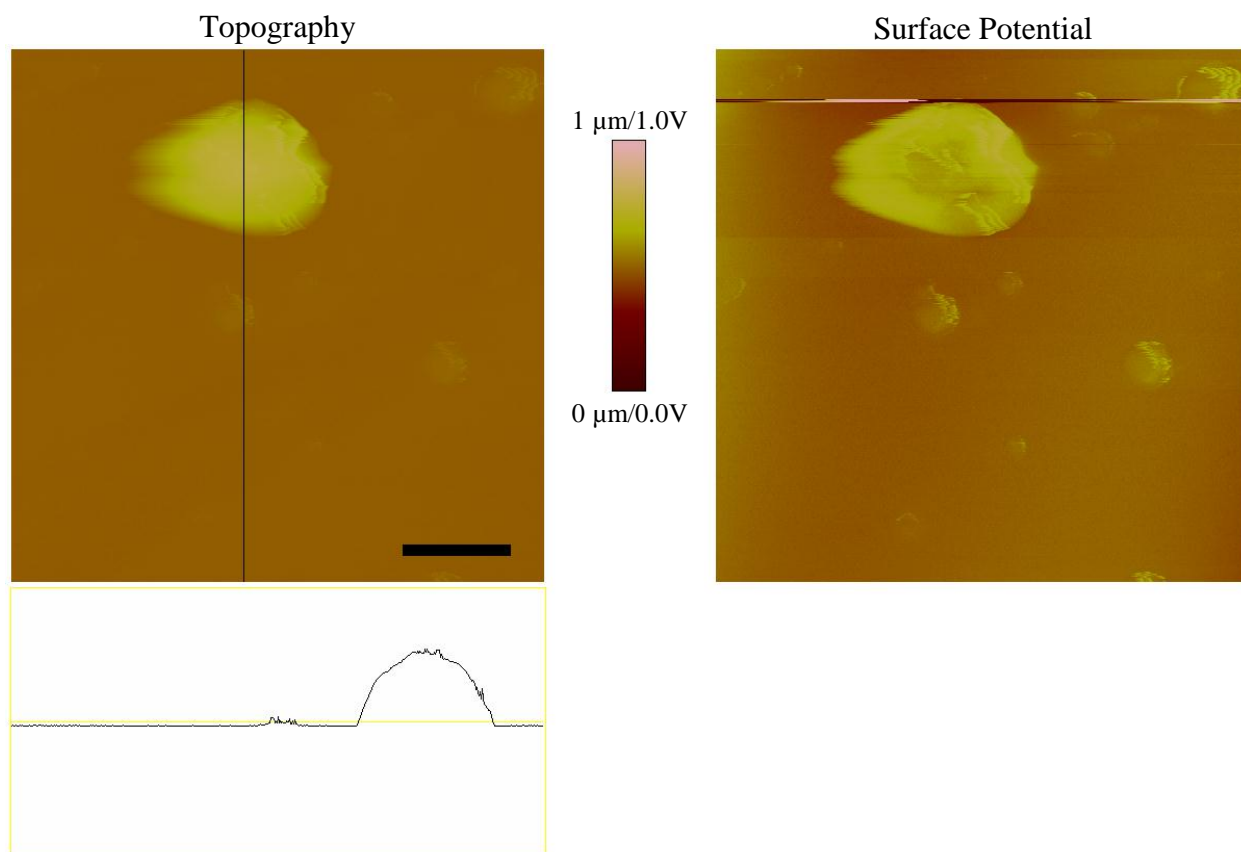


Figure 4.20 Topography and section (left) and surface potential (right) images of a possibly octahedral gold nanoparticle adsorbed onto a graphite surface. The particle is roughly 300 nm in diameter, and in the section through the particle, some edges can be seen. Like the nanospheres, this particle exhibits a positive contrast in the potential against the graphite surface.

gold nanospheres on graphite. In the surface potential, each cluster of particles appears with a positive potential contrast. This means that there is more electron density in the graphite than in the gold nanoparticles. Perhaps, similar to the azulenes, the Fermi level of these nanoparticles is interacting with the graphite surface, giving up some electron density.

#### 4.3.2.2 Gold Octahedral Nanoparticles

The nanoparticles made with the octahedral method came down on the graphite in smaller number than the nanospheres, but they are much larger. Figure 4.20 shows a single nanoparticle that is about 300 nm in diameter. A flat face can be seen in a cross section of the particle, although only the top can be imaged by the AFM. The exact shape is difficult to

discern, although, as stated previously, the absorption spectrum agrees with the literature. The surface potential shows a positive contrast in the particle, similar to the nanospheres, with no appreciable difference, also indicating lower electron density in the particle against the graphite.

#### 4.3.2.3 Gold Nanostars

Like the octahedral nanoparticles, the gold nanostars also adsorbed more sparsely than the nanospheres. Figure 4.21 shows a small cluster of these nanoparticles, probably two or three of them. Although the star shape is not discernible, they are much more irregular shaped than

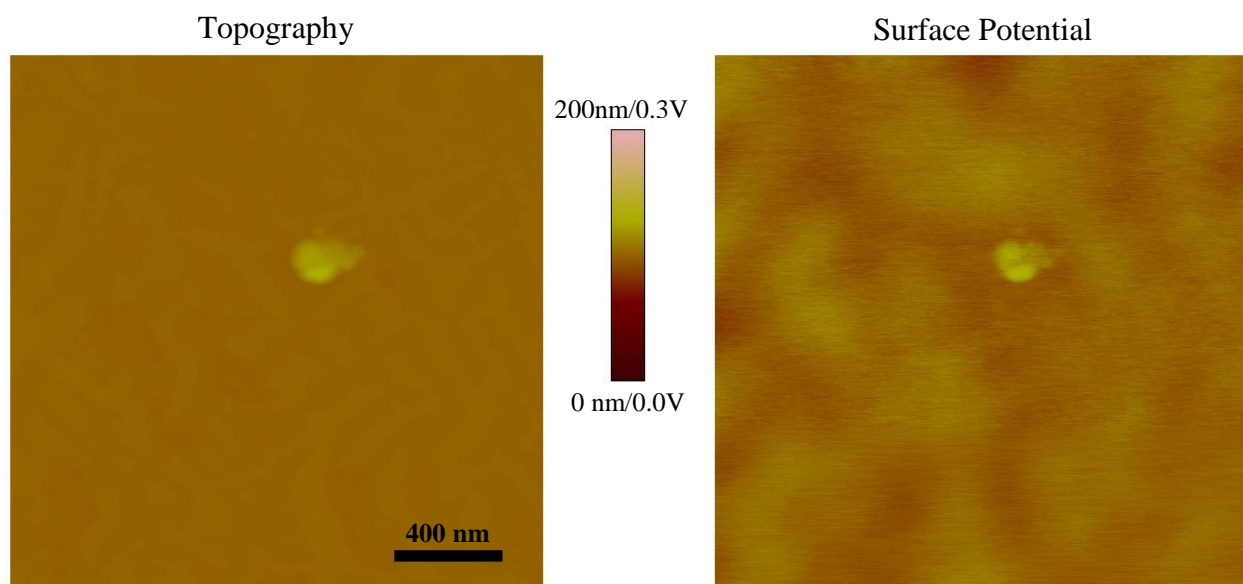


Figure 4.21 Topography (left) and surface potential (right) images of a small cluster (2 or 3 based on size) of gold nanostars on a graphite surface. As with the other nanoparticles studied, these exhibit a positive potential against the graphite surface.

the nanospheres and octahedral particles. The surface potential, though, tells the same story as the other nanoparticles, a positive potential contrast against the graphene.

#### 4.3.2.4 Gold Nanoparticles Summary

The gold nanoparticles were formed and adsorbed well onto the graphite surface. Topography images indicated that the particles were the correct size they should be according to



their synthesis protocol. Each surface potential image showed the nanoparticles in positive contrast to the surrounding graphite. One possible explanation is that the particles are interacting with the graphite Fermi level, much like the azulenes. In this respect we could find no difference in the particles or their effect on the graphite surface. It has been reported that gold nanoparticles have an n-doping effect on graphene.<sup>32</sup> In this study, gold nanoparticles are formed on graphene used in a FET. By measuring the electronic transport properties of the FET decorated with and without the gold nanoparticles, it was determined that the particles n-doped the graphene. This corroborates our findings, that the gold nanoparticles donate electron density to the graphite, and are thus brighter in the surface potential than the graphite surface.

#### **4.4 Conclusion**

The research described here aimed to investigate the nanoscale electrical interaction of adsorbates on a graphite surface through surface potential mapping. It was found that azulene compounds with different substituents, electron donating and withdrawing groups, on odd numbered carbons resulted in opposite surface potential contrasts with the graphite surface. Gold nanoparticles of varying shapes seemed to behave similarly on the surface, showing a positive contrast with the graphite surface. Azulene itself and compounds with electron withdrawing groups, TFA and DTFA, all showed a negative potential contrast compared to the graphite surface. This indicates that the molecules are pulling electron density from the graphite, p-doping it. The azulene compound with electron donating groups, DIA, showed a positive potential contrast against the graphite surface, indicating a sharing of electron density with the surface, n-doping it. These data confirm the idea that azulene compounds may serve as a tunable dopant for graphene-like materials. The ability to control the electronic properties of graphene and graphene-like materials will be key to their incorporation and function in novel devices. For

example, in FETs, graphene used as the channel material must have a controlled band gap, while in solar cells, graphene used as an electrode must behave more like a conductor. Precise control of these properties will enable better and more efficient graphene devices.

Although azulene compounds adsorbed onto graphite and measured with surface potential mapping is a novel system, other adsorbates have been looked at previously. The most similar study looks at two aromatic compounds adsorbed onto exfoliated graphene and few-layer graphene.<sup>34</sup> One compound is heavily fluorinated with electron withdrawing character, while the other has a vanadium center and has electron donating character. To study the interaction of the molecules with the graphene, both surface potential mapping and field effect transistor (FET) experiments were performed. Their surface potential images are similar to the ones shown here; the graphene with the fluorinated molecules adsorbed show darker areas where the molecules have aggregated, while the graphene with the vanadium compound adsorbed shows very slightly brighter areas where there appears to be aggregation. Combined with their FET data, the researchers conclude that the fluorinated compound is pulling electron density from the graphene, while the vanadium compound is donating to it. This corroborates the data shown here, however these molecules do not provide nearly the flexibility of the azulene system for being able to tune the electrical properties of graphene.

Metallic nanoparticles as graphene dopants have also been studied before. There is some disagreement in the literature, however, as to whether gold nanoparticles p-dope or n-dope graphene.<sup>50, 51</sup> In one report, researchers describe deposition of gold onto a graphene sheet in a FET. They load the graphene with varying coverages of gold nanoparticles, and see a p-doping effect in the graphene through the FET electrical characteristics.<sup>50</sup> Another report describes a very similar procedure, again loading a graphene FET with varying amounts of gold

nanoparticles. Here they use Raman measurements as well as FET characteristics to determine the doping activity of the gold nanoparticles. They describe an n-doping effect when the nanoparticles are discrete, which transitions to a p-doping effect at high coverage when the gold nanoparticles begin to interconnect.<sup>51</sup> The results of the presented work agree with findings that the gold nanoparticles n-dope graphene-like materials.

The results of the research presented here support the idea that azulene compounds hold promise for use as adsorbates to tune the electrical properties of graphene-like materials. The large tunability of azulene compounds' own energy levels, the HOMO and the LUMO, make them a unique system for this purpose. Gold nanoparticles were also found to n-dope the graphite surface, affirming previous studies that found similar results. Graphene-like materials are being investigated for use in many nanoscale and nanostructured devices, such as FETs, solar cells, and fuel cells, and control of the graphene-like material's electronic properties is important for the proper function and efficiency of these devices. For use as the transparent electrode in solar cells, for example, the Fermi level of the graphene must be in proper alignment with the energy levels of the other materials to maximize efficiency. A method for tuning this Fermi level to suit the needs of specific devices will enable the fabrication of more functional and efficient devices.

## References

1. S.M.-M. Dubois, Z. Z., X. Declerck, and J.-C. Charlier, *Electronic properties and quantum transport in Graphene-based nanostructures*. The European Physical Journal B. **2009**, 72, 1-24.
2. Shevyakov, S. V.; Li, H.; Muthyala, R.; Asato, A. E.; Croney, J. C.; Jameson, D. M.; Liu, R. S. H., *Orbital Control of the Color and Excited State Properties of Formylated and Fluorinated Derivatives of Azulene*. The Journal of Physical Chemistry A. **2003**, 107 (18), 3295-3299.
3. Wei, W.; Qu, X., *Extraordinary Physical Properties of Functionalized Graphene*. Small. **2012**, 8 (14), 2138-2151.
4. Lee, S.; Yeo, J. S.; Ji, Y.; Cho, C.; Kim, D. Y.; Na, S. I.; Lee, B. H.; Lee, T., *Flexible organic solar cells composed of P3HT:PCBM using chemically doped graphene electrodes*. Nanotechnology. **2012**, 23 (34).
5. Kwon, O. S.; Park, S. J.; Hong, J. Y.; Han, A. R.; Lee, J. S.; Lee, J. S.; Oh, J. H.; Jang, J., *Flexible FET-Type VEGF Aptasensor Based on Nitrogen-Doped Graphene Converted from Conducting Polymer*. ACS Nano. **2012**, 6 (2), 1486-1493.
6. Antolini, E., *Graphene as a new carbon support for low-temperature fuel cell catalysts*. Appl. Catal. B-Environ. **2012**, 123, 52-68.
7. Chang, T.; Geng, J.; Guo, X., *Chirality- and size-dependent elastic properties of single-walled carbon nanotubes*. Appl. Phys. Lett. **2005**, 87 (25), 251929.
8. Vasic, D. B.; Lukic, P. M.; Lukic, V. M.; Sasic, R. M., *Analytical model of CNT FET current-voltage characteristics*. J. Optoelectron. Adv. Mater. **2012**, 14 (1-2), 176-182.
9. Chen, J.; Lei, W.; Zhang, X. B., *Enhanced Electron Transfer Rate for Quantum Dot Sensitized Solar Cell Based on CNT-TiO<sub>2</sub> Film*. J. Nanosci. Nanotechnol. **2012**, 12 (8), 6476-6479.
10. Manivannan, S.; Saranya, A. M.; Renganathan, B.; Sastikumar, D.; Gobi, G.; Park, K. C., *Single-walled carbon nanotubes wrapped poly-methyl methacrylate fiber optic sensor for ammonia, ethanol and methanol vapors at room temperature*. Sens. Actuator B-Chem. **2012**, 171, 634-638.
11. Hahnlein, B.; Handel, B.; Pezoldt, J.; Topfer, H.; Granzner, R.; Schwierz, F., *Side-gate graphene field-effect transistors with high transconductance*. Appl. Phys. Lett. **2012**, 101 (9), 093504.
12. Mun, J. H.; Cho, B. J., *Physical-gap-channel graphene field effect transistor with high on/off current ratio for digital logic applications*. Appl. Phys. Lett. **2012**, 101 (14), 143102.
13. Cao, J.; Ionescu, A. M., *Study on dual-lateral-gate suspended-body single-walled carbon nanotube field-effect transistors*. Solid-State Electronics. **2012**, 74 (0), 121-125.
14. Seo, M. H.; Choi, S. M.; Seo, J. K.; Noh, S. H.; Kim, W. B.; Han, B., *The graphene-supported palladium and palladium-yttrium nanoparticles for the oxygen reduction and ethanol oxidation reactions: Experimental measurement and computational validation*. Applied Catalysis B: Environmental. **2013**, 129 (0), 163-171.
15. Lee, J. W.; Ko, J. M.; Kim, J.-D., *Hydrothermal preparation of nitrogen-doped graphene sheets via hexamethylenetetramine for application as supercapacitor electrodes*. Electrochimica Acta. **2012**, 85 (0), 459-466.
16. Tang, B.; Hu, G., *Two kinds of graphene-based composites for photoanode applying in dye-sensitized solar cell*. Journal of Power Sources. **2012**, 220 (0), 95-102.
17. Josef, V.; Attila, J. M.; Dan, L.; David, O.; Gordon, W.; Ray, B.; Anvar, Z., *Carbon nanotube/graphene nanocomposite as efficient counter electrodes in dye-sensitized solar cells*. Nanotechnology. **2012**, 23 (8), 085201.
18. Jang, H.-S.; Yun, J.-M.; Kim, D.-Y.; Park, D.-W.; Na, S.-I.; Kim, S.-S., *Moderately reduced graphene oxide as transparent counter electrodes for dye-sensitized solar cells*. Electrochimica Acta. **2012**, 81 (0), 301-307.
19. Gunho, J.; Minhyeok, C.; Sangchul, L.; Woojin, P.; Yung Ho, K.; Takhee, L., *The application of graphene as electrodes in electrical and optical devices*. Nanotechnology. **2012**, 23 (11), 112001.

20. Scarselli, M.; Castrucci, P.; Crescenzi, M. D., *Electronic and optoelectronic nano-devices based on carbon nanotubes*. Journal of Physics: Condensed Matter. **2012**, 24 (31), 313202.
21. Kim, J., *Large-Scale Integrated Carbon Nanotube Gas Sensors*. J. Nanomater. **2012**.
22. Zhang, Z. Y.; Wang, S.; Peng, L. M., *High-performance doping-free carbon-nanotube-based CMOS devices and integrated circuits*. Chin. Sci. Bull. **2012**, 57 (2-3), 135-148.
23. Shen, C. C.; Lin, C. T.; Li, L. J.; Liu, H. L., *Charge dynamics and electronic structures of monolayer graphene with molecular doping*. Appl. Phys. Lett. **2012**, 101 (11), 111907-4.
24. Sławińska, J.; Dabrowski, P.; Zasada, I., *Doping of graphene by a Au(111) substrate: Calculation strategy within the local density approximation and a semiempirical van der Waals approach*. Physical Review B. **2011**, 83 (24), 245429.
25. Wang, R.; Wang, S. N.; Zhang, D. D.; Li, Z. J.; Fang, Y.; Qiu, X. H., *Control of Carrier Type and Density in Exfoliated Graphene by Interface Engineering*. ACS Nano. **2011**, 5 (1), 408-412.
26. Gu, G.; Xie, Z., *Modulation doping of graphene: An approach toward manufacturable devices*. Appl. Phys. Lett. **2011**, 98 (8), 083502-3.
27. Jang, W. S.; Chae, S. S.; Lee, S. J.; Song, K. M.; Baik, H. K., *Improved electrical conductivity of a non-covalently dispersed graphene-carbon nanotube film by chemical p-type doping*. Carbon. **2012**, 50 (3), 943-951.
28. Eva Y. Andrei, G. L., and Xu Du, *Electronic properties of graphene: a perspective from scanning tunneling microscopy and magnetotransport*. Reports on Progress in Physics. **2012**, 75, 47.
29. Champlain, J. G., *A first principles theoretical examination of graphene-based field effect transistors*. J. Appl. Phys. **2011**, 109 (8), 084515-19.
30. Carot, M. L.; Torresi, R. M.; Garcia, C. D.; Esplandiu, M. J.; Giacomelli, C. E., *Electrostatic and Hydrophobic Interactions Involved in CNT Biofunctionalization with Short ss-DNA*. J. Phys. Chem. C. **2010**, 114 (10), 4459-4465.
31. Gautam, M.; Jayatissa, A. H., *Ammonia gas sensing behavior of graphene surface decorated with gold nanoparticles*. Solid-State Electronics. **2012**, 78, 159-165.
32. Huh, S.; Park, J.; Kim, K. S.; Hong, B. H.; Bin Kim, S., *Selective n-Type Doping of Graphene by Photo-patterned Gold Nanoparticles*. ACS Nano. **2011**, 5 (5), 3639-3644.
33. Kozlov, S. M.; Vines, F.; Gorling, A., *Bandgap Engineering of Graphene by Physisorbed Adsorbates*. Adv. Mater. **2011**, 23 (22-23), 2638-+.
34. Wang, X. M.; Xu, J. B.; Xie, W. G.; Du, J., *Quantitative Analysis of Graphene Doping by Organic Molecular Charge Transfer*. J. Phys. Chem. C. **2011**, 115 (15), 7596-7602.
35. Chen, W.; Chen, S.; Qi, D. C.; Gao, X. Y.; Wee, A. T. S., *Surface transfer p-type doping of epitaxial graphene*. J. Am. Chem. Soc. **2007**, 129 (34), 10418-10422.
36. Coletti, C.; Riedl, C.; Lee, D. S.; Krauss, B.; Patthey, L.; von Klitzing, K.; Smet, J. H.; Starke, U., *Charge neutrality and band-gap tuning of epitaxial graphene on SiC by molecular doping*. Physical Review B. **2010**, 81 (23).
37. Jiang, H.; Sabarinathan, J.; Manifar, T.; Mittler, S., *3-D FDTD Analysis of Gold-Nanoparticle-Based Photonic Crystal on Slab Waveguide*. J. Lightwave Technol. **2009**, 27 (13), 2264-2270.
38. Shukla, S.; Baev, A.; Jee, H.; Hu, R.; Burzynski, R.; Yoon, Y. K.; Prasad, P. N., *Large-Area, Near-Infrared (IR) Photonic Crystals with Colloidal Gold Nanoparticles Embedding*. ACS Appl. Mater. Interfaces. **2010**, 2 (4), 1242-1246.
39. Nengsih, S.; Umar, A. A.; Salleh, M. M.; Oyama, M., *Detection of Formaldehyde in Water: A Shape-Effect on the Plasmonic Sensing Properties of the Gold Nanoparticles*. Sensors. **2012**, 12 (8), 10309-10325.
40. Wehling, T. O.; Katsnelson, M. I.; Lichtenstein, A. I., *Adsorbates on graphene: Impurity states and electron scattering*. Chem. Phys. Lett. **2009**, 476 (4-6), 125-134.
41. Zhang, W. J.; Lin, C. T.; Liu, K. K.; Tite, T.; Su, C. Y.; Chang, C. H.; Lee, Y. H.; Chu, C. W.; Wei, K. H.; Kuo, J. L.; Li, L. J., *Opening an Electrical Band Gap of Bilayer Graphene with Molecular Doping*. ACS Nano. **2011**, 5 (9), 7517-7524.

42. Szafranek, B. N.; Schall, D.; Otto, M.; Neumaier, D.; Kurz, H., *High On/Off Ratios in Bilayer Graphene Field Effect Transistors Realized by Surface Dopants*. *Nano Lett.* **2011**, *11* (7), 2640-2643.
43. Kumar, D.; Meenan, B. J.; Mutreja, I.; D'Sa, R.; Dixon, D., *Controlling the Size and Size Distribution of Gold Nanoparticles: A Design of Experiment Study*. *International Journal of Nanoscience*. **2012**, *2*.
44. Gwo, S.; Lin, M.-H.; He, C.-L.; Chen, H.-Y.; Teranishi, T., *Bottom-Up Assembly of Colloidal Gold and Silver Nanostructures for Designable Plasmonic Structures and Metamaterials*. *Langmuir*. **2012**, *28* (24), 8902-8908.
45. Sau, T. K.; Rogach, A. L.; Döblinger, M.; Feldmann, J., *One-Step High-Yield Aqueous Synthesis of Size-Tuneable Multispiked Gold Nanoparticles*. *Small*. **2011**, *7* (15), 2188-2194.
46. Melitz, W.; Shen, J.; Kummel, A. C.; Lee, S., *Kelvin probe force microscopy and its application*. *Surface Science Reports*. **2011**, *66* (1), 1-27.
47. Kawano, H., *Effective work functions for ionic and electronic emissions from mono- and polycrystalline surfaces*. *Progress in Surface Science*. **2008**, *83* (1-2), 1-165.
48. Lias, S. G., Ionization Energy Evaluation. In *NIST Chemistry WebBook, NIST Standard Reference Database Number 69* [Online] Linstrom, P. J.; Mallard, W. G., Eds. National Institute of Standards and Technology: Gaithersburg MD, 20899. <http://webbook.nist.gov> (accessed Dec. 9, 2012).
49. Liu, R. S. H., *Colorful Azulene and Its Equally Colorful Derivatives*. *Journal of Chemical Education*. **2002**, *79* (2), 183.
50. Ren, Y. J.; Chen, S. S.; Cai, W. W.; Zhu, Y. W.; Zhu, C. F.; Ruoff, R. S., *Controlling the electrical transport properties of graphene by in situ metal deposition*. *Appl. Phys. Lett.* **2010**, *97* (5).
51. Wu, Y. P.; Jiang, W.; Ren, Y. J.; Cai, W. W.; Lee, W. H.; Li, H. F.; Piner, R. D.; Pope, C. W.; Hao, Y. F.; Ji, H. X.; Kang, J. Y.; Ruoff, R. S., *Tuning the Doping Type and Level of Graphene with Different Gold Configurations*. *Small*. **2012**, *8* (20), 3129-3136.

## **Chapter 5: Conclusions and Future Directions**

### **5.1 Overview**

The research presented in this dissertation investigated the fabrication and electronic properties of nanoscale features for use in novel nanodevices using AFM as both a tool for nanoscale physical and chemical modification and an instrument for nanoscale topographical and electronic properties analysis. As a whole, this work has brought us closer to the design and fabrication of nanoscale and nanostructured devices, such as the ATP synthase rotor nanodevice described in Chapter 1 or a solar cell utilizing adsorbate tuned CNTs to channel electrons. The capability to analyze the nanoscale physical and electronic interaction of components of such devices, through topographical and surface potential imaging, has also been demonstrated, and is crucial to improving device function and implementation. This work is described across two chapters. Chapter 3 focuses on nanofabrication through nanoscale physical and chemical manipulation, while Chapter 4 focuses on nanoscale manipulation and characterization of electronic properties.

Chapter 3 describes the formation of chemical nanopatterns using both nanoshaving/grafting and oxidative lithography techniques. These patterns were formed in SAMs on two substrates, gold and silicon oxide. They were also formed under varying conditions including tip velocity, bias, and number of passes to investigate the effect of these variables on nanopattern formation. Copper nanofeatures were then fabricated on these nanopatterns with an electroless copper plating solution and subsequently characterized with tapping mode AFM.

Chapter 4 discusses research investigating the nanoscale electronic interaction of adsorbates with graphite surfaces. Surface potential mapping was used to investigate this nanoscale electronic interaction. The adsorbates investigated were azulene compounds with either electron donating groups or electron withdrawing groups as substituents and gold nanoparticles of various shapes. It was found that the different azulene compounds did behave differently on the graphite surface. Azulene and azulene compounds with electron withdrawing groups on odd numbered carbons appeared more negative in potential with respect to the graphite surface, while those with electron donating groups on odd numbered carbons appeared more positive. The gold nanoparticles, however, showed no difference and were all positive in potential with respect to the graphite surface, indicating the shape does not affect the electrical interaction between the nanoparticles and the graphite surface at these length scales. This chapter offers concluding remarks on the work presented in this dissertation, and outlines the future direction, both short and long term, for each project.

## **5.2 Nanofabrication of Copper Features**

### **5.2.1 Conclusion**

The copper nanofeatures formed with the oxidative lithography and electroless copper plating described in Chapter 3 had measured widths down to 210 nm on gold substrates, and 40 nm on silicon oxide substrates. As mentioned in Chapter 3, compared with recent publications describing the directed formation of metallic nanofeatures, this method is relatively simpler and the nanofeatures formed are slightly more narrow.<sup>1, 2, 3</sup> The Sagiv group have reported silver nanofeatures with half-widths down to 33 nm on an OTS on silicon oxide system using a combination of oxidative lithography and silver electroplating with a silver coated stamp.<sup>1</sup> In



another paper, a method is described using a conductive AFM tip to directly reduce copper ions from a copper(II) acetate layer formed on a SAM, forming rough and non-continuous features down to 35 nm in width.<sup>2</sup> On gold substrates, copper nanofeature formation has been recently reported using a dip-pen lithography technique to first form the chemical nanopattern, then form the resist SAM around it.<sup>3</sup> Electroless plating is then used to form copper nanofeatures down to 400 nm in width. Compared to other methods described in the literature, the nanofeature formation method presented here is more directed, controllable, and simpler. There are still issues to be worked out, however, namely feature continuity and control across substrates. The copper nanofeatures formed on OTS on silicon oxide, although smaller in width, were less solid and continuous compared with previously reported nanofeatures. To function as nanowires and electrical interconnects, this must be improved upon. The growth of the copper nanofeature was also shown to be much different on ODT on gold than on the OTS on silicon oxide systems. A full understanding of the differences here would allow more control over nanofeature growth and formation, and would offer insight into the mechanism for the formation of the copper nanofeatures.

This method has great potential to provide a way to form very directed, arbitrarily shaped metal nanofeatures and has implications for nanodevice prototyping and nanoscale electronic interconnects. The availability of an easy and controllable method for forming metallic nanofeatures will facilitate the design and fabrication of novel nanodevices and circuitry. The example shown in Chapter 1 utilizing a molecular rotor, ATP synthase, is a good demonstration of how this method could be incorporated into novel nanodevice fabrication. Another example is the possibility of interconnecting nanoscale FETs for the fabrication of nanoscale logic gates.

These examples highlight the potential of this method to enable more advances in nanodevice and circuitry design and implementation.

### 5.2.2 Future Direction

The metal nanofeatures formed by this method have good placement and shape control, but could have better size and continuity control on the gold and silicon oxide substrates, respectively. Better control of these aspects will lead to more consistent and solid metal nanofeatures. The next experiments in this project will focus on further optimizing the oxidative lithography and copper plating steps by systematically investigating lithography and plating parameters. For use in electronic nanodevices, the electronic properties of the nanofeatures must be characterized. As metal nanowires become smaller, their electronic properties change, and resistance increases. Knowing how these properties change with the size and shape of nanofeatures formed with this method will help in incorporation of the nanofeatures into devices. Nanofeatures will be formed between microelectrodes for resistance measurements. Metals other than copper, such as silver and gold, will be explored as well to broaden the scope of the method.

#### 5.2.2.1 Oxidative Lithography and Electroless Copper Plating Optimization

The copper features formed on the ODT on gold system were much larger in width than the features formed on the OTS on silicon oxide system. The oxidative lithography formed a wider nanopattern on the ODT on gold; this process can be optimized further to form narrower patterns. Factors that control this width include tip velocity, passes, bias, and humidity. In the presented work, the humidity was not manually controlled. Since the humidity controls the size of the meniscus that forms between the tip and the surface, this should also control nanopattern

width. A set of experiments exploring the effects of humidity on nanopattern formation would elucidate the humidity's effect on this formation and may help control nanopattern width during formation.

Although the copper nanofeatures formed on the OTS on silicon oxide system were more controllable in width than on the ODT on gold system, the continuity of these features was much less controlled. The features were rough and non-continuous, and there was much non-specific deposition surrounding the nanopatterns. It has been reported that increasing the temperature of the system during the copper plating process can lead to a reduction in non-specific deposition.<sup>4</sup> Here, researchers increased the electroless plating solution to 45°C and found no evidence of copper deposition on the methyl terminated SAMs, only on carboxyl terminated SAMs. It is thought that the copper ions are destabilized at the interface between the solution and the SAM at higher temperatures. Investigating the effects of higher temperatures on the electroless plating of copper on the OTS on silicon system will determine if this is a route for reducing the amount of non-specific copper deposition. It has also been reported that exposing the carboxyl terminated nanopatterns to a copper ion solution before treatment with the electroless plating solution can reduce non-specific deposition, and may also help form more continuous copper nanofeatures.<sup>3</sup> Here, the patterns were exposed to an ethanolic solution of copper(II) perchlorate for one hour prior to electroless plating. This step seeds the carboxyl terminated nanopatterns with  $\text{Cu}^{2+}$  ions. Exploring this seeding step could lead to more continuous copper nanofeatures and less non-specific deposition.

#### 5.2.2.2 Copper Nanofeature Electronic Properties Characterization

After optimization of copper nanofeature formation, the electronic properties of the features will be measured. As the diameter of copper wires decreases, the resistivity increases. This is due to electron scatter effects from the surface of the wire, as well as scattering at grain boundaries. Research has been done on copper nanowires as narrow as 15 nm.<sup>5</sup> It was found that the resistivity of these grain boundary free nanowires was 5.67  $\mu\Omega$  cm for 15 nm diameters and 3.58 for 30 nm diameters at 295 K. The resistivity of bulk copper is reported at 1.712  $\mu\Omega$  cm at 298 K.<sup>6</sup> The reported resistivities of these copper nanowires are greater than bulk copper, but still within the limits of being a decent conductor. These values will increase for nanowires with grain boundaries present, such as the nanowires fabricated in this work, and so it is important that these nanowires be characterized. Grown between two microelectrodes, measuring I/V curves will determine nanowire resistance. Using the resistivities noted above and a simple model of a cylindrical copper nanowire 1  $\mu\text{m}$  long and 30 nm in diameter gives a resistance of 50  $\Omega$ . To avoid junction effects, the nanowires could be grown between two copper microelectrodes, or to study junction effects, different metals could be used as these electrodes.

### **5.3 Adsorbates on Graphite Conclusion**

#### **5.3.1 Conclusion**

The research described in Chapter 4 investigates the nanoscale electrical interaction of azulene compounds and gold nanoparticles adsorbed on a graphite surface through surface potential mapping. Azulene compounds with electron donating groups on odd numbered carbons exhibited a positive potential contrast with the graphite surface, and compounds with electron withdrawing groups on odd numbered carbons resulted in a negative potential contrast with the graphite surface. The gold nanoparticles, however, all showed a positive potential

contrast, regardless of shape. This confirms the idea that azulene compounds have the potential to be used as tunable dopants for graphene-like materials. Better control of the amount and type of doping will enable better and more efficient graphene devices.

Studies have been previously reported describing adsorbates on graphene, but mostly investigated on a macroscopic scale. One study, however also describes surface potential mapping to investigate the interaction of two compounds on graphene.<sup>7</sup> One is heavily fluorinated with electron withdrawing character and the other has a vanadium center with electron donating character. These compounds were adsorbed onto exfoliated graphene and graphene used in FETs. They found that the compound with electron withdrawing groups p-doped the graphene, while the compound with the metal center n-doped it, with results similar to those in Chapter 4. Gold nanoparticles on graphene has been described before, although there is some debate in the literature as to whether the particles p-dope or n-dope the graphene.<sup>8,9</sup> Both studies describe loading graphene sheets in FETs with gold nanoparticles and using the FET characteristics to determine the type of doping. One found only p-doping character<sup>8</sup>, while the other found n-doping character at lower surface coverages, but p-doping at high coverages when the gold nanoparticles begin to interconnect.<sup>9</sup> The data in Chapter 4 corroborates the n-doping results.

This research has implications in the design and construction of devices incorporating graphene and graphene-like materials. Precise control over the electronic properties of these materials is crucial to their intended function. By having a variety of azulene dopants that can tailor the electronic properties of graphene, devices utilizing graphene can be better designed and thus more functional and efficient. One example is the use of graphene as the transparent electrode in solar cells. Not only does the graphene need to be a conductor in this instance, its

Fermi level must be matched with the other materials in the cell in order to maximize efficiency. The ability to tune this level will enable the fabrication of more efficient graphene solar cells. Another example is graphene or CNTs used as the channel material in FETs. In this case, the graphene or CNT must act as a semiconductor, and so a band gap must be induced into the graphene material. Again, the ability for precise tuning of this property in graphene-like materials will lead to better functioning graphene or CNT based FETs. These are but two examples of many instances where researchers are experimenting with graphene-like materials, and a better control over electronic properties of these materials will lead to advances in devices utilizing them.

### 5.3.2 Future Direction

This research showed that azulene compounds with different substituents can behave differently on graphite, but only four azulene compounds were studied. In order to better establish the trend in substituent type and doping type, more azulene compounds must be studied. The next step for this work is to study more azulene compounds to better establish this trend. This will include molecules with substituents that have a range of electron donating and withdrawing strength, both on odd numbered and even numbered carbons. This will fully explore the range of possible interactions between azulenes and graphite. The future direction of the project is adsorbing azulenes onto graphene and CNTs for surface potential mapping and doping characteristics to fully explore the role azulene compounds can play in tuning the electronic properties of these materials.

#### 5.3.2.1 Azulene Compounds

In order to better establish the trend seen in Chapter 4 of the azulene compounds with electron drawing groups p-doping the graphite and azulenes with electron donating groups n-doping it, a wider range of azulenes must be studied. Initial experiments will start with varying the substituents on the odd carbons to include a broader range of electron withdrawing and donating strength than was shown in Chapter 4. It would also be interesting, however, to modify the LUMO by placing a similar range of substituents on the even numbered carbons. This will help establish a solid understanding of the relationship between the position of these orbitals and what is seen in the surface potential images. If the position of the LUMO is near the Fermi level of the graphite, as posited in Chapter 4, destabilizing it enough with electron donating groups on even carbons would favor interaction between the Fermi level and the HOMO, with results similar to the DIA in Chapter 4. Stabilizing the LUMO, by electron withdrawing groups on even carbons, would lower the LUMO energy but it would still be closer to the Fermi level than the HOMO, with results similar to the DTFA.

#### 5.3.2.2 Adsorbates on Graphene and CNT

Graphite served as a model surface for other graphene-like materials in Chapter 4. In a device, the material that will be modified is graphene or CNTs. Future work will be adsorbing these same azulene compounds onto graphene and CNTs and measuring their electronic properties with surface potential imaging. Graphene and CNTs are two and one dimensional materials, respectively, and so adsorbate interactions can have a measureable effect on their properties. Surface coverage and adsorbate morphology could have an impact on these interactions, which will be elucidated by examining the interactions on the nanoscale.

### **5.4 Final Statement**

The research presented in this dissertation has advanced AFM based methods for fabrication and characterization of nanoscale and nanostructured devices. Directed and controlled fabrication of copper nanofeatures with oxidative lithography and electroless copper plating has been demonstrated, and a novel system, azulene compounds adsorbed onto graphite, has been explored at the nanoscale with surface potential imaging. As mentioned previously, these systems have implications in fabrication and characterization of novel electronic nanodevices as well as nanostructured devices such as solar cells and this research brings us closer to realizing such devices. Through the future directions outlined above, this research will continue to shed light on the nanofabrication and electronic properties of metal nanofeatures and graphene-like materials and the eventual fabrication of nanodevices utilizing them.



## References

1. Berson, J.; Zeira, A.; Maoz, R.; Sagiv, J., *Beilstein J. Nanotechnol.* **2012**, *3*, 134-143.
2. Kwon, G.; et al., *Nanotechnology* **2012**, *23* (18).
3. Chang, Y. H.; Wang, C. H., *J. Mater. Chem.* **2012**, *22* (8), 3377-3382.
4. Lu, P.; Walker, A. V., *Langmuir* **2007**, *23* (25), 12577-12582.
5. Bid, A.; Bora, A.; Raychaudhuri, A. K., *Physical Review B* **2006**, *74* (3).
6. *CRC Handbook of Chemistry and Physics* [Online]; <http://hbcnetbase.com> (accessed Dec 6, 2012).
7. Wang, X. M.; Xu, J. B.; Xie, W. G.; Du, J., *J. Phys. Chem. C* **2011**, *115* (15), 7596-7602.
8. Ren, Y. J.; et al., *Appl. Phys. Lett.* **2010**, *97* (5).
9. Wu, Y. P.; et al., *Small* **2012**, *8* (20), 3129-3136.